Effects of melting, subduction-related metasomatism, and sub-solidus equilibration on the distribution of water contents in the mantle beneath the Rio Grande Rift (USA)

Lillian A. Schaffer[1], Anne H. Peslier[2*], Alan D. Brandon[1], Michael Bizimis[3], Robert Gibler[1], Marc Norman[4], Jason Harvey[5]

[1]University of Houston, Houston TX 77004, USA

[2]Jacobs, NASA Johnson Space Center, Mail Code XI3, Houston, TX 77058, USA; anne.h.peslier@nasa.gov

[3]University of South Carolina, Columbia SC, 29208, USA

[4]Research School of Earth Sciences, The Australian National University, Canberra ACT 2600, Australia

[5]School of Earth and Environment, University of Leeds, Leeds LS2 9JT, UK

*Corresponding author

Abstract

The distribution of water in the upper mantle plays a crucial role in the Earth's deep water cycle, magmatism, and plate tectonics. To better constrain how these large-scale geochemical systems operate, peridotite and pyroxenite mantle xenoliths from Kilbourne Hole (KH) and Rio Puerco (RP) along the Rio Grande Rift (NM, USA) were analyzed for water contents, and major and trace element compositions. These xenoliths sample a lithosphere whose composition was influenced by subduction and rifting, and can be used to examine the effects of melting, metasomatism, and sub-solidus equilibration on the behavior of water.

The KH peridotites have 252-447 ppm H_2O in clinopyroxene (Cpx) and 73-174 ppm H_2O in orthopyroxene (Opx) and can be divided into two groups. Group 1, representing the majority of KH xenoliths, has flat to depleted light rare earth element (LREE) patterns in Cpx and bulk-rock when normalized to primitive mantle (PM). The trace element and water contents of Group 1 KH

peridotites can be modelled by melting processes as long as a correction for sub-solidus equilibration is first applied to be able to model the water content of individual phases. Exceptionally for an off-cratonic setting, olivines in KH xenoliths underwent negligible H loss during xenolith ascent and preserved their mantle water contents (5-25 ppm H_2O). Based on lower olivine water contents and higher calculated viscosities relative to those of the asthenosphere, KH Group 1 peridotites represent samples from the lithosphere. The KH peridotites thus provide the first estimate of the concentration of water (98±13 ppm H_2O) in the off-cratonic continental mantle lithosphere. Sub-solidus equilibration also provides an explanation for the discrepancy between the Cpx/Opx ratio of water contents in natural peridotites worldwide and in laboratory experiments on water partitioning in peridotite minerals. Group 2 KH peridotites have enriched LREE PM-normalized patterns consistent with cryptic metasomatism, while KH clinopyroxenites (227-275 ppm H_2O) represent crystallized mantle melts.

In contrast, the olivines from the RP xenoliths appear to have experienced almost complete H loss during xenolith ascent. Pyroxenes and bulk-rock compositions of RP peridotites have a wider range of depleted to enriched LREE PM-normalized patterns and of water contents, compared to those at KH. The water and other trace element contents of two of the RP peridotite xenoliths (0 and 266 ppm H_2O in Cpx and 0 and 100 ppm H_2O in Opx) can be modelled by melting processes. The other RP peridotites contain 225-412 ppm and 68-138 ppm H_2O in Cpx and Opx, respectively, and have trace element compositions consistent with metasomatism. Trace element modelling of the metasomatized KH and RP peridotites suggests that the metasomatic melts are of subduction origin. These melts contain about two times more water at RP than at KH, although this did not result in a more water-rich mantle lithosphere at RP. Rio Puerco lies within northern Rio Grande

rift, proposed to have been affected by a flat slab subduction, which may explain the more hydrous and extensive metasomatism compared to the south, where KH is located.

1. Introduction

Mantle peridotite incorporates hydrogen atoms, typically quantified as weight parts per million (ppm) H_2O in the literature, into crystal defects of its nominally anhydrous minerals: olivine, pyroxene, and garnet (Bell and Rossman, 1992; Libowitzky and Beran, 2006). These trace amounts of water have the potential to dramatically decrease the mechanical strength of the mantle lithosphere via the hydrolytic weakening of olivine and the peridotite melting temperature (e.g., Chopra and Paterson, 1984; Drury, 1991; Gaetani and Grove, 1998; Green, 1973; Mackwell et al., 1985; Mei and Kohlstedt, 2000a, b; Faul et al., 2016). Water contents can also affect geophysical properties such as electrical conductivity, thermal conductivity and seismic attenuation of peridotite (e.g., Hirth et al., 2000; Hofmeister, 2004; Karato, 1990, 2006; Karato and Jung, 1998; Wang et al., 2008), although the latter remains equivocal (Cline II et al., 2018). Consequently, the water content of the upper mantle has been estimated from indirect methods such as seismology, electrical conductivity or numerical modeling (e.g., English et al., 2003; Gao et al., 2004; Jones, 2016; van der Lee et al., 2008; West et al., 2004), but the utility of these methods can be limited by non-unique solutions and large uncertainties. For example, results can be compatible with either the presence of water or that of small amounts of melt (e.g., Gao et al., 2004; West et al., 2004). In contrast, mantle xenoliths provide the opportunity to evaluate directly the influence, behavior, and concentrations of water in the mantle, once the potential effects on water of xenolith transport to the surface by the host magma have been addressed.

Mantle xenoliths from two localities in New Mexico, Kilbourne Hole (KH) in the southern Rio Grande Rift (RGR), and Rio Puerco (RP) in the northern RGR are examined here. These xenoliths sample the mantle in a continental region that is characterized by the interplay of flat subduction and rifting, processes where water is a key factor (e.g., English et al., 2003; Green, 1973; Harvey et al., 2011; Harvey et al., 2015; Humphreys et al., 2003; Peacock, 1990; Schmidt and Poli, 1998). Previous work on KH mantle xenoliths has shown that many of their compositional characteristics are related to partial melting (Carter, 1070; Irving, 1980; Bussod and Irving, 1981; Bussod and Williams, 1991, Perkins and Anthony, 2011; Harvey et al., 2012, 2015). Given that peridotite xenoliths with no obvious metasomatism are rare (Menzies, 1983), this will provide the opportunity to constrain the behavior of water during melting. In particular, the distribution of water between natural mantle phases is at odds with that observed in experiments on water partitioning during melting of peridotite, and modelling with experimentally derived mineral-melt partition coefficients for water fails to properly explain water content variations in minerals from peridotite xenoliths and abyssal peridotites (e.g., Aubaud et al., 2004; Demouchy and Bolfan-Casanova, 2016; Hao et al., 2014; Hauri et al., 2006; Peslier et al., 2017; Tenner et al., 2009; Warren and Hauri, 2014).

In addition, some samples from KH and RP have been metasomatized by fluids and/or melts (Harvey et al., 2012; Porreca et al., 2006). The goal of this study is to constrain the behavior of water during melting, sub-solidus equilibration, and metasomatism in a tectonic setting where flat-slab subduction was followed by rifting as the slab rolled back (Chapin, 1979; Dickinson and Snyder, 1978; English et al., 2003; Saleeby, 2003). In particular, two questions are addressed using the combination of the water contents and additional compositional characteristics in the mantle xenoliths from KH and RP. The first question is whether the unmetasomatized KH mantle

xenoliths represent asthenosphere that upwelled as a result of lithospheric thinning during rifting, as has been proposed for some mantle xenoliths within the Rio Grande Rift (Byerly and Lassiter, 2012), or whether they are lithosphere that was already present during rifting. Second, the influence of flat subduction on metasomatism and hydration of the mantle is examined by comparing metasomatized KH and RP xenoliths. Both of these issues are related to changing continental and mantle dynamics, and how these affect the water contents in an off-cratonic lithospheric mantle.

2. Rio Grande rift tectonic, geodynamics, and the possible role of water

The Rio Grande Rift lies at the eastern edge of the Basin and Range province located in the southwestern United States (Fig. 1). The rift formed during the large-scale magmatism and broad extension that occurred during the Farallon slab roll-back starting between 55 – 40 Ma (e.g., Coney and Reynolds, 1977; Copeland et al., 2017; DeCelles, 2004; Eaton, 1982; Humphreys, 1995). Subduction of the Farallon slab began along the western border of the United States more than 150 Ma ago (e.g., DeCelles, 2004). However, around 80 Ma it appears that the angle of subduction shallowed to the extent that portions of the Farallon slab were in direct contact with the North American lithosphere (Dickinson and Snyder, 1978). This is referred to as flat-slab subduction, and the region of the western United States that experienced flat-slab subduction is referred to as the "flat-slab corridor" (Fig. 1; English et al., 2003; Saleeby, 2003). Sometime between 40-55 Ma, the Farallon slab began to founder and roll back towards the west which caused widespread extension throughout the western United States known as the Basin and Range province (e.g., Coney and Reynolds, 1977; Copeland et al., 2017; Humphreys, 1995).

Water may have played an important role in tectonic and geodynamic processes of the Rio Grande Rift. Hydration of the mantle lithosphere beneath the southwestern USA by the Farallon

subduction has been inferred west of the Rio Grande Rift, including beneath the Colorado Plateau (e.g., Dixon et al., 2004; Li et al., 2008; Smith, 2000). In particular along the flat-slab corridor, any fluids or melts that might have been generated from the slab would go directly into the lithosphere. This would potentially hydrate this zone more than the adjacent areas that experienced steeper-angled subduction where slab fluids would have to travel through the asthenosphere first (Humphreys et al., 2003). Both suites of xenoliths examined here are from host-magma erupted after the Farallon roll-back. Measuring the water contents directly in mantle xenoliths from the Rio Puerco Volcanic Field (RP), which erupted within the flat-slab corridor, and from Kilbourne Hole (KH) volcanics, which did not, should provide a test of the hypothesis that flat-slab subduction added more water to the overlying lithosphere than subduction that occurred with a steeper slab angle (Humphreys et al., 2003).

It has also been observed that anomalously slow P and S wave velocities are recorded beneath the northern tip of the Rio Grande Rift (red line in Fig. 1) at depths as shallow as 45 km (Gao et al., 2004; Sosa et al., 2014; van Wijk et al., 2008; West et al., 2004). This anomaly could be explained either by (i) higher mantle water contents in the anomalous zone compared to the adjacent mantle, (ii) the presence of partial melts, or (iii) removal and replacement of the lithosphere by hotter asthenosphere (Gao et al., 2004; West et al., 2004). It has been suggested that KH peridotite xenoliths are sampling asthenosphere or new lithosphere compositionally similar to the asthenosphere below (Byerly and Lassiter, 2012; Gao et al., 2004; Kil and Wendlandt, 2004; Perry et al., 1988; Rowe et al., 2015; Thompson et al., 2005). However, it is Rio Puerco that is also located in the northern section of the rift where the slow seismic velocity anomaly has been detected (Gao et al., 2004; West et al., 2004). This anomaly has thus been speculated to extend to the southern Rio Grande Rift mantle (Byerly and Lassiter, 2012), where KH is located. Moreover,

Rio Puerco xenoliths have trace element and isotopic compositions that indicate extensive metasomatism typical of the subcontinental lithosphere, and compositional characteristics of the lavas from this area also rule out an asthenospheric origin (Byerly and Lassiter, 2012; Perry et al., 1988). On the other hand, lithosphere thicknesses are similar at RP and KH: ~50 – 75 km thick at Rio Puerco and ~40 – 80 km at Kilbourne Hole (Achauer and Masson, 2002; Cordell et al., 1991; Thompson et al., 2005). Equilibration pressure estimates are also similar: 1 – 1.8 GPa (based on phase stability diagrams) at RP and 1.1 – 1.8 GPa at KH (based on garnet pyroxenites), corresponding to depths of 35 – 55 km (Perkins and Anthony, 2011; Porreca et al., 2006). These depths coincide with that of the anomalous slow seismic velocity anomaly that ranges from 45 to several hundred km (Gao et al., 2004; Sosa et al., 2014; West et al., 2004). Comparing water contents and calculating viscosities using olivine water contents (Li et al., 2008), in combination with major and trace element compositions, in RP and KH xenoliths could provide constraints on whether the KH peridotites are from the lithosphere or from the asthenosphere.

In summary, measuring the water contents of well-characterized peridotite xenoliths from the Rio Grande Rift will allow to test two hypotheses:

1. Flat-slab subduction hydrates the lithosphere more than steeper subduction
2. Lithosphere has been removed and replaced with asthenosphere or by new lithosphere of asthenospheric composition during slab roll-back and rifting.

3. Samples

Mantle xenoliths from two localities along the Rio Grande Rift are examined here: KH and RP (Fig. 1). The water contents of 29 mantle xenoliths were measured along with major and trace element contents in their bulk-rock and minerals.

Kilbourne Hole is a volcanic maar located in the Potrillo Volcanic Field (New Mexico, USA), which is close to the axis of the southern Rio Grande Rift. High-silica ash-flow sheets and basaltic to andesite lavas in this segment of the rift are the oldest known volcanic rocks along the entire rift, with a ^{87}Rb-^{87}Sr age of 32 Ma (Stinnett and Stueber, 1976). Xenoliths are found in a basanite that has been dated from 80 – 141 ka (Bussod and Williams, 1991; Dromgoole and Pasteris, 1987; Hoffer, 1976). The majority of the mantle xenoliths have sustained low degrees of deformation (protogranular texture), although pyroxenites and some peridotites have experienced more deformation (porphyroclastic; Kil and Wendlandt, 2004). Previous studies conclude that the geochemistry of most KH peridotites is primarily controlled by partial melting rather than metasomatism based on major element melting models (Herzberg, 2004), Sm-Nd isotope systematics, and depleted concentrations of light rare earth elements (LREE; La – Nd) compared to heavy rare earth elements (HREE; Dy – Lu) (Harvey et al., 2012; Roden et al., 1988). A minority of xenoliths display evidence of metasomatism, either texturally or geochemically, which may be caused by subduction-related fluids from the Farallon slab (Harvey et al., 2012; Perkins et al., 2006; Roden et al., 1988). Twenty-one xenoliths (18 peridotites and 3 pyroxenites) were analyzed for water content, including four peridotites that have been previously described in Harvey et al. (2012).

The Rio Puerco Volcanic Field (New Mexico, USA) is a group of volcanic necks found in the northern portion of the Rio Grande Rift located on the boundary between the rift and the Colorado Plateau, and is intersected by the Jemez Lineament. The Jemez Lineament is a zone of Cenozoic volcanism thought to occur at a suture zone between Archean provinces (Karlstrom et al., 2002; Karlstrom et al., 2005; Magnani et al., 2005; Magnani et al., 2004). Peridotite and pyroxenite xenoliths are found in alkaline basalts dated at 2.05-4.49 Ma (Hallet, 1994; Hallet et

al., 1997). At least one infiltrating melt that affected the mantle represented by these xenoliths had a carbonatite component indicated by calcite found in xenoliths (Perkins et al., 2006). Moreover, analyses of oxygen isotope ratios in RP pyroxenites and peridotites suggest that discrete metasomatic events associated with the Farallon slab have affected the mantle beneath this locality (Perkins et al., 2006; Porreca et al., 2006). Nine RP spinel mantle xenoliths were analyzed for water and were collected at four different volcanic necks: CSR (Cerro de Santa Rosa), CSC (Cerro de Santa Clara), CN (Cerro Negro), and CTON (Cerrito Negro).

4. Methods

Water, major and trace element concentrations were measured for each mineral phase within the 26 xenoliths. Thin sections were made and used for texture identification and, for a sample with two lithologies (KIL41), point-counting to obtain mineral mode. Polished grain mounts on two parallel sides were made for Fourier Transform Infrared Spectroscopy (FTIR) analysis of each sample. Except for the 4 samples from Harvey et al. (2012) for which data were already available, the same grain mounts were used for mineral major and trace element in situ analysis via electron microprobe (EMP) and Laser Ablation-Inductively Coupled Plasma-Mass Spectrometry (LA-ICP-MS), respectively. Bulk-rock major and trace element data was also acquired for most samples by ICP-MS or X-ray fluorescence spectroscopy (XRF).

.4.1. Sample Preparation

Edges of the xenoliths (sized 10-25 cm for KH and 5-15 cm for RP) were avoided due to potential basalt contamination within a few mm of the xenolith margin and fractions from the center were gently crushed. Between 20 – 30 grains of each mineral were selected for FTIR analyses, embedded in epoxy and polished on two parallel sides. In each grain mount, a petrographic microscope was used to determine the orientation of each mineral grain using

interference figures. Grains oriented along a Bxo, Bxa, or optic normal crystallographic axes were photographed and the axes marked on the photos. Each oriented grain had its thickness measured using a Mitutoyo Absolute digimatic micrometer with a 2 σ precision of ± 3 μm. The grain mounts ranged in thickness from 100 to 600 μm.

4.2. Fourier Transform Infrared Spectroscopy (FTIR)

Analyses to obtain water contents were performed at the NASA-Johnson Space Center using the Hyperion 3000 microscope of a Bruker Vertex 70 FTIR. Aperture size ranged between 50 x 50 μm and 100 x 100 μm and was modified based on the shape and quantity of fractures or inclusions to be avoided. The FTIR spectrometer, including the sample stage area, was flushed continuously with dry nitrogen gas to avoid contamination by atmospheric water. Samples were stored in a cabinet flushed with N_2 gas and heated for at least an hour in a furnace at 80 °C to remove surface water prior to FTIR analyses. Measurements of each grain were conducted using polarized infrared light oriented parallel to one of the optical indices α, β, or γ.

Transmission spectra were measured from wavenumbers 4000 – 680 cm^{-1} and with a spectral resolution of 4 cm^{-1}, over 128 scans for pyroxenes and 200 scans for olivine, the latter because of low water contents (< 10 ppm H_2O). At least three locations on each grain were analyzed if possible, including at least one at the edge of the grain in order to assess intra-grain water content heterogeneities. Line scans were run on olivine grains to quantify the extent of H loss throughout the grain during host magma ascent (Peslier and Luhr, 2006). Each spectrum was normalized to a thickness of 1 cm, and the area under the absorption bands caused by O-H bond vibrations was measured (between 3750 – 3000 cm^{-1} for clinopyroxene, 3750 – 2800 cm^{-1} for orthopyroxene, and 3700 – 3100 cm^{-1} for olivine). Each spectrum baseline was drawn by hand, a method that provides as precise and consistent results as subtracting the spectrum of a dehydrated

mineral or applying a mathematical function to model the baseline (Bell et al., 1995, 2003). In particular, using dehydrated mineral spectra would require dehydrating minerals for each xenolith because the baseline shape is composition specific, rendering the method unpractical. The hand-drawn method may result in systematic errors in precision of up to 20% (Peslier et al., 2012). The integrated absorbances obtained in this way from the spectra can be put into a modified version of the Beer-Lambert law to calculate water contents:

$$C_{H2O} = A_i / I_i \quad \text{(eq. 1)}$$

where C_{H2O} is the water content in ppm H_2O, I_i is the mineral-specific integrated molar absorption coefficient, and A_i is the sum of the areas beneath the OH vibration along the three optical indicatrix indices α, β, and γ (Libowitzky and Beran, 2006). Integrated molar absorption coefficients used in this study are from Bell et al. (1995) for pyroxene and Bell et al. (2003) for forsteritic olivine. The detection limit is estimated at < 0.5 ppm H_2O. The uncertainties in this calculation and their origins are discussed in previous studies (Peslier and Luhr, 2006; Peslier et al., 2002) and were included in an error propagation formula to calculate ± 1σ error for water contents shown in the figures and Table 1.

4.3. Electron Microprobe

The analyses of major elements were performed on pyroxene, olivine, and spinel using a Cameca SX100 electron microprobe at NASA-Johnson Space Center. Running conditions were 15 kV and 20 nA, 20 s on peak and 10 s on background. The standards used were oligoclase for Na; diopside, forsterite, or chromite for Mg; diopside for Ca; orthoclase for K; rutile for Ti; chromite for Cr; fayalite or chromite for Fe; rhodonite for Mn; nickel oxide for Ni; diopside or forsterite for Si; and oligoclase or chromite for Al. For each xenolith, a minimum of 3 grains of

each phase and a minimum of 3 locations on each grain were analyzed. For analyses, standard deviation is better than 1% for all elements except for Mn (6%). Detection limits are better than 0.02 wt.%, with the exception of Mn and Fe (0.04 wt.%). The EMP data in Table SI2 are averages of analyses on multiple grains within one thick section.

4.4. Inductively Coupled Plasma Mass Spectrometry (ICP-MS)

Trace element concentrations were measured in selected clinopyroxene and orthopyroxene grains by laser ablation (LA) ICP-MS at the University of Houston using a Varian 810-MS quadrupole ICP-MS connected to a CETAC LSX-213 laser operated at 10 Hz and an intensity of approximately 3 mJ per pulse. For each 100 µm spot analyzed, a gas blank was collected for 15-20 seconds followed by 30 seconds of sample ablation. The standard reference materials, the NIST glass KL2-G (Kempenaers et al., 2003) or the USGS glass BHVO-2G (Gao et al., 2002) were used to correct for instrumental drift and fractionation and relative element sensitivities, while the USGS reference basaltic glass BIR-1G was used to monitor external reproducibility. Data were reduced with the data reduction software package Glitter, with each analysis normalized to the Mg concentration measured by electron microprobe to correct for variations in ablation yield.

Bulk-rock trace element compositions of xenoliths were analyzed at Washington State University or at the Australian National University (samples KIL-1, 2, 3, 8, 41, 43, 44, 70, and 71) using powders from rock chips prepared from the center of each xenolith. Samples were crushed in an alumina mortar. The resulting powders were fused in Li tetraborate, digested, and measured as a solution on an Agilent 4500 ICP-MS (Washington State University; Johnson et al., 1999) or dissolved in HF + HNO_3 and measured as a solution on an Agilent 7500 (Australian National University; Norman et al., 1998). Precision for the methods employed at Washington State University and the Australian National University is typically better than ±5% (RSD).

4.5. X-Ray Fluorescence (XRF) Spectrometry

The powders prepared for bulk-rock ICPMS were also used for XRF analysis at Washington State University to obtain major and selected trace (Ni, Sc, V, Sr, Zn, Zr, Ga, and Cu) element concentrations (Johnson et al., 1999). The powders were fused with Li tetraborate. Nine USGS reference rocks (PCC-1, BCR-1, BIR-1, DNC-1, W-2, AGV-1, GSP-1, G-2, and STM -1) were used to construct calibration curves of element sensitivities relative to known concentrations. Two fusion beads of pure vein quartz were used as blanks for all elements except silicon. The USGS reference materials BCR-1 and GSP-1 were used as internal standards. The 2 σ standard deviations for the major element analyses are ±0.6 wt.% for SiO_2, and less than or equal to ±0.2 wt.% for all other major elements. The 2 σ standard deviations for the trace element analyses are less than ±5 ppm for all elements with the exception of Cu (±7.4 ppm). For bulk-rock Ni, Sc, V, Sr, Zn, Zr, Ga, and Cu, ICP-MS data are used preferentially over XRF data for better consistency with other elements given that a larger number of elements was measured using ICPMS (Table SI3).

5. Results

5.1. Petrology

5.1.1 Kilbourne Hole xenoliths

Thirteen spinel peridotites and three pyroxenites were collected for this study. Four additional KH peridotites (KH03-15, KH96-08, KH96-20, and KH96-21) were previously characterized previously by Harvey et al. (2012) (Table 1). All but one peridotite in this study are coarse-grained peridotites (average grain size 2-4 mm, protogranular texture (e.g., Mercier and Nicolas, 1975; Fig. SI1b). Sample KIL8 is finer-grained (<2 mm average grain size) and is weakly foliated with an equigranular texture (Fig. SI1a). All of the samples are composed of olivine,

298 orthopyroxene, clinopyroxene, and spinel. Mineral modes (weight %) were calculated using a
299 least-squares inversion method using bulk-rock major elements in combination with mineral major
300 elements (e.g., Armytage et al., 2014; Harvey et al., 2012; Tarantola and Valette, 1982). Of the 17
301 KH peridotites in this study, thirteen are lherzolites, three are harzburgites, and one is a dunite
302 (Table 1). KIL41 contains a ~3 mm wide clinopyroxenite vein (Fig. 2a). Even after subtracting the
303 contribution from the clinopyroxenite vein, the least-squares inversion method cannot resolve
304 whether the peridotitic part of KIL41 should be classified as lherzolite or harzburgite. For this
305 reason, its modal mineralogy was recalculated by point counting three thin sections using 500 µm
306 increments (four times smaller than the average grain size) to determine that its main lithology is
307 a harzburgite (Table 1). The samples KIL44 and KIL70 contain minerals with overgrowth rims
308 containing numerous secondary spinel grains. These rims are not exclusive to one phase and
309 surround all types of silicate minerals. Some KH peridotites contain clinopyroxenes with a
310 "spongy" edge (Harvey et al., 2012) but such a feature has not been observed in KH samples from
311 this study. Veins of interstitial glass with an average thickness of approximately 30 µm are present
312 in four peridotites (KIL1, KIL2, KIL3 and KIL41). No resorption along mineral rims in contact
313 with the glass is present. Similar veins are present within KH xenoliths studied by (Harvey et al.,
314 2012). These veins were interpreted to be trapped residual melts of << 1% degrees of partial
315 melting in the mantle.

316 Mineral modes for KH pyroxenites were estimated using the least-squares inversion
317 method. Samples KIL16, KIL82, and KIL83, are classified as olivine clinopyroxenites and are
318 predominantly composed of clinopyroxene with minor spinel. Amphibole is present in KIL83, but
319 was not included in the least-squares inversion because no amphibole was analyzed for major
320 element concentrations. KIL83 is composed primarily of interlocking subhedral to anhedral

clinopyroxene with minor olivine and spinel, with amphibole always adjacent to spinels. Orthopyroxene is present in KIL82 (approximately 2 %; Table 2). All KH pyroxenites are fine-grained with clinopyroxene grains in all three samples ranging from 0.1 – 1 mm, spinel grains ranging from 50 μm – 1.25 mm, and olivine grains consistently measuring approximately 0.1 mm in size. Pyroxenite KIL82 is composed primarily of anhedral clinopyroxene grains (~0.5 mm) that are surrounded by a finer grained clinopyroxene (20-50 μm) matrix. With a similar texture to KIL83, pyroxenite KIL16 is composed primarily of interlocking clinopyroxene with reaction rims. However, in one region of the KIL16 thin section, rounded anhedral clinopyroxenes are surrounded by 0.1 mm anhedral grains of olivine, spinel and glass.

5.1.2 Rio Puerco xenoliths

Mineral modes for the RP spinel peridotites were calculated using the same least squares inversion method previously described for KH peridotites. Results of the least squared inversion method show that of the nine RP samples there are seven lherzolites, one harzburgite, and one olivine websterite (Table 1). In general, samples from Rio Puerco are heterogeneous in grain size and show signs of deformation (e.g., undulose extinction in olivine and orthopyroxene; Porreca et al., 2006). Websterite CTON-53 additionally contains calcite that appears to be replacing olivine in response to melt-rock interactions (Porreca et al., 2006).

Thin sections were obtained for all RP xenoliths except CSC-61 and CTON-53 (no intact xenolith was available for these samples). All RP xenoliths show abundant fractures (Fig. SI1c, d), and are considered to have a porphyroclastic texture. All RP xenoliths with the exception of CSC-16, CN-105, and CSR-7 contain exsolution lamellae in either orthopyroxene or both orthopyroxene and clinopyroxene. Orthopyroxene in RP xenoliths can be the largest grains, with

maximum sizes of 4 – 6 mm. However, the majority of orthopyroxene grains in the RP peridotites are similar in size to olivine, clinopyroxene, and spinel, which are typically 0.25 – 1 mm in size. Small melt pockets or glass veins are present in thin sections of peridotites CSR-17, CSC-14, CN-4, and CSR-7. Glass veins present in peridotites CSR-7 and CN-4 are within 10 mm of the edge of the xenolith and interpreted to be contamination by infiltration of the host basalt. Basalt rinds surrounding xenoliths CSR-17 and CSC-14 are not included in the thin section, thus it is unclear if glass veins in these are host basalt contamination or if they are derived from mantle processes. Peridotite CSR-20 contains many olivine grains with red coloration around the edge of the grain and is interpreted to be related to transformation to iddingsite during surface weathering (Gay and LeMaître, 1961). Additional petrographic descriptions for the variety of textures and mineralogies of RP xenoliths (including CTON-53, which was not examined petrographically in this study) are presented in (Porreca et al., 2006). Back scatter electron images collected during EMP analyses show that samples CN-4, CTON-53, CSR-7, CSR-17, CSC-16, and CSC-14 contain crystallized melts, expressed as assemblages of glass, plagioclase, and accessory minerals such as spinel, sulfides, and ilmenite. Clinopyroxenes with a "spongy" border are present in RP xenoliths as well, both in this study (Fig. SI2) and previously (Porreca et al., 2006).

5.2. Major element chemistry and geothermometry

Bulk-rock and mineral major element analyses are reported in supplementary Tables SI1 and SI2. Kilbourne Hole peridotites have bulk-rock Al_2O_3 ranging from 0.34 to 4.0 wt.% (Fig. 3a) and Mg# (cation Mg/[Mg+Fe]) of 0.88-0.91. Rio Puerco peridotite xenoliths have bulk-rock Al_2O_3 ranging from 1.7 to 3.1 wt.% and Mg# of 0.89-0.91. These values are similar to non-cratonic peridotite xenoliths worldwide (e.g., Carlson et al., 2005; Frey and Prinz, 1978; Harvey et al., 2012; Irving, 1980; Pearson et al., 2003; Peslier et al., 2002; Roden et al., 1988). There is a wide

range of Mg# in KH pyroxenites, from 0.74 to 0.88 but their bulk-rock TiO_2, CaO, and Al_2O_3 contents do not exhibit wide ranges within KH pyroxenites (1.34 – 1.39 wt.%, 15.86 – 18.41 wt.%, and 12.23 – 13.26 wt.%, respectively).

In KH peridotites, the range of olivine Mg# is 0.88-0.91 (Fig. 3b and c), which is identical to the range of the peridotite bulk-rock Mg#. Peridotite orthopyroxenes are enstatites with Mg# of 0.89-0.91. There is no significant zoning present in minerals, and chemical composition is homogeneous between grains within the same sample. In KH peridotites, clinopyroxene is Cr-diopside with Cr_2O_3 between 0.6-1.6 wt.%, Mg# between 0.88-0.92, and Cr# (cation Cr/[Cr+Al]) between 0.07-0.22. Peridotite spinels have Cr# values ranging from 0.08-0.46. In KH pyroxenites, clinopyroxene is also of diopside composition (Mg# =0.89), except for KIL16 which instead contains augite (Mg# =0.77). Pyroxenite KIL 16 also has more Fe-rich olivine (Mg# =0.78, Fig. 3a and b insets) and lower Cr spinel (Cr# = 0.002) than the other two pyroxenites (olivine Mg# ~0.89, spinel Cr# >0.034).

The RP olivines have Mg# of 0.89-0.91 (Fig. 3b and c), which is the same as the RP bulk-rock Mg# range. Orthopyroxene is enstatite with Mg# values between 0.90-0.91. As described by Porreca et al. (2006) exsolution lamellae were sometimes present in pyroxene grains (Fig. SI1c). Clinopyroxene in RP xenoliths is Cr-diopside with Cr_2O_3 contents ranging from 0.5-1.2 wt.% and Mg# of 0.90-0.93. The "spongy" rims around some clinopyroxenes described earlier are slightly enriched in CaO, MgO, and Cr_2O_3, and slightly depleted in Na_2O, Al_2O_3, and FeO relative to the core of the grain (Fig. SI2). Spinel grains are homogeneous in composition within each xenolith and have Cr# of 0.1-0.36. Websterite CTON-53 has similar mineral compositions to the peridotites with Mg# for bulk-rock, olivine and orthopyroxene all ~0.91, a bulk-rock Al_2O_3 content of 2.52 wt. %, and a spinel Cr# of 0.31 (Fig. 3, Table SI1 and SI2).

389 Two-pyroxene geothermometers, (Brey and Köhler, 1990; Bertrand and Mercier, 1985),
390 were used to calculate the equilibration temperatures (Table 1). The temperatures were calculated
391 using a pressure of 1.5 GPa based on KH equilibrium phase diagrams created by Perkins and
392 Anthony (2011). Overall, the temperatures calculated with the Bertrand and Mercier (1985)
393 thermometer (928 – 1163°C) are approximately 50°C lower than those calculated with the Brey
394 and Köhler (1990) thermometer, in good agreement with other studies from this area (900 –
395 1050°C, Bussod and Irving, 1981; 889 –1163°C, Kil and Wendlandt, 2004; 939 – 1180°C, Harvey
396 et al., 2012; 944 – 1138°C; Perkins and Anthony, 2011). Pyroxenite KIL82, the only KH
397 pyroxenite containing orthopyroxene and clinopyroxene, was estimated to have an equilibration
398 temperature of 1025 ^{o}C (Table 1) using the Brey and Köhler (1990) geothermometer, i.e. within
399 the range of equilibration temperature of the KH peridotites. The range of temperatures calculated
400 for RP xenoliths at 1.5 GPa using the Bertrand and Mercier (1985) geothermometer (855 – 985°C)
401 is in good agreement with previous studies (900 – 1000°C, Porreca et al., 2006; 655 –1164 °C,
402 Perkins et al., 2006). There are no correlations between the calculated temperatures and peridotite
403 texture or lithology.

404 5.3. Trace element geochemistry

405 Bulk-rock and in situ clinopyroxene and orthopyroxene trace element compositions
406 (Supplementary information (SI) Tables SI 3-5) were obtained for all KH and RP xenoliths, with
407 the exception of RP peridotite CSC-16, which was not sufficiently large for bulk-rock ICP-MS
408 measurements. Figure 4 shows extended trace element concentration patterns of KH and RP bulk-
409 rock and pyroxenes normalized to primitive mantle (PM) concentrations from McDonough and
410 Sun (1995). Peridotites from KH show a range of concentrations in LREE compared to middle
411 REE (MREE; Sm – Tb) and HREE (Fig. 4a-c) in both clinopyroxene and bulk-rocks. Kilbourne

Hole peridotites are split here into two groups using the PM-normalized Ce/Yb ratio $(Ce/Yb)_N$ of their clinopyroxenes (Fig. 4a). Group 1 peridotites contain clinopyroxene with $(Ce/Yb)_N < 1$, while Group 2 peridotites have clinopyroxene $(Ce/Yb)_N > 1$. These correspond to Group 2 having LREE enrichment relative to HREE in clinopyroxene and bulk-rock, while Group 1 is characterized by flat to LREE-depleted patterns when normalized to PM. Although dunite KIL40 has a clinopyroxene $(Ce/Yb)_N$ ratio < 1, it exhibits higher MREE ≥ HREE in clinopyroxene and LREE≥ MREE in the bulk-rock relative to PM, and is thus assigned to Group 2.

There are systematic shifts to lower concentrations of the bulk-rock MREE to HREE from lherzolites, through harzburgites, to the dunite, consistent with the increasing abundance of olivine and decreasing abundance of clinopyroxene. Negative Ti (largest), Zr and Hf anomalies are observed in clinopyroxenes for all KH xenoliths, while the orthopyroxenes exhibit positive anomalies for these elements (Fig. 4a and b). Flat or positive Ti, Zr and Hf anomalies are observed in KH bulk-rock trace element patterns. This is caused by orthopyroxene preferentially incorporating these elements over clinopyroxene (Eggins et al., 1998). Harzburgites and dunites, having less clinopyroxene than lherzolites, still exhibit positive Ti, Zr and Hf anomalies while lherzolites do not. The bulk-rock REE profiles of KH Group 1 peridotites (Fig. 4c) are parallel to those of their clinopyroxenes. The trace element patterns of peridotites KIL82 and KIL8 appear relatively flat in both clinopyroxene and bulk-rock data. Group 2 KH peridotites show a concave-up trace element pattern, with Nb, LREE, and HREE concentrations that are higher relative to MREE concentrations. The KH pyroxenites have similar bulk-rock trace element PM-normalized patterns relative to each other (Fig. 4c), but their trace element concentrations are 10 – 100 times higher than those for the KH peridotites. Clinopyroxene was analyzed only in pyroxenite KIL82,

and has a trace element pattern that parallels those of the Group 2 peridotites but at ~ 5-10 times higher concentrations (Fig. 4a).

Rio Puerco xenoliths show a broader range in clinopyroxene trace element compositions (Fig. 4d), spanning from more LREE-depleted to more LREE-enriched than those from KH. Orthopyroxene trace element concentrations were largely below detection limits (Fig. 4e). No trace element pattern could be found to characterize a single RP volcanic neck, as each of the group of samples from each volcanic neck shows a range of patterns. With the exception of peridotites CSC-16 and CSR-20, La and Ce are enriched relative to Nd and Sm concentrations. In contrast, CSC-16 and CSR-20 trace element patterns show depletions in all LREE relative to HREE. Websterite CTON-53 and peridotites CN-105, CSR-7, and CSC-14 furthermore show positive Sr anomalies, which is mirrored in the clinopyroxene profiles except for CSC-14 clinopyroxene. There are negative Zr anomalies observed in clinopyroxene from CTON-53, CN-105, CSC-14, and CSC-16, and a negative Hf anomalies observed in clinopyroxene from CTON-53 and CN-4. Bulk-rock trace element compositions (Fig. 4f) for RP xenoliths have trace element patterns that are broadly parallel to those of their respective clinopyroxenes.

5.4 Water concentrations

Spectra obtained from FTIR O-H analyses for olivine and pyroxene (Fig. 5, details in SI2) are similar to what has been described before in peridotites (e.g., Beran and Libowitzky, 2006; Skogby, 2006). Water concentrations in pyroxenes of KH and RP xenoliths and in olivines from 7 of the KH xenoliths are homogeneous within mineral grain and within each xenolith (Table SI6). There is no difference in relative height or position of O-H bands between spectra in minerals from

455 lherzolite, harzburgite, dunite and pyroxenites. One peridotite from RP (CSR-20, the most LREE
456 depleted RP peridotite) had no detectable water in either clino-, orthopyroxene or olivine.

457 Clinopyroxenes in the peridotites have water contents that range between 250 and 447 ppm
458 H_2O for KH and 0 and 307 ppm H_2O for RP (Fig. 6a, d; Table 1, Table SI6). Rio Puerco peridotites
459 CSC-14 and CN-4 had no inclusion-free clinopyroxene appropriate for FTIR analyses, therefore
460 clinopyroxene water content estimates were made based on the $\frac{[H_2O]_{opx}}{[H_2O]_{cpx}}$ ratios of the other six RP
461 xenoliths (0.333 ± 0.07). The estimated water contents of CSC-14 and CN-4 clinopyroxene are
462 371 and 306 ppm H_2O, respectively. Since these contents are estimated rather than measured and
463 have higher uncertainties (calculated using error propagation formula), they are not included in the
464 range above.

465 Water contents in orthopyroxene are lower than those of clinopyroxene and range between
466 73 and 174 ppm H_2O for the KH peridotites and between 0 and 138 ppm H_2O for the RP peridotites
467 (Fig. 6e, d; Table 1). Water contents in olivine from KH range from 3 to16 ppm H_2O (Fig. 6c;
468 Table 1). The only RP peridotite with measurable water content in olivine is CSR-7 a maximum
469 of 17 ppm H_2O. In RP xenoliths, the water contents of peridotite minerals are independent of the
470 volcanic neck where the xenolith was collected.

471 Clinopyroxenes from KH pyroxenites have water contents (258-312 ppm H_2O) similar to
472 the KH peridotites, with the augite of KIL16 recording the lowest water content of all pyroxenites.
473 At RP, websterite CTON-53 is more water-rich than the peridotites and contains 581, 379 and 15
474 ppm H_2O in its clinopyroxene, orthopyroxene and at the core of its olivine, respectively.

475 At Kilbourne Hole, water contents are distributed homogeneously within pyroxene grains,
476 while the olivine water content is either homogeneous or heterogeneous within each single grain

(Table SI6 and Fig. 7). At Rio Puerco, all but two xenoliths contain olivine grains with water contents below the detection limit (~0.5 ppm H_2O). The two RP peridotites that contain olivine with detectable water have 50-75% less water at the edge compared to the core of the grain resulting in heterogeneous intra-grain water contents (Fig. 7).

5.5. Links between water content and other parameters

The range of peridotite lithologies from lherzolite, harzburgite to dunite in KH peridotites, results in correlations between clinopyroxene Al_2O_3 contents and modal abundances or bulk-rock Yb contents (Fig. 8a and b). Similarly, because the water contents of clinopyroxene in the harzburgite and dunite are lower than those of the lherzolites, water content in KH clinopyroxenes correlates with their modal abundance (Fig. 8d), clinopyroxene Al_2O_3 contents (Fig. 8c) and middle to heavy REE contents (Fig. 6b). At Kilbourne Hole, the water content of orthopyroxene correlates positively with clinopyroxene Al_2O_3 and ^{IV}Al content, orthopyroxene Al_2O_3 (Fig. 6e) and MgO contents, and olivine FeO content. However, there are no correlations between these any of these parameters within the lherzolites as a group (Fig. 6 and 8c and d). Based on this, KH peridotites exhibit general correlations between water content, melting indices, and lithology. No correlation, however, is seen between pyroxene water and REE contents, including Ce (Fig. 6f). No correlations exist between the water contents of KH olivine and other measured geochemical parameter (Fig. 6c).

At Rio Puerco, water content in peridotite clinopyroxene correlates with that of orthopyroxene (Fig. 6d), and with SiO_2 ($R^2 = 0.68$) and ^{IV}Al contents in clinopyroxene ($R^2 = 0.81$). Websterite CTON-53 water contents do not fall on any correlations exhibited by the peridotites, except the correlation between clinopyroxene and orthopyroxene water contents where it has the

highest water contents of any of the samples measured (Fig. 6d). Water contents in orthopyroxene from the Rio Puerco peridotites do not show any significant correlations with other parameters.

5.6. Bulk-Rock Water Calculations

Bulk-rock water contents for each xenolith were calculated by simple mass balance using modal mineralogy in combination with FTIR-derived water contents for each phase. They range from 10 to 118 ppm H_2O in KH peridotites and from 0 to 78 ppm H_2O in RP peridotites. All KH lherzolites have calculated bulk-rock water contents > 50 ppm. Lower water contents are found in the KH harzburgites (34-52 ppm H_2O) and the dunite (11 ppm H_2O). Among the RP xenolith suite, olivine websterite CTON-53 contains 268 ppm H_2O, which is 3.5 times the water content of peridotite CSR-7 (78 ppm H_2O). Bulk-rock water contents are strongly dependent on clinopyroxene water contents (R^2=0.85), thus correlations between bulk-rock water and other elements in peridotites are similar to correlations observed with clinopyroxene water contents (e.g., compare Fig. 6a and g).

6. Discussion

6.1. Mantle water content preservation

Hydrogen is one of the fastest diffusing elements in mantle minerals, and may be partially or completely lost, particularly from olivine, during xenolith ascent (Demouchy and Mackwell, 2006; Ingrin and Blanchard, 2006; Peslier and Luhr, 2006; Peslier et al., 2008, Brenna et al., 2018). Pyroxene grains in KH and RP peridotites have homogeneous water contents at the edges and cores of grains, which are therefore assumed to represent pre-xenolith entrainment (i.e., mantle) water contents. This is consistent with observations that in peridotites, lack of zonation in water content typifies natural pyroxenes worldwide (Bonadiman et al., 2009; Demouchy and Bolfan-

Casanova, 2016; Doucet et al., 2014; Hao et al., 2014; Li et al., 2008; Peslier and Bizimis, 2015; Peslier et al., 2002; Peslier et al., 2010; Skogby, 2006; Skogby et al., 1990; Sundvall and Stalder, 2011; Yu et al., 2011) while heterogeneous water contents in pyroxene have been observed only at two xenolith locations (Denis et al., 2018; Tian et al., 2017). Even the pyroxenes of KIL41, the harzburgite cross-cut by a clinopyroxene vein, have homogeneous water contents.

In contrast, the distribution of water contents in olivine grains from Kilbourne Hole is variable. Seven xenoliths contain olivine grains that have homogeneous water contents across the entire grain (e.g., Fig. 7a), while the other eight xenoliths contain olivines with lower H content at the rim of the grain relative to their respective cores (e.g., Fig. 7b, Table SI6). Water homogeneity or heterogeneity is independent of whether the olivines belong to peridotites from KH Group 1 or 2. Olivines with no core to rim variations in water content across the grain are interpreted to preserve mantle water contents. The olivines with less water at the rim of the olivine relative to the core are interpreted as having lost water during xenolith ascent. One-dimensional (1-D) modeling of diffusion profiles as described by Peslier et al. (2015) was applied to Kilbourne Hole olivine grains with heterogeneous water contents using the diffusion coefficients determined by Demouchy and Mackwell (2006) and by varying the total time that xenoliths underwent H loss. These mm-size KH grains exhibit water loss only within 200-400 μm of the edges, creating a plateau-shaped profile. The best fit to the data is modeled using the maximum absorbance values measured in the grain core as initial water contents (solid lines in Fig. 7b). Models with higher initial water contents do not produce diffusion profiles that match the data (dashed lines in Fig. 7b).

Based on these diffusion models, we conclude that the olivines in Kilbourne Hole peridotites preserved their original mantle water contents at the core of each grain. Preservation of

olivine water contents in off-craton xenoliths that are typically found in alkali basalts is exceptional, while it is routinely observed in xenoliths found in kimberlites from cratonic settings (e.g., Demouchy and Bolfan-Casanova, 2016; Doucet et al., 2014; Peslier et al., 2012). In the case of KH, the xenoliths are found in a maar which formed by rapid magma ascent and explosive eruption (e.g., Lorenz, 1975, 2003; Reeves and DeHon, 1965). The high rate of the magma ascent is supported by the observation that seven KH peridotites have grains with homogeneous water contents (Fig. 7a). These xenoliths are interpreted to have risen to the surface so quickly that no water loss took place. Importantly, these KH peridotites provide the first estimates of the water content of an off-cratonic subcontinental mantle lithosphere, with peridotites containing 10 to 118 ppm H_2O, and an average of 81 ± 30 ppm H_2O (Table 1).

Of the two RP xenoliths containing olivine with detectable water, CSR-7 and CTON-53, the water content profiles are bell-shaped, also interpreted as H diffusion profiles (Fig. 7c-d). Models using observed maximum absorbance values or higher absorbance values can be fit to the data by varying the modeled time it took for the H to diffuse. Because multiple model solutions can be fitted to olivine diffusion profiles using different initial absorbance values and different H diffusion times, it is unknown if measured water contents represent original mantle water contents (Peslier, 2010; Peslier and Luhr, 2006; Peslier et al., 2002; Thoraval and Demouchy, 2014). The reported water contents for RP olivine thus likely represent minimum values.

6.2. Water and mantle processes

6.2.1. Qualitative observations

Melting and metasomatism have both played a significant role in the geochemical evolution of the upper mantle beneath the Rio Grande Rift as can be deduced from the chemistry of KH and RP peridotites studied here. Within the 17 KH peridotites, the negative correlation

between olivine modal abundance and pyroxene water contents, positive correlation between bulk-rock Al_2O_3 wt.% and pyroxene water contents (Fig. 6), and negative correlation between olivine Mg# and orthopyroxene water contents are all qualitatively consistent with partial melting because water behaves as an incompatible element during melting (e.g., Aubaud et al., 2004; Frey and Prinz, 1978; Herzberg, 2004; Norman, 1998). The positive correlations between clinopyroxene H_2O and HREE concentrations of bulk rock and clinopyroxene (Fig. 6b) are also consistent with this interpretation (e.g., Frey and Prinz, 1978; Norman, 1998; Denis et al., 2015). In other words, since H is incompatible during melting (e.g., Aubaud et al., 2004; Michael, 1988)), the residues are progressively more depleted in water from lherzolites, through harzburgites to the dunite.

Within Group 1 KH lherzolites, for which clinopyroxene, orthopyroxene, and bulk-rock LREE contents are depleted relative to those of HREE (Fig. 4 a-c), there are correlations between bulk-rock Al_2O_3 content, olivine Mg#, and bulk-rock REE contents (Fig. 3a-c). Additionally, there are positive correlations observed between Group 1 Y and HREE concentrations in clinopyroxene (R^2 = 0.81-0.97, Yb shown in Fig. 9). These relationships are interpreted to be the result of partial melting (e.g., Herzberg, 2004; Norman, 1998). However, the water contents of Group 1 minerals do not correlate with any of the melting indices (Fig. 6), reflecting the limited range in variation of water content (336 to 447(± 25) ppm H_2O).

All Group 2 KH peridotites have clinopyroxene that have flat REE patterns or are enriched in LREE relative to HREE (Fig. 4a). This is interpreted to result from metasomatism by LREE-enriched melts. However, within KH Group 2, correlations between orthopyroxene Al_2O_3 and water contents (Fig. 6e), bulk-rock Al_2O_3 and water contents (Fig. 6g), and clinopyroxene water, Al_2O_3 and modal contents (Fig. 8a, b, d) span from lherzolite through harzburgite and dunite lithologies and are consistent with melt depletion. Although dunites can represent melt channels

590 in the mantle, KIL40, the dunite from KH, has a high olivine Mg# of 90.6, consistent with an origin
591 from high degrees of melting (Kelemen et al., 1995). The water contents of minerals in KH
592 peridotites that are affected by metasomatism do not correlate with other incompatible elements
593 such as LREE concentrations (Fig. 6f). These observations are consistent with either
594 metasomatism by water-poor melts and consequent preservation of water contents controlled by
595 earlier melting processes, or alternatively, from redistribution of water during sub-solidus re-
596 equilibration.

597 In contrast, the water contents of clinopyroxene in RP peridotites do not correlate with
598 melting indices (olivine Mg#, bulk-rock Al_2O_3 and HREE contents; Fig. 6). Additionally, all RP
599 peridotites except one contain concentrations of HREE approximately three times lower than a
600 primitive upper mantle composition (PM; McDonough and Sun, 1995; Fig. 4d-f), consistent with
601 these peridotites having undergone significant melting. The LREE in RP peridotites CSC-16 and
602 CSC-20 are depleted relative to MREE and HREE, a profile that can be generated via partial
603 melting. All other RP peridotites show some evidence of LREE enrichment, with the most extreme
604 examples of this being exhibited by CSR-17 and CSC-61 clinopyroxene (2 to 3 times PM, 10 times
605 $HREE_N$ contents, Fig. 4d). These profiles and correlations can be used to support the conclusion
606 that RP peridotites have been melted more extensively and more strongly metasomatized than
607 those of KH. However, water contents in RP peridotite minerals are generally lower than those
608 from KH Group 1 and do not correlate with typical metasomatism indices such as clinopyroxene
609 modal abundance or LREE/HREE ratios (Fig. 6f). Pyroxenite xenoliths are abundant at RP and
610 likely represent crystallized melts or melt cumulates that formed at mantle depth (Porreca et al.,
611 2006). Evidence from RP xenoliths showing cm-wide pyroxenite veins cross cutting lherzolite
612 (Porreca et al., 2006), and the fact that two RP lherzolites are devoid of metasomatic signatures

(LREE-depleted profiles in Fig. 4d and f) suggest that metasomatism could have been heterogeneous and localized in its chemical effects at the dm scale. Moreover, even if these peridotites come from the RP volcanic field, the xenoliths were sampled at four different volcanic necks (labeled CN, CSC, CSR and CTON in Table 1), and thus were brought to the surface by different host magmas. Hence, each of the host magmas could sample a localized volume of the mantle lithosphere beneath RP. It is possible that the complex melting-metasomatic history of the RP xenolith suite has erased any trends with water, given that these xenoliths may be random samples of a metasomatized mantle that is heterogeneous at the dm scale.

6.2.2. Estimating the degree of melting

The degree of melting (F) for each peridotite is estimated by modelling the behavior of HREE concentrations in clinopyroxene (Fig. 9, Table SI7). Two other methods of estimating the degree of melting are described in SI3 (1) comparing to major element modelling based on the approach of Herzberg (2004), and (2) based on the Cr# of spinels (Hellebrand et al., 2001).

The degree of melting of the KH and RP peridotites is estimated using the Yb and Y content of clinopyroxene. Trends representing of incremental batch melting models are used in Fig. 9 because this is the most realistic style of melting in the upper mantle (Asimow and Longhi, 2004; Herzberg, 2004; Langmuir et al., 1993; Walter et al., 1995). Equation A7 from Johnson et al. (1990) for modelling a trace element concentration in a mineral during non-modal batch melting was used, but in steps of 1% of melting to model incremental batch melting: the bulk-rock concentration obtained for the residue at each 1% step was used as a new initial bulk-rock concentration for the next 1% melting step. The modal proportions of starting phases (i.e. those of KIL72) and melting phases (Johnson et al., 1990) are given in Table SI8. Partition coefficients used are in Table SI8 (Adam and Green, 2006; Beattie, 1994; Elkins et al., 2008; Fujimaki et al.,

1984; Gaetani et al., 2003; Green et al., 2000; Johnston and Schwab, 2004; McKenzie and O'Nions, 1991; Nielsen et al., 1992; Salters et al., 2002; Salters and Longhi, 1999). Three initial compositions are tested (Fig. 9): depleted mantle (DM), PM (McDonough and Sun, 1995; Workman and Hart, 2005; Table SI9) and that of our most fertile lherzolite KIL72, which has a flat REE pattern relative to PM (Fig. SI4b). Some KH lherzolites have higher Al_2O_3 and HREE contents than the DM. All KH Group 1 lherzolites, some of which are at least as fertile for major elements and HREE as the DM, have depleted LREE patterns in clinopyroxene (Fig. 4a and SI4a). This indicates that these peridotites experienced melting from a protolith that was more fertile than DM, and that using DM as an initial composition would underestimate the degree of melting. Moreover, KH Group 1 peridotites are more fertile than most abyssal peridotites (Fig. 9), generally thought to be residues of melting of the DM (Hellebrand et al., 2002; Johnson et al., 1990; Seyler et al., 2004; Warren, 2016). Consequently, a PM-like initial composition seems more realistic for KH peridotites. Using a PM initial composition or that of KIL72, the Y and Yb contents of KH and RP clinopyroxenes can be modelled by up to 20 and 22 % incremental batch melting, respectively (Fig. 9). The degree of melting that is used in Fig. 10 is consequently calculated with the clinopyroxene Y and Yb contents of KIL72, which has a composition close to that of the PM. Finally, the clinopyroxene HREE contents of harzburgites and the dunite may have been affected by sub-solidus equilibration while that effect is negligible for lherzolites with > 6.5 wt % clinopyroxene (Sun and Liang, 2014). Sub-solidus re-equilibration in spinel peridotites with low modal clinopyroxene results in a 2 to 3 times increase of the Ho to Lu contents in clinopyroxene (Sun and Liang, 2014). From this amount of increase, it is estimated that the degrees of melting calculated for the harzburgites and dunite in KH and RP using the clinopyroxene Yb contents may

be under-estimated by up to ~10 %. These are illustrated as positive error bars of F = 0.1 for harzburgites and the dunite in Fig. 10.

Modelling of the entire clinopyroxene trace element patterns is shown in Fig. SI4. Lherzolites from KH Group 1 and RP lherzolites CSR-20 and CSC-16 have LREE depleted patterns that can be matched by melting models. For KH Group 2 and the other RP peridotites, however, only the HREE can be modelled using melting equations. In summary, based on both major and trace element considerations it appears that KH peridotites have undergone 1 – 20% melting with Group 2 peridotites all showing signs of subsequent metasomatism, while RP peridotites underwent 5 – 22% melting and all but two have been metasomatized after melt depletion (Fig. SI4, Table SI7).

6.2.3. Modelling water contents during melting

6.2.3.1. Parameters and equations for melting models

To model water content variations in pyroxene, olivine and bulk-rock during melting, batch and incremental batch melting equations are used (Johnson et al., 1990; Shaw, 2005). Nernst partition coefficients for water used in this study are 0.0016, 0.0144, and 0.0174 for $D_{H2O}^{ol/melt}$, $D_{H2O}^{opx/melt}$, and $D_{H2O}^{cpx/melt}$ (Table SI10), respectively, based on average experimental D values. Only experiments that produced at least two nominally anhydrous minerals in addition to glass and did not contain hydrous phases (mica, amphibole) were selected (Aubaud et al., 2004; Hauri et al., 2006; Tenner et al., 2009). These choices aim at experiments that represent melting of a spinel or garnet peridotite with residual olivine, clinopyroxene, and/or orthopyroxene. Moreover, the range of experimental $D_{H2O}^{cpx/melt}$ (0.012-0.025; Aubaud et al., 2004; Hauri et al., 2006; Tenner et al., 2009) is similar to that calculated using the composition of KH and RP clinopyroxenes with the method

of O'Leary et al. (2010): $D_{H2O}^{cpx/melt}$ = 0.010-0.019. Trends for batch and incremental batch melting models are shown in Fig. 10.

6.2.3.2. Comparing measured water contents with melting models

The curves for incremental batch melting using an initial water content of 1100 ppm H_2O, or for batch melting using 570 ppm H_2O pass though the bulk-rock water contents of KH Group 1 peridotites (Fig. 10a). Using the lowest and highest water partition coefficients and batch melting models allows to reproduce the water content of 9 out of 12 KH Group 1 lherzolites. Using initial water contents of 200-1000 ppm H_2O allows to encompass all but one KH Group 1 lherzolites and one KH Group 2 harzburgite data with batch melting equations (pink curves in Fig. 10a). An initial water content of 570-1100 ppm H_2O is within the range of estimates of the water content of the PM of 330-1100 ppm H_2O but higher than the 150-200 ppm H_2O typically assumed for the DM (Dixon and Clague, 2001; Palme and O'Neill, 2003). Three out of 5 Group 2 peridotites have water contents that are too high for their inferred degree of melting (Fig. 10a). However, using these same initial water contents of 570 or 1100 ppm H_2O, the water contents of clinopyroxenes appear too high, while those of orthopyroxene and olivine are too low compared to the melting models (Fig. 10b-d). This observation leads us to hypothesize that the distribution of water between mantle minerals as measured in peridotites is not solely derived from melting (and metasomatic) processes but is also reflects subsequent sub-solidus re-equilibration.

6.2.3.3. Sub-solidus equilibration of water between peridotite minerals

In addition to the mismatch between measured and modelled water contents in minerals from minimally metasomatized peridotites like these from KH Group 1, another observation supports the hypothesis of sub-solidus equilibration in the distribution of water in mantle minerals.

The average clinopyroxene/orthopyroxene, clinopyroxene/olivine and orthopyroxene/olivine water content ratios ($\frac{[H_2O]_{cpx}}{[H_2O]_{opx}}$, $\frac{[H_2O]_{cpx}}{[H_2O]_{ol}}$,and $\frac{[H_2O]_{opx}}{[H_2O]_{ol}}$) in KH peridotites are 2.5, 43.8 and 17.3, respectively. This is in poor agreement with water partitioning experiments run at solidus conditions (Fig. 6d, Table SI10) where for instance typical $\frac{[H_2O]_{cpx}}{[H_2O]_{opx}}$ ratios are 1.4-1.7 (Aubaud et al., 2004; Demouchy and Bolfan-Casanova, 2016; Hao et al., 2014; Hauri et al., 2006; Peslier, 2010; Peslier and Bizimis, 2015; Peslier et al., 2017; Tenner et al., 2009; Warren and Hauri, 2014). For example, experiment B394 from Hauri et al. (2006) is a good analogue to the KH mantle (Table SI10): they used a KH peridotite as their starting material for that experiment; it has olivine, clino-and orthopyroxene in equilibrium (Gaetani and Grove, 1998). Moreover, the experiment was run without addition of water under temperatures and pressures approximating those of the shallow lithosphere (Gaetani and Grove, 1998). The resulting $\frac{[H_2O]_{cpx}}{[H_2O]_{opx}}$, $\frac{[H_2O]_{cpx}}{[H_2O]_{ol}}$,and $\frac{[H_2O]_{opx}}{[H_2O]_{ol}}$, however are 1.4, 9.2 and 6.5, respectively (Gaetani and Grove, 1998; Hauri et al., 2006). We suggest that sub-solidus reequilibration is responsible for the discrepancy between measured mineral/mineral water content ratios from mantle xenoliths and those derived from experiments ran at solidus conditions.

Trace and major elements can be redistributed between clinopyroxene and orthopyroxene during sub-solidus cooling depending on their diffusion rates (e.g., Buseck et al., 1980; Sun and Liang, 2014). The high proportion of modal clinopyroxene in most KH and RP peridotites (> 6.5 %, Table 1) makes it unlikely that REE were significantly affected in these samples during sub-solidus cooling (Sun and Liang, 2014). On the other hand, Ca/Mg ratios of orthopyroxene and clinopyroxene ($\frac{(\mathrm{Ca/Mg})\mathrm{opx}}{(\mathrm{Ca/Mg})\mathrm{cpx}}$) in most natural peridotites, including the ones studied here, are lower than those from experiments run at the solidus (Brey and Köhler, 1990). Major element

compositional changes are likely to influence the distribution of water between clino- and orthopyroxenes. Moreover, H being one of the fastest diffusing elements in mantle minerals, re-distribution during sub-solidus cooling is expected (e.g., Chakraborty, 2010; Cherniak and Dimanov, 2010; Demouchy et al., 2017; Farver, 2010). The higher $\frac{[H_2O]_{cpx}}{[H_2O]_{opx}}$ ratios in naturally equilibrated peridotites compared to experiments run at the peridotite solidus (Fig. 6d) would thus signify sub-solidus re-equilibration of water.

In order to quantify the effect of sub-solidus re-equilibration on water distribution among peridotite minerals, a method based on the change in pyroxene composition upon cooling is used here. First, the cation Ca/Mg ratio of orthopyroxene and clinopyroxene is calculated for each sample. This ratio is chosen because the sub-solidus exchange of Mg and Ca between orthopyroxene to clinopyroxene is well established (Brey and Köhler, 1990): during cooling, diopside becomes increasingly richer in Ca relative to Mg while Ca is lost relative to Mg in enstatite. In addition, the measured Ca and Mg abundances in pyroxene have a low analytical uncertainty because they are significantly above detection limits of the electron microprobe. The orthopyroxene Ca/Mg ratio is divided by that of clinopyroxene ($\frac{(\mathrm{Ca/Mg})\mathrm{opx}}{(\mathrm{Ca/Mg})\mathrm{cpx}}$) for all peridotites as well as for selected laboratory experiments (Table SI10). The three experiments selected (one from Aubaud et al., 2004, and two from Hauri et al., 2006) were performed at ≤ 2 GPa, and comprise olivine, clinopyroxene, orthopyroxene and glass (i.e. melt) in equilibrium, but no garnet, so the conditions are as close as possible to those of the spinel peridotites studied here, and all phases were analyzed for water (Table SI10). Next, $\frac{(\mathrm{Ca/Mg})\mathrm{opx}}{(\mathrm{Ca/Mg})\mathrm{cpx}}$ is plotted against the experiment or peridotite equilibration temperatures (Brey and Köhler, 1990; Fig. 11a). The following linear regressions are obtained (Fig. 11a):

745 $$\frac{(Ca/Mg)_{opx}}{(Ca/Mg)_{cpx}} = 0.00020 \times T - 0.19130$$ for KH + experiments (eq. 2)

746 $$\frac{(Ca/Mg)_{opx}}{(Ca/Mg)_{cpx}} = 0.00016 \times T - 0.13797$$ for RP + experiments (eq. 3)

747 with Ca and Mg concentrations in afu and T, the temperature, in °C. The sole purpose of
748 equations 2 and 3 is to calculate the $\frac{(\mathrm{Ca/Mg})\mathrm{opx}}{(\mathrm{Ca/Mg})\mathrm{cpx}}$ ratio at the peridotite solidus (~1400 °C; the
749 temperature at which the ridge adiabat intersects with the solidus of a peridotite containing 300-
750 1000 ppm H_2O; Hirschmann, 2006): $\left(\frac{(\mathrm{Ca/Mg})\mathrm{opx}}{(\mathrm{Ca/Mg})\mathrm{cpx}}\right)_{solidus} = 0.0901 \pm 0.0073$ for KH and
751 $\left(\frac{(\mathrm{Ca/Mg})\mathrm{opx}}{(\mathrm{Ca/Mg})\mathrm{cpx}}\right)_{solidus} = 0.0874 \pm 0.0104$ for RP. The error on these ratios is the standard error
752 predicted at a given temperature from the regressions through the data resulting in equations 2 and
753 3.

754 Then, $\frac{(\mathrm{Ca/Mg})\mathrm{opx}}{(\mathrm{Ca/Mg})\mathrm{cpx}}$ is plotted against the ratio of water contents in orthopyroxene and
755 clinopyroxene, $\frac{[H_2O]_{opx}}{[H_2O]_{cpx}}$, for each xenolith location, along with those from experiments, in order to
756 calculate $\frac{[H_2O]_{opx}}{[H_2O]_{cpx}}$ at the solidus (Fig. 11b). A separate least squares regression is calculated for
757 each xenolith location (+ experimental data) to ensure that different sub-solidus cooling histories
758 and relationships between water partitioning and pyroxene composition have a minimal effect on
759 the regression. The least squares regression of the KH and RP data with experimental data (Fig.
760 11b) are:

761

762 $$\frac{[H_2O]_{opx}}{[H_2O]_{cpx}} = 5.2495 \times \frac{(Ca/Mg)_{opx}}{(Ca/Mg)_{cpx}} + 0.3009$$ for KH + experiments (eq. 4)

763

764 $$\frac{[H_2O]_{opx}}{[H_2O]_{cpx}} = 5.2238 \times \frac{(Ca/Mg)_{opx}}{(Ca/Mg)_{cpx}} + 0.2985 \quad \text{for RP+ experiments} \quad \text{(eq. 5)}$$

765

766 Using equation 4 and 5 and the $\left(\frac{(\mathrm{Ca/Mg})\mathrm{opx}}{(\mathrm{Ca/Mg})\mathrm{cpx}}\right)_{solidus}$ (calculated at 1400°C with equation 2

767 and 3), $\frac{[H_2O]_{opx}}{[H_2O]_{cpx}}$ ratios at the solidus ($\left(\frac{[H_2O]_{opx}}{[H_2O]_{cpx}}\right)_{solidus}$) are calculated to be 0.774 ±0.096 and 0.755

768 ±0.116 for KH and RP respectively. Similarly, a $\left(\frac{[H_2O]_{ol}}{[H_2O]_{cpx}}\right)_{solidus}$ of 0.105 ±0.015 for KH is

769 calculated by plotting $\frac{(\mathrm{Ca/Mg})\mathrm{opx}}{(\mathrm{Ca/Mg})\mathrm{cpx}}$ against the ratio of water contents in olivine and clinopyroxene,

770 $\frac{[H_2O]_{ol}}{[H_2O]_{cpx}}$, and obtaining a linear regression (Fig. 11c). This is only done for KH data because olivines

771 from RP have lost most and, in some xenoliths, all their water during xenolith ascent.

772 Finally, in order to redistribute water between pyroxenes and olivine to concentrations that

773 more accurately represent solidus conditions appropriate for comparison to melting models, a

774 coefficient x_{sseq}, referred to here as the equilibrium factor, is calculated for each sample using the

775 following equation:

776 $$\left(\frac{[H_2O]_{xls}}{[H_2O]_{cpx}}\right)_{solidus} = \frac{[H_2O]_{xls} \times x_{sseq}}{[H_2O]_{cpx}/x_{sseq}} \quad \text{(eq. 6)}$$

777 with $[H_2O]_{xls}$ equal to the measured water contents of orthopyroxene or olivine, $[H_2O]_{cpx}$

778 equal to the measured water contents of clinopyroxene, and $\left(\frac{[H_2O]_{xls}}{[H_2O]_{cpx}}\right)_{solidus}$ equal to the ratio of

779 water between orthopyroxene or olivine and clinopyroxene at 1400 °C (calculated with equations

780 2-5). To solve for x_{sseq}, the equation can be rearranged to:

781 $$x_{sseq} = \sqrt{\frac{\left(\frac{[H_2O]_{xls}}{[H_2O]_{cpx}}\right)_{solidus} \times [H_2O]_{cpx}}{[H_2O]_{xls}}} \quad \text{(eq. 7)}$$

782 For each sample, orthopyroxene and olivine water contents can be multiplied by $x_{sseq}^{opx/cpx}$
783 or $x_{sseq}^{ol/cpx}$, and clinopyroxene water content can be divided by $x_{sseq}^{opx/cpx}$ to obtain their water
784 concentrations $[H_2O]_{xls}^{solidus}$ at liquidus temperature prior to sub-solidus re-equilibration (Solidus
785 H_2O in Table 1).

786 Examination of the corrected water contents warrant a couple remarks. First, the timescales
787 involved in sub-solidus re-equilibration in the mantle are too long to preserve any water content
788 zoning in the peridotite mantle. Second, the corrected olivine water contents (15-25 ppm H_2O) are
789 close but lower than olivine water contents at saturation at 1.3 GPa and 950ºC (30-40 ppm H2O)
790 obtained from solubility experiments (Padrón-Navarta and Hermann, 2017), consistent with the
791 lack of hydrous phases in the KH and RP peridotites. Now, the discrepancy between the $\frac{[H_2O]_{cpx}}{[H_2O]_{opx}}$
792 ratio measured in natural peridotites (~2 for a worldwide database, Fig. 6d) and that obtained from
793 experiments (~1.2—1.7) can be addressed again (Aubaud et al., 2004; Demouchy and Bolfan-
794 Casanova, 2016; Hao et al., 2014; Hauri et al., 2006; Peslier, 2010; Peslier and Bizimis, 2015;
795 Tenner et al., 2009; Warren and Hauri, 2014). If the water content of KH pyroxenes and olivine
796 are corrected for sub-solidus re-equilibration, then the average $\frac{[H_2O]_{cpx}}{[H_2O]_{opx}}$, $\frac{[H_2O]_{cpx}}{[H_2O]_{ol}}$,and $\frac{[H_2O]_{opx}}{[H_2O]_{ol}}$ in KH
797 and RP peridotites are 1.4, 10.2 and 7.4, consistent with the ratios from experiment B394 (1.4, 9.2
798 and 6.5 respectively, Table SI10; Hauri et al., 2006). The higher $\frac{[H_2O]_{cpx}}{[H_2O]_{opx}}$ ratio in natural peridotites
799 compared to that of experiments is a result of sub-solidus re-equilibration. Consequently, measured

800 water concentrations need to be corrected to reflect initial water concentrations at the solidus prior
801 to modeling water content variations in mantle minerals, as examined next.

802 6.2.3.4. Comparing sub-solidus corrected water content to melting models

803 The batch and fractional melting models described earlier are now compared to the water
804 contents of the peridotite minerals, corrected for sub-solidus equilibration (Fig. 10e-g). Using an
805 initial water content of 570 ppm H_2O results in batch melting models that match well the bulk-
806 rock water content of KH Group 1 lherzolites as pointed out in section 6.2.3.2. But now, the batch
807 melting models also reproduce well the water contents of clinopyroxene, orthopyroxene and
808 olivine after they have been corrected for sub-solidus equilibration. The clinopyroxene and olivine
809 water contents, once corrected for sub-solidus equilibration, are also better centered on the curves
810 for incremental batch melting models. Within KH Group 2, the water contents of all but one of the
811 peridotites are too high to be predicted by the melting models for all minerals.

812 With the exception of two lherzolites (CSR20 and CSC16) which both have LREE-
813 depleted patterns (clinopyroxene $Ce/Yb_N < 0.03$, Fig. 4d and f), the water contents of RP
814 peridotites except two are also too high to be explained by melting. The water contents of these
815 two RP peridotites, corrected for sub-solidus equilibration, can be modelled by incremental batch
816 melting and a wide range of initial water contents, 300 to 1100 ppm H_2O (Fig. 10e-g), i.e. estimated
817 range for the water content of the PM (Dixon and Clague, 2001; Palme and O'Neill, 2003). This
818 suggests that depleted peridotites CSR20 and CSC16 could have had their water content controlled
819 only by melting processes and no metasomatic addition.

820 In summary, the water contents of KH Group 1 lherzolites can be reproduced by melting
821 models, but the water content of most KH Group 2 peridotites are too high to be accounted for by

822 melt depletion. The water contents of all but two peridotites from RP are too high to be derived
823 from partial melting. This excess water must reflect some other process(es) that has added water
824 to most RP and a minority of KH peridotites. In the next two sections, metasomatism is considered
825 as the mechanism that could have enriched these peridotites in water.

826 6.2.4. Metasomatism along the Rio Grande Rift

827 This section aims at modelling trace element behavior, including that of water, during
828 metasomatic processes, defined as compositional changes brought upon the peridotite by
829 percolating mantle melts. The effects can be cryptic, i.e. only changes in the most incompatible
830 trace elements, and this is the best explanation for most of the compositions of the KH and RP
831 metasomatized peridotites. Metasomatism can also be modal, although this is only evidenced here
832 in peridotite KH96-08 (Harvey et al., 2012), as discussed in section 6.2.2. Finally, the pyroxenites
833 could be crystallized metasomatic melts. We define below a peridotite-melt interaction process in
834 which a mantle melt ascends through the upper mantle and undergoes assimilation and fractional
835 crystallization (AFC) by reacting with melting residues (peridotite pre-metasomatism). The melt
836 resulting from the AFC process then cryptically metasomatizes the peridotite locally near the melt
837 channels, possibly by seeping along grain boundaries and adding via diffusion incompatible trace
838 elements into the peridotite minerals. Hence, in order to constrain what types of melts could have
839 metasomatized the KH and RP peridotites for water, trace element evolution during peridotite-
840 melt interaction is modelled using the compositions of representative mantle melts from a variety
841 of tectonic settings. The origin of the pyroxenites is also examined in this section. This is then
842 followed by modelling of variations in water content in the minerals of metasomatized peridotites
843 during these processes.

844 6.2.4.1 Trace element modelling of peridotite-melt interaction

845 To constrain the origin of the metasomatic agents in KH and RP xenoliths, the peridotite-
846 melt interaction model can be broken into 3 steps, similar to what has successfully been used to
847 model the composition of Hawaiian peridotite xenoliths (Bizimis et al., 2004). Step 1: the "pre-
848 metasomatic" trace element pattern of each peridotite is calculated by applying incremental batch
849 melting equations to the trace element composition of KIL72. For each peridotite, the degrees of
850 melting (F) determined earlier using Yb-Y content of clinopyroxene is used. Step 2: the AFC
851 equation 6a of DePaolo (1981) is applied using these residue compositions and that of a mantle
852 melt to obtain the composition of a melt resulting from AFC. Step 3: the melt resulting from the
853 AFC process (hence “AFC melt”) is assumed to metasomatize the peridotite, a process modelled
854 via simple mixing. Six different mantle melt compositions are tested as potential metasomatic
855 agents: 1 - mid-ocean ridge basalt (MORB; Klein, 2003), 2 – melt in equilibrium with a primitive
856 mantle (McDonough and Sun, 1995) composition (PMM), 3 - arc basalt (ARC; Plank, 2005), 4 -
857 silicate slab melt (SM, Rapp et al., 1999), 5 - continental carbonatite melt (CC; Bizimis et al.,
858 2003), and 6 - deep subduction zone carbonatite melt (SZC; Walter et al., 2008). The trace element
859 compositions of these are shown in Fig. 12a and Table SI9. For the carbonatite melts (SZC and
860 CC), partition coefficients for carbonatite melt-silicate solid systems (Table SI8) are applied when
861 available (Blundy and Dalton, 2000; Green et al., 1992; Klemme et al., 1995; Sweeney et al.,
862 1995). For the AFC modeling, a value of 0.99 for r, the ratio of assimilated mass to newly
863 crystallized mass, is applied (Bizimis et al., 2004) and f, the mass of the magma to the initial mass
864 of the magma, is varied to optimize the match between model and data, and ranges from 0.2 to
865 0.99 (Table SI7). All samples for which water contents could not be explained by melting models
866 or for which trace element patterns are LREE enriched (i.e., KH Group 2 and all RP peridotites

except CSR-20 and CSC-16, Fig. SI4 b and c) were modelled in this manner. The results of the peridotite-melt interaction modelling are in Fig. 12 and Table SI7.

The clinopyroxene trace element profiles of KH Group 2 xenoliths are best reproduced by peridotite-melt interaction models using either 0.03-0.14 % SZC "AFC melt", or 0.5-2 % SM "AFC melt" (Fig. 12b-f). Silicate and carbonatitic metasomatism has been inferred previously in KH peridotites (Harvey et al., 2012). The only element that has an obvious mismatch between observed and modeled compositions is Sr, which exhibits a negative anomaly in models using SZC. This melt composition represents carbonatitic melts at pressures higher (6-7 GPa; Walter et al., 2008) than those at which the KH peridotites equilibrated (~1.5 GPa). The Sr anomaly in the SZC melt may have been generated by large ion lithophile elements like Sr being lost to fluids, melts or supercritical melts during oceanic crust subduction (Walter et al., 2008). Given that $D_{Sr}^{solid/melt}$ increases with increasing pressure (Kessel et al., 2005), the lack of Sr anomalies in the KH peridotites may signify that the melts metasomatized the mantle beneath KH at lower pressures than those at which the SZC melt were formed (Walter et al., 2008).

The trace element patterns of clinopyroxene in the metasomatized RP xenoliths are best reproduced by peridotite-melt interaction models using 0.2-3 % "AFC melt". Those from CRS17 and CSC61 may also be reproduced with 0.15-0.2 % SZC "AFC melt", with the caveat again of mismatching the Sr negative anomaly (Fig. 12 j-l). Those from CN105, CSC14 and CN4 may be modelled using 0.01-0.07 % CC "AFC melt", characterized in particular by negative Zr and Hf anomalies in PM normalized trace element profiles (Fig. 12 g-i). Silicate metasomatism linked to subduction processes and carbonatite metasomatism has previously been identified in RP mantle xenoliths (Perkins et al., 2006; Porreca et al., 2006).

889 Overall, the trace element compositions of clinopyroxenes from KH Group 2 and RP
890 metasomatized peridotites are reproduced successfully by peridotite-melt interaction models either
891 involving ≤ 0.2% carbonatite melts or 0.2-3 % subduction-related silicate melts.

892 6.2.4.2 Origin of the pyroxenites

893 Pyroxenites are often considered to represent a locally crystallized mantle melts,
894 cumulates, or the result of modal metasomatism by peridotite-melt reaction (e.g., Downes, 2007;
895 Porreca et al., 2006). Melts in equilibrium with KH clinopyroxenites have trace element
896 concentrations as high as those of carbonatite melts (Fig. 12a). The clinopyroxene trace element
897 profiles of KH Group 2 peridotites can be matched by peridotite-melt interaction models using the
898 composition of a melt in equilibrium with KH pyroxenites (Fig. 12b-f), suggesting that KH
899 pyroxenites represent crystallized metasomatic melts.

900 Clinopyroxene, orthopyroxene, and bulk-rock trace element compositions of websterite
901 CTON-53, on the other hand, are lower than all metasomatized RP peridotites (Fig. 4d-f). Melts
902 in equilibrium with CTN53 are also lower in trace elements than any of the mantle melt
903 compositions from the literature used here (Fig. 12a). This websterite, therefore, does not represent
904 a crystallized metasomatic melt. Peridotite-melt interaction models best reproduce the CTN53
905 clinopyroxene trace element pattern with 0.04 % PMM or 0.06 % SM (Fig. SI5).

906 The next section considers the amount of water that these melts may have added by
907 metasomatism in the context of the models just discussed.

908 6.2.5. Effects of metasomatism on water contents of the Rio Grande Rift mantle

909 6.2.5.1: Modelling water contents during peridotite-melt interaction

In the KH and RP peridotites that have water contents too high to be explained by melting alone (Fig. 10), water must have been added during later enrichment(s), perhaps during the same metasomatic event(s) that produced the other incompatible trace element enrichments (e.g., Doucet et al., 2014; Peslier et al., 2012), consistent with our trace element modelling of peridotite-melt interaction (Fig. 12). Figure 13 shows the sub-solidus-corrected water contents of pyroxenes for those xenoliths that have other petrologic or trace element evidence of metasomatism (KH Group 2, and RP peridotites except CSR-20 and CSR 16). A three-step peridotite-melt interaction model, in the same manner as performed above for the other trace elements, is applied to reproduce the water contents of the metasomatized peridotites. Starting peridotite compositions are assumed based on the incremental batch melting models with an initial content in the solid C_0 = 1100 ppm H_2O at various degrees of melting (Step 1). This depleted peridotite composition then interacts with a melt via AFC, producing an "AFC melt" (Step 2). The water content of this "AFC melt" is then added by simple mixing calculation to that of the depleted peridotite, using the % added established during the modelling of the other trace elements (section 5.2.4.1) and increasing the water content of the melt until the water contents of the peridotites' pyroxenes is matched (Step 3). The models are compared to the sub-solidus-corrected water contents of metasomatized KH and RP peridotites because it is assumed that the melts were percolating through the lithospheric mantle at a temperature close to the peridotite solidus. Interactions with pyroxenite melts, then with silicate melts, finally with carbonatitic melts are modelled. Results are illustrated in Fig. 13, summarized in Table SI7, and detailed below.

First the water contents of melts in equilibrium with KH or RP pyroxenites are used in the peridotite-melt interaction models. A melt in equilibrium with the KH pyroxenites contains 1.67 wt% H_2O on average. Between 0.35 and 0.7 % of a KH pyroxenite "AFC melt" needs to be added

933 (Step 3) to reproduce the range of water contents in the pyroxenes of KH Group 2 peridotites
934 (purple curves in Fig. 13a and b). Similarly, addition of 0.15 to 0.35 % of a RP pyroxenite "AFC
935 melt" (Step 3) using the composition of a melt in equilibrium with the RP websterite (CTON53,
936 3.24 wt% H_2O) can reproduce the range of water contents in pyroxenes of the RP metasomatized
937 peridotites (orange curves in Fig. 13c and d).

938 Second, the water contents of various melts were tested in peridotite -melt interaction
939 models using the percentage of added carbonatite melts obtained in the modelling illustrated in
940 Fig. 12. Using the average percentage carbonatite melt added that is necessary to reproduce the
941 trace element patterns of KH Group 2 peridotites (0.1 %), the metasomatizing melt needs to contain
942 6.5 to 11 % H_2O to match the water contents of pyroxene in the KH Group 2 peridotites (light blue
943 curves in Fig. 13 a and b). Similarly, with the percentage of added carbonatite melt obtained in the
944 peridotite-melt interaction models of Fig. 12, 1.7 wt. % (for 0.2 % added SZC) and 20 wt. % (for
945 0.03 % added CC) H_2O are necessary to even start matching the lowest pyroxene water contents
946 of the metasomatized RP peridotites (light blue curves in Fig. 13 c and d). Although the lowest
947 water contents (1.7 and 6.5 wt% H_2O) are possible for mantle melts, the highest water contents
948 (>7% H_2O) are unrealistic and would be higher than that of most mantle melts. For example, an
949 average of 4 % H_2O is observed in subduction zone melts, which are thought to be among the
950 wettest (Plank et al., 2013). Consequently, even if metasomatism by carbonatite melts likely
951 occurred in the KH and RP mantle lithosphere, they are not the main providers of the added water
952 because the amount of water that they would need to contain seems to be unrealistically high.
953 Addition of water by carbonatite melts may be a viable mechanism if, instead of a single-stage or
954 closed-system event as modelled here, the melts are added in quasi-continuous flow in an open

955 system until the amount of water observed in the metasomatized peridotites can be added from
956 melts with reasonable amounts of water.

957 Finally, the water content of the metasomatizing melt is varied in peridotite-melt
958 interaction models using the % of SM melt obtained for each peridotite in Fig. 12 until their water
959 content can be reproduced (Fig. 13, Table SI7). The water contents of the melts that metasomatized
960 the KH Group 2 peridotites are thus estimated to range from 0.4 to 0.7 wt. % H_2O (green curves
961 in Fig. 13 a and b). The melts that metasomatized the RP peridotites would have had a wider range
962 of water contents, from 0.25 wt.% H_2O (for example with 3 % added melt, yellow curves in Fig.
963 13 c and d) to 3 wt.% H_2O (for example with 0.2% melt added, green curves in Fig. 13 c and d).
964 This range is similar to the 0.5-2 wt.% H_2O estimated for basalts along the Rio Grande Rift using
965 their Cl content (Rowe et al., 2015). No relationship is apparent between the water content of
966 metasomatized RP peridotites and their provenance from different volcanic necks (CS, CSR, CSC,
967 Fig. 13 c-d). For example, peridotites from CSR have the lowest and highest pyroxene water
968 contents of the dataset and also include one of the un-metasomatized RP peridotite (CSR-20 with
969 no water detected). The host basalts erupted at each volcanic neck consequently sampled variously
970 metasomatized and rehydrated lithospheric mantle. The presence of contrasting metasomatic
971 signatures at the one locality suggests that the mantle lithosphere beneath RP is heterogeneously
972 metasomatized and variably enriched in water at scales smaller than those of the host volcanic
973 systems.

974 On average, the metasomatizing melts at RP (1.06 ± 1.03 wt.% H_2O) would have carried
975 about twice as much water as those at KH (0.56 ± 0.17 wt.% H_2O). With these constraints on water
976 and trace element metasomatic agents that enriched these peridotites, xenolith geochemistry can
977 now be related to the tectonic processes that affected the KH and RP regions of the mantle.

978 6.2.5.2 Illustration of peridotite-melt interaction in a harzburgite with a clinopyroxenite
979 vein

980 Petrologic evidence for the metasomatizing process can be seen in veined harzburgite
981 KIL41. Measured mineral compositions reflect increases of incompatible elements Al in pyroxene
982 and Fe in olivine (Fig. 2f-h) and decreases of Cr in spinel (Fig. 2b) towards the vein that can be
983 interpreted as reaction between melt and harzburgite. The water contents measured in the
984 clinopyroxene increases from harzburgite to clinopyroxenite vein (Fig. 2c). However, the water
985 contents measured in the orthopyroxene and olivine decrease (Fig. 2d and e). In the vein, the water
986 preferentially partitions into clinopyroxene over olivine during crystallization due to $D_{H2O}^{cpx/melt}$ >
987 $D_{H2O}^{ol/melt}$ (Aubaud et al., 2004; Hauri et al., 2006). Assuming that the vein is composed of ~90 %
988 clinopyroxene and ~10% olivine (Fig. 2a), the water content of the vein amounts to ~350 ppm
989 H_2O, i.e. higher than that of the harzburgite (52 ppm H_2O). This is expected as melts should contain
990 more water than peridotites given the incompatible behavior of water in mantle processes. Along
991 the vein, modal metasomatism results in minerals of intermediate major element compositions
992 between that of the vein and harzburgite (Fig. 2b, f-h). The distribution of water in the "wall" along
993 the vein is also governed by the higher compatibility of water in clinopyroxene compared to
994 orthopyroxene and olivine, and only clinopyroxene records higher water contents than the
995 surrounding harzburgite. By the time the thin melt vein crystallized and cooled, no local re-
996 equilibration of water content had taken place because the sub-solidus temperatures were low
997 enough to prevent significant H diffusion, resulting in preservation of the decreasing water
998 contents of orthopyroxene and olivine towards the vein.

999 6.3. Evolution of the mantle lithosphere beneath the Rio Grande Rift

1000 6.3.1. Subduction processes

1001 Tectonic setting (e.g., DeCelles, 2004; Whitmeyer and Karlstrom, 2007), combined with
1002 the compositional evidence in peridotite xenoliths, has led previous workers to conclude that
1003 metasomatism in the mantle beneath the southwestern USA is related to subduction of the Farallon
1004 plate (Armytage et al., 2015; Byerly and Lassiter, 2012; Li et al., 2008; Perkins et al., 2006). The
1005 trace elements models for the KH and RP peridotites are also consistent with metasomatism by
1006 subduction-related melts (SM). In addition, metasomatized peridotites from both locations have
1007 evidence for carbonatite-related metasomatism: some subduction-related (SZC at KH and RP),
1008 some related to continental settings (CC at RP). Carbonatite melts in this region have been linked
1009 before to the Farallon plate subduction (Armytage et al., 2015; Ducea et al., 2005; Perkins et al.,
1010 2006; Porreca et al., 2006), a hypothesis consistent with our modelling of trace element patterns
1011 with SZC melts. Except in one peridotite (CSR-7, Fig. 12l), the trace element patterns of the
1012 peridotite clinopyroxenes could not be explained by interaction with melts that could have come
1013 from upwelled asthenosphere (MORB and PMM) as may have been expected from the location of
1014 RP and KH in a rift. The latter tectonic setting, however, may have played a role in heating the
1015 lithosphere and melting carbonatite already present in the lithosphere, which could explain that the
1016 trace element compositions of some of the RP xenoliths can be reproduced with interaction with
1017 CC melts (Fig. 12 g-i).

1018 In the region where flat-slab subduction occurred, melts derived directly from the slab may
1019 be more likely to reach the lithosphere than in regions where the angle of subduction is higher.
1020 This could explain why RP peridotites are more extensively and pervasively metasomatized than
1021 KH peridotites. This assumes that the relative numbers of metasomatized versus unmetasomatized
1022 peridotites at each location, as well as the high number of pyroxenites at RP (Porreca et al., 2006),

1023 is representative of their compositional and lithological distribution in the mantle lithosphere. The
1024 interpretation that compositional differences of the metasomatic agents are the result of different
1025 angles of slab subduction is consistent with prior xenolith studies from this region (Harvey et al.,
1026 2012; Perkins et al., 2006; Porreca et al., 2006). At RP, these melts appear to be more water-rich
1027 (up to 3 wt.% H_2O silicate slab-derived melts) than those at KH (< 0.8 wt.% H_2O) supporting the
1028 hypothesis of Humphreys et al. (2003) that flat-slab subduction allowed metasomatic agents that
1029 were more hydrous to interact with the southwestern USA mantle. Water-rich melts also hydrated
1030 and perhaps caused mantle lithosphere thinning of the Colorado Plateau (Li et al., 2008). However,
1031 despite evidence for wetter metasomatizing melts at RP compared to KH, the RP xenoliths are not
1032 more hydrated than the KH ones (Fig. 6g). This suggests that the hypothesized weakening and
1033 delamination of the lithosphere following more pervasive and wetter metasomatism at RP is an
1034 unlikely scenario.

1035 6.3.2. Kilbourne Hole Group 1: asthenosphere or lithosphere mantle

1036 The water contents in KH Group 1 peridotites can be used to test whether they represent
1037 recently emplaced asthenosphere, as hypothesized for peridotites of similar compositions from a
1038 xenolith site, Elephant Butte, located 50 km north of KH in the Rio Grande Rift (Byerly and
1039 Lassiter, 2012). First, the measured KH Group 1 water contents can be compared to those estimated
1040 for the asthenosphere, and second, the viscosity calculated using olivine water contents and flow
1041 laws in dislocation creep (Mei and Kohlstedt, 2000; Li et al., 2008) can be compared to western
1042 United States viscosity models (Dixon et al., 2004). The additional information provided by KH
1043 Group 1 water contents will help determine if KH peridotites are more similar to the lithosphere
1044 or the asthenosphere.

1045 The water contents of the asthenosphere (Fig. 14a) can be estimated using a variety of
1046 methods. Using H_2O concentrations in MORB and OIB indicate from 50 to >1000 ppm H_2O in
1047 their source in the asthenosphere (Dixon et al., 1997). Seismologial data suggest a minimum of
1048 100 ppm H_2O (Masuti et al., 2016). Electrical conductivity studies suggest 0 to 16 ppm H_2O in
1049 Pacific Ocean asthenosphere between depths of 50 – 100 km (Sarafian et al., 2015), or up to 100
1050 ppm H_2O in the continental mantle lithosphere, or between 100 and 900 ppm H_2O at depths of 200
1051 km (the shallowest depths calculated in Wang et al., 2008). In comparison with these estimates,
1052 the average bulk-rock water content of KH Group 1 peridotites is 98 ± 13 ppm H_2O, significantly
1053 below MORB-based estimates but within uncertainty for the estimates from seismology (Fig. 14a).
1054 It appears that overall KH Group 1 water contents are on the lower side of the estimates for those
1055 predicted to exist in the asthenosphere.

1056 The average global asthenosphere viscosity is thought to range between 2.7×10^{17} and $2 \times$
1057 10^{19} Pa.s (Craig and McKenzie, 1986; Hager, 1991; Larsen et al., 2005; Pollitz et al., 1998).
1058 Beneath the western United States, the asthenosphere appears to be less viscous than the average
1059 of global asthenosphere viscosity, with regional estimates ranging between $5 \times 10^{17} – 3 \times 10^{18}$ Pa.s
1060 at depths < 100 km (Dixon et al., 2004; Kaufmann and Amelung, 2000). These lower
1061 asthenosphere viscosity estimates in the western United States may be the result of higher water
1062 contents and temperatures relative to the global asthenosphere conditions (Dixon et al., 2004). The
1063 calculated viscosities of KH peridotites using the measured olivine water contents, a shear stress
1064 of 0.3 MPa, , the equilibration temperatures at 1.5 GPa (Brey and Köhler, 1990, see section 5.2)
1065 and a flow law for olivine aggregates (see SI 4; Li et al., 2008; Peslier et al., 2010) range from 2.3
1066 $\times 10^{20}$ to 9.5×10^{22} Pa.s (Table 1, Fig. 14a). Using a higher shear stress (0.6 MPa, Hansen and
1067 Warren, 2015) decreases the effective viscosities of ~ one log unit (Fig. SI6 a and b). In any case,

all KH peridotites record viscosities that are more than one magnitude higher than those of the asthenosphere (Fig. 14a, Fig. SI6), confirming that they come from the lithosphere.

Next the hypothesis that the Group 1 peridotites originally come from the asthenosphere but were recently emplaced in the lithosphere can be tested. The water content their olivines may have had in the asthenosphere may be calculated using reasonable temperatures at the lithosphere-asthenosphere boundary (LAB) beneath KH and the sub-solidus equations generated in Fig. 11. First, realistic pressure-temperature conditions the peridotites could come from near the LAB must be estimated. The LAB is estimated to be at 40 to 80 km depth beneath KH (Achauer and Masson, 2002; Cordell et al., 1991; Thompson et al., 2005). Using the geotherms for the KH area of Kil and Wendlandt (2004), this corresponds to temperatures of 850 to 1450 ºC. The lowest temperature is colder than the equilibration temperatures of KH peridotites, so is likely too low, and a 40 km thick lithosphere too thin, to be realistic. The highest temperature is higher than the peridotite solidus (~1400ºC) and thus is also not realistic. Temperatures of 1250- 1400 ºC are more realistic, being higher than equilibration temperatures for KH, lower than the solidus temperatures, and corresponding to ~62-70 km LAB depths.

Next, the water content that the olivine had at solidus conditions at these pressure-temperature conditions must be estimated. The olivine water content at 1400ºC has already been calculated above in our sub-solidus correction calculation. Similarly, the 1250ºC temperature is used in equation 2 to calculate a $\frac{(\mathrm{Ca/Mg})\mathrm{opx}}{(\mathrm{Ca/Mg})\mathrm{cpx}}$ ratio of 0.06. The latter ratio is then input in the equation of Fig. 11c to obtain a $\frac{[H_2O]_{ol}}{[H_2O]_{cpx}}$ ratio of 0.08. Then a $x_{sseq}^{ol/cpx}$ is calculated for each KH Group 1 peridotite (equation 7), from which the water content the olivines may have had at 1250ºC can be

calculated. The olivine water contents at 1250 and 1400ºC are about 0.3 to 3 times higher than the measured olivine water contents (Fig. 14b).

Finally, viscosity can be calculated using these new olivine water contents and these pressure-temperature conditions. The obtained viscosities are significantly lower than the ones at peridotite equilibration temperatures. But because the olivine water contents at 1250 and 1400ºC still largely overlap the range of those at equilibration temperatures (Fig. 14b), the main factor that influences the lowering of the viscosities relative to those at equilibration temperatures is temperature (Fig. SI6 c) more than olivine water content. These viscosities (Empty blue circles in Fig. 14a) overlap with those of the asthenosphere. Based on water content data, it is possible that the KH Group 1 peridotites were once part of the asthenosphere. This scenario, however, would necessitate lithospheric thicknesses of > 60 km to match the lower viscosities of the asthenosphere beneath the SW USA, i.e. thicker than those inferred by the slow seismic wave velocities detected beneath the northern Rio Grande Rift (Gao et al., 2004; Sosa et al., 2014; van Wijk et al., 2008; West et al., 2004).

In summary, KH peridotites are from the lithosphere. The hypothesis of a recent asthenospheric mantle material underplating the lithosphere beneath KH during rifting processes (hypothesis 2 in the introduction) cannot be dismissed for KH Group 1 based on water concentrations and calculated viscosities, but the range of pressure-temperature conditions for this scenario to have occurred are narrow (LAB > 62 km and < 70 km corresponding to temperatures of 1250-1400ºC using the geotherm beneath KH of Kil and Wendlandt (2004). Interestingly, another lithospheric peridotite suite, Jiande in the South China block, also seems to have water contents controlled by melting (Hao et al., 2014). Jiande is, however, located in a completely different tectonic setting, namely asthenospheric upwelling linked to activation of a fault between

two Proterozoic continental blocks, compared to KH where melting events could be linked to asthenospheric upwelling following rifting. Water contents controlled by peridotite melting are therefore not found exclusively in rift settings.

7. Conclusions

The KH peridotites are remarkable in two ways. First, most of them (KH Group 1) appear to have compositions primarily controlled by melting processes which is rare for continental mantle xenoliths (Menzies, 1983). Effects of sub-solidus equilibration can be corrected using a novel approach developed for this study, and primary water contents of these peridotites and their minerals can be recovered and modelled as the result of melting. Second, the minimal H loss from olivine during xenolith ascent in KH peridotites, which is exceptional for off-craton xenoliths, allows for calculation of bulk peridotite water content for the off-cratonic lithosphere (98±13 ppm H_2O), assuming these xenoliths are broadly representative of the lithospheric mantle in this region. Based on their water contents and calculated viscosities, KH peridotites come from the lithosphere. Two unmetasomatized peridotites from RP also appear to have compositions, including water contents, that can be explained by melting of a primitive mantle protolith.

Metasomatic processes are evidenced in both KH and RP xenoliths suites by enrichments of highly incompatible elements and water. This process apparently produced both cryptic metasomatism in the peridotites and pyroxenites by crystallization of mantle melts (KH) and peridotite-melt interaction (RP). Metasomatism is highly variable spatially, but the mantle lithosphere in the southern region of the Rio Grande Rift (KH) seems to have experienced less metasomatism than the northern region of the rift (RP) overall, again assuming that the studied suites are representative. The silicate and carbonatite metasomatism found in both groups is regionally associated with the subduction of the Farallon slab (Armytage et al., 2015; Ducea et al.,

2005; Perkins et al., 2006; Porreca et al., 2006). One or both of the RP metasomatic agents had up to 3 wt.% H_2O, while KH mantle was metasomatized by melts with significantly less water (< 0.8 wt.%) which is interpreted to be associated with flat-slab subduction beneath RP. In contrast, the lower water contents of metasomatizing melts at KH may be linked to steeper angles of subduction. This is consistent with the hypothesis put forth by Humphreys et al. (2003) that the flat-slab subduction of the Farallon slab enriched the lithosphere more in water relative to the regions that experienced steeper subduction zone angles. Despite metasomatic melts being more water-rich at RP compared to KH, however, the mantle lithosphere at RP does not have higher water contents than that at KH because of the different amount of metasomatic input at each location, as deduced from trace element modelling. The combination of melting and metasomatic processes resulted in a lithosphere beneath the Rio Grande Rift that is very heterogeneous in water content, from one peridotite in which no water could be detected to peridotites containing up to 120 ppm H_2O and pyroxenites with 227-400 ppm H_2O.

Acknowledgements

We thank Jane Silverstone for providing the Rio Puerco xenoliths. Detailed reviews by Jessica Warren and two anonymous reviewers greatly improved this manuscript. We also thank the editor of this special issue, James Day. This work was supported by NSF grants EAR #1118335 to AHP and ADB and OCE #1624310 to MB and AHP.

Figure caption

Figure 1. Topographic map of southwestern United States, showing the location of Kilbourne Hole (KH) and Rio Puerco (RP) xenolith localities and the major geological features of the area. Thick black dashed lines separate the region where flat-slab subduction occurred (flat-slab corridor) from where the subduction zone had steeper angles of subduction (steep angle subduction) from English et al. (2003) and Saleeby (2003). Location of where an anomalous slow seismic velocity was detected (e.g. Gao et al., 2004; West et al., 2004) shown as a thick red line. UT = Utah, CO = Colorado, AZ = Arizona, NM = New Mexico. Topographic map from GeoMapApp database.

Figure 2. a: Back-scattered electron mosaic image of a thin section of KIL41 showing harzburgite cross-cut by a clinopyroxenite vein. b: Spinel (SP) Cr# versus distance. c-e: Clinopyroxene (CPX), orthopyroxene (OPX) and olivine (OL) water contents versus distance. f-h: Pyroxene Al_2O_3 content and olivine Mg# versus distance. Distance is relative to the size of the vein that is estimated to have an average width of 4000 μm, and its wall an average width of 2000 μm from observations of three thin sections of KIL41. The concentrations shown here are averages of numerous analyses by FTIR and EMP of doubly polished grain mounts and of the thin section shown here, respectively.

Figure 3. Rio Puerco and Kilbourne Hole correlations between selected partial melting indices (Bulk Al_2O_3 content and OL Mg#) or of metasomatism (CPX Ce content) for bulk-rock (BR), clinopyroxene (CPX), and olivine (OL). The dashed purple line is the regression using KH Group 2 samples, and the dashed green lines are the regression using KH Group 1 samples. Open circles represent RP clinopyroxene H_2O that were estimated using the average $[H_2O]_{OPX}/[H_2O]_{CPX}$ ratio

in RP peridotites (0.333). Mg# is a.f.u. Mg/ (Mg + Fe). Insets in a and b aim at showing KH pyroxenite compositions.

Figure 4. Clinopyroxene (CPX), orthopyroxene (OPX), and bulk-rock trace element concentrations (Conc.) normalized to primitive mantle (PM) composition (McDonough and Sun, 1995) in Kilbourne Hole (KH, a-c) and Rio Puerco (RP, d-f) peridotites and pyroxenites. Yttrium bulk-rock concentrations were not measured in the KH xenoliths described in Harvey et al. (2012).

Figure 5. Representative transmission FTIR spectra in the OH vibration region (3700 – 2800 cm^{-1}) from (a) clinopyroxenes, (b) orthopyroxenes, and (c) olivines. Symbols α, β, and γ indicate the orientation of the infrared polarizer relative to the crystal indicatrix. All spectra are normalized to a thickness of 1 cm and offset for clarity.

Figure 6. Water contents of clinopyroxene (CPX), orthopyroxene (OPX), olivine (OL) and bulk-rock (BR) compared to selected parameters. Blue lines are regressions through the KH peridotites. Open circles represent samples in which water could not be measured in the clinopyroxene (no clear path for the infrared beam), and instead, clinopyroxene H_2O contents are estimated using the average $[H_2O]_{OPX}/[H_2O]_{CPX}$ ratio in RP peridotites (0.333). Uncertainties of 1σ on water content measurements are shown. Dotted purple ellipse in a marks KIL41 harzburgite and its clinopyroxenite vein. The KH and RP pyroxene water contents are compared to pyroxene water contents from the literature on peridotites (perid.) from mantle xenoliths from cratonic and off-craton settings from the database of Peslier et al. (2017). Grey dotted lines in panel d encompass the $[H_2O]_{CPX}/[H_2O]_{OPX}$ ratios of experiments run at solidus (Aubaud et al., 2004; Hauri et al., 2006; Tenner et al., 2009). The discrepancy between the peridotites $[H_2O]_{CPX}/[H_2O]_{OPX}$ ratios and

1197 those from experiments is caused by sub-solidus equilibration (equil.) of water between the
1198 pyroxenes of the natural peridotites (grey arrow).

1199 **Figure 7.** Total integrated OH absorbances measured from core to core across selected olivine
1200 grains from Kilbourne Hole and Rio Puerco peridotites and H diffusion modelling. The profiles in
1201 b, c, and d are interpreted as H diffusion from the olivine during xenolith ascent. Olivines in 7 out
1202 of 15 KH xenoliths appear to not have lost any H (example shown in a). The spectra shown (KIL71
1203 and KIL43) are representative lherzolites from Kilbourne Hole, while CSR-7 (harzburgite) and
1204 CTON53 (websterite) are the only two samples that have water in their olivine from Rio Puerco.
1205 Solid and dashed lines are modeled H diffusion profiles modelled in one-dimension and the
1206 diffusion rates from Demouchy and Mackwell (2006) calculated at the equilibration temperature
1207 of each peridotite. A in the legend stands for the absorbance used as the initial olivine water content
1208 in the model. Solid lines indicate a model where the initial water content used (A) was the
1209 absorbance measured in the core of the grain (observed A). Dashed lines indicate a model where
1210 the initial water content used (A) was higher than the measured absorbance at the core of the grain.
1211 β and γ indicate the orientation of the infrared polarizer relative to the mineral principle axes. The
1212 time listed for each model is the H diffusion time.

1213 **Figure 8.** Clinopyroxene (CPX) water contents and modal abundances of KH peridotites compared
1214 to clinopyroxene Al_2O_3 and bulk-rock (BR) Yb contents. Bluek lines are linear regressions using
1215 all KH data. Uncertainty of 1σ on water content measurements is shown.

1216 **Figure 9.** Selected major and trace element of Rio Puerco and Kilbourne xenoliths compared to
1217 partial melting models. These models use Yb and Y content variations in clinopyroxene (CPX)
1218 during incremental batch melting of primitive mantle (PM, in red; McDonough and Sun, 1995),

depleted mantle (DM, in pink, Workman and Hart, 2005), and the most fertile KH peridotite, KH72 blue line). Tick marks represent 5% melt intervals. Abyssal peridotites data are from Hellebrand et al. (2002), Johnson et al. (1990), Seyler et al. (2004), and Warren (2016). This figure was used to estimate the degree of melting sustained by each KH and RP peridotite. Symbols as in Fig. 3.

Figure 10. Melting models compared to water contents of KH and RP bulk-rock (BR), clinopyroxene (CPX), orthopyroxene (OPX) and olivine (OL). Solid black lines represent batch melting curves with a c_o of 570 ppm H_2O, and the dotted black lines represent incremental batch melting models with a c_o of 1100 ppm. Gray areas and lines encompass melting models between those using minimum (min) and maximum (max) available water partition coefficients (Table SI7). Pink curves in panel a are for the minimum (200 ppm H_2O) and maximum c_o (1000 ppm H_2O) that result in models that encompass the water content of the minimally metasomatized KH Group 1 peridotites (light blue round symbols). A c_o 570 ppm H_2O (batch melting) or 1000 ppm H_2O (incremental batch melting) allows reasonable modelling of the bulk-rock water content of most KH peridotites (a), but not of the measured water contents in each mineral phase, in particular the water content of clinopyroxene and olivine of KH Group 1 samples (b,c,d). However, if the water contents of minerals are corrected for sub-solidus equilibration (corr.), then the melting curves match reasonably the water contents of individual mineral phases (e,f,g). RP pyroxene water contents are too high compared to the melting models, except for LREE-depleted lherzolites CSC-20 and CSR-16. F is the degree of melting, from 1 to 25 %, calculated from using the Y content of the clinopyroxene with KIL72 as an initial composition (Fig. 9). Uncertainty of 1σ is shown for water contents.

Figure 11. Regressions used to calculate the water contents of peridotite minerals at the solidus. a) $\frac{(Ca/Mg)opx}{(Ca/Mg)cpx}$ ratios versus temperature of equilibration (°C) for KH and RP peridotites data, and three experiments (grey crosses) (Aubaud et al., 2004; Hauri et al., 2006). Regressions through the data allows calculation of the $\frac{(Ca/Mg)opx}{(Ca/Mg)cpx}$ ratio at solidus temperature (1400ºC). b-c) $\frac{[H_2O]_{opx}}{[H_2O]_{cpx}}$ or $\frac{[H_2O]_{ol}}{[H_2O]_{cpx}}$ ratios of KH and RP peridotites and experiments plotted against $\frac{(Ca/Mg)opx}{(Ca/Mg)cpx}$ ratios. This allows to calculate the $\frac{[H_2O]_{opx}}{[H_2O]_{cpx}}$ and $\frac{[H_2O]_{ol}}{[H_2O]_{cpx}}$ at the solidus. Symbols for peridotites as in Fig. 3.

Figure 12. Trace element concentrations (Conc.) of clinopyroxene normalized to primitive mantle (PM) from peridotite-melt interaction models compared to metasomatized KH (i.e. Group 2) and RP peridotites (thick black lines). First, the starting composition of the peridotite is calculated by incremental batch melting models (dashed black line) from the composition of KIL72 and using as minimum the degree of melting inferred for each sample (from Fig. 8c method). Then that residue composition is mixed with a melt which composition results from assimilation and crystallization modelling (AFC). Various melt compositions were tested, from melts in equilibrium with KH pyroxenites (melt eq. KH pyrox., purple line) and RP websterite (melt eq. RP webs., orange line) to melt compositions from the literature (panel a and Table SI9): melt in equilibrium with primitive mantle (PMM; McDonough and Sun, 1995), mid-oceanic ridge basalt (MORB; Klein, 2003), arc basalt (ARC; Plank, 2005), slab silicate melt (SM; Rapp et al., 1999), subduction zone carbonatite (SZC; Walter et al., 2008) and continental carbonatite (CC; Bizimis et al., 2003). For clarity, only the best matches between models and data are shown.

Figure 13. Peridotite-melt interaction (PMI) models for water contents compared to metasomatized KH (Group 2, a-b) and RP (all but CSR-20 and CSR-16, c-d) peridotites. The water

content of a certain percentage of melts issued from assimilation and fractional crystallization (AFC) modelling are mixed with peridotite water contents issued from batch (for KH) and fractional (for RP) melting models as a function of the degree of melting (F). Gray areas encompass melting models between those using maximum and minimum available water partition coefficients (Table SI10). The water content of peridotite minerals has been corrected for sub-solidus equilibration (corr.). CS, CSR, CSC are the different volcanic necks where xenoliths are found at RP. Pyrox. = pyroxenite, webs. = websterite, eq. = equilibrium. Symbols as in Fig. 3.

Figure 14. Effective viscosity of KH peridotites versus their bulk-rock (BR) water contents. Effective viscosity is calculated using the olivine water contents and the equation from Li et al. (2008). Estimates of SW USA asthenosphere (asthen.) viscosity at depths < 100 km are shown in the red field (Dixon et al., 2004; Kaufmann and Amelung, 2000). Global viscosity estimates are shown in the pink field with the average as a dark pink vertical line (Craig and McKenzie, 1986; Hager, 1991; Larsen et al., 2005; Pollitz et al., 1998). Water contents estimates for the upper part of the asthenosphere range from < 20 ppm to >1000 ppm H_2O and could be higher beneath SW USA (Dixon et al., 2004; Dixon and Stolper, 1995; Masuti et al., 2016; Sarafian et al., 2015). Empty blue circles are for viscosities with olivine water contents of KH Group 1 calculated at possible lithosphere-asthenospheric boundary depths beneath KH (bright blue for 62 km and 1250ºC and light blue for 70 km and 1400ºC, i.e. near solidus conditions).

References

Achauer, U. and Masson, F. (2002) Seismic tomography of continental rifts revisited: from relative to absolute heterogeneities. Tectonophys. 358, 17-37.

Adam, J. and Green, T. (2006) Trace element partitioning between mica- and amphibole garnet lherzolite and hydrous basanitic melt: 1 Experimental results and the investigation of controls on partitioning behaviour. Cont. Min. Pet. 152, 1-17.

Armytage, R.M.G., Brandon, A.D., Andreasen, R. and Lapen, T.J. (2015) Evolution of Mojavian mantle lithosphere influenced by Farallon plate subduction: Evidence from Hf and Nd isotopes in peridotite xenoliths from Dish Hill, CA. Geochim. Cosmochim. Acta 159, 264-284.

Armytage, R.M.G., Brandon, A.D., Peslier, A.H. and Lapen, T.J. (2014) Osmium isotope evidence for Early to Middle Proterozoic mantle lithosphere stabilization and concomitant production of juvenile crust in Dish Hill, CA peridotite xenoliths. Geochim. Cosmochim. Acta 137, 113-133.

Asimow, P.D. and Longhi, J. (2004) The significance of multiple saturation points in the context of polybaric near-fractional melting. J. Petrol. 45, 2349-2367.

Aubaud, C., Hauri, E. and Hirschmann, M.M. (2004) Hydrogen partition coefficients between nominally anhydrous minerals and basaltic melts. Geophys. Res. Lett. 31, doi:10.1029/2004GL021341.

1301 Beattie, P. (1994) Systematics and energetics of trace-element partitioning between olivine and
1302 silicate melts: Implications for the nature of mineral/melt partitioning. Chem. Geol. 117, 57-
1303 71.
1304 Bell, D.R., Ihinger, P.D. and Rossman, G.R. (1995) Quantitative analysis of trace OH in garnet and
1305 pyroxenes. Am. Mineral. 80, 465-474.
1306 Bell, D.R. and Rossman, G.R. (1992) Water in Earth's mantle: the role of nominally anhydrous
1307 minerals. Science 255, 1391-1397.
1308 Bell, D.R., Rossman, G.R., Maldener, J., Endisch, D. and Rauch, F. (2003) Hydroxide in olivine: a
1309 quantitative determination of the absolute amount and calibration of the IR spectrum. J.
1310 Geophys. Res. 108 (B2), 2105.
1311 Beran, A. and Libowitzky, E. (2006) Water in natural mantle minerals II: olivine, garnet and
1312 accessory minerals, in: Keppler, H., Smyth, J.R. (Eds.), Water in nominally anhydrous minerals.
1313 Mineralogical Society of America, Chantilly, VA, pp. 169-191.
1314 Bertrand, P. and Mercier, J.-C. (1985) The mutual solubility of coexisting ortho- and
1315 clinopyroxene: toward an absolute geothermometer for the natural system? Earth Planet.
1316 Sci. Lett. 76, 109-122.
1317 Bizimis, M., Salters, V.J.M. and Dawson, J.B. (2003) The brevity of carbonatite sources in the
1318 mantle: evidence from Hf isotopes. Cont. Min. Pet. 145, 281-300.
1319 Bizimis, M., Sen, G. and Salters, V.J.M. (2004) Hf-Nd isotope decoupling in the oceanic
1320 lithosphere: constraints from spinel peridotites from Oahu, Hawaii. Earth Planet. Sci. Lett.
1321 217, 43-58.

1322 Blundy, J.D. and Dalton, J. (2000) Experimental comparison of trace element partitioning
1323 between clinopyroxene and melt in carbonate and silicate systems, and implications for
1324 mantle metasomatism. Cont. Min. Pet. 139, 356-371.
1325 Bonadiman, C., Hao, Y., Coltorti, M., Dallai, L., Faccini, B., Huang, Y. and Xia, Q.-K. (2009) Water
1326 contents of pyroxenes in intraplate lithospheric mantle. Eur J. Mineral. 21, 637-647.
1327 Brenna, M., Cronin, S.J., Smith, I.E.M., Tollan, P.M.E., Scott, J.M., Prior, D.J., Bambery, K. and
1328 Ukstins, I.A. (2018) Olivine xenocryst diffusion reveals rapid monogenetic basaltic magma
1329 ascent following complex storage at Pupuke Maar, Auckland Volcanic Field, New Zealand.
1330 Earth Planet. Sci. Lett. 499, 13-22.
1331 Brey, G.P. and Köhler, T. (1990) Geothermobarometry in four-phase lherzolites II. New
1332 thermobarometers, and practical assessment of existing thermobarometers. J. Petrol. 31,
1333 1353-1378.
1334 Buseck, P.R., Nord, G.L. and Veblen, D.R. (1980) Subsolidus phenomena in pyroxenes, in: Prewit,
1335 C.T. (Ed.), Pyroxenes. Mineralogical Society of America, Blacksburg, VA, pp. 117-212.
1336 Bussod, G.Y. and Irving, A.J. (1981) Thermal and rheologic history of the upper mantle beneath
1337 the southern Rio Grande rift, LPI Contribution. Lunar and Planetary Institute, pp. 145-148.
1338 Bussod, G.Y.A. and Williams, D.R. (1991) Thermal and kinematic model of the southern Rio
1339 Grande rift: inferences from crustal and mantle xenoliths from Kilbourne Hole, New Mexico.
1340 Tectonophys. 197, 373-389.
1341 Byerly, B.L. and Lassiter, J.C. (2012) Evidence from mantle xenoliths for lithosphere removal
1342 beneath the central Rio Grande Rift. Earth Planet. Sci. Lett. 355-356, 82-93.

1343 Carlson, R.W., Pearson, D.G. and James, D.E. (2005) Physical, chemical, and chronological
1344 characteristics of continental mantle. Rev. Geophys. 43, RG1001.
1345 Carter, J.L. (1970) Mineralogy and chemistry of the Earth's upper mantle based on the partial
1346 fusion-partial crystallization model. GSA Bulletin 81 (7), 2021-2034.
1347
1348 Chakraborty, S. (2010) Diffusion coefficients in olivine, wadsleyite and ringwoodite, in: Zhang, Y.,
1349 Cherniak, D.J. (Eds.), Diffusion in minerals and melts. Mineralogical Society of America, pp.
1350 603-639.
1351 Chapin, C. (1979) Evolution of the Rio Grande Rift – A Summary, Rio Grande Rift: Tectonics and
1352 Magmatism. American Geophysical Union, pp. 1-6.
1353 Cherniak, D.J. and Dimanov, A. (2010) Diffusion in pyroxene, mica and amphibole, in: Zhang, Y.,
1354 Cherniak, D.J. (Eds.), Diffusion in minerals and melts. Mineralogical Society of America,
1355 Geochemical Society, Chantilly, VA, pp. 641-690.
1356 Chopra, P.N. and Paterson, M.S. (1984) The role of water in the deformation of dunite. J.
1357 Geophys. Res. 89, 7861-7876.
1358 Cline II, C.J., Faul, U.H., David, E.C., Berry, A.J. and Jackson, I. (2018) Redox-influenced seismic
1359 properties of upper-mantle olivine. Nature 555, 355.
1360 Coney, P.J. and Reynolds, S.J. (1977) Cordilleran Benioff zones. Nature 270, 403.
1361 Copeland, P., Currie, C.A., Lawton, T.F. and Murphy, M.A. (2017) Location, location, location: The
1362 variable lifespan of the Laramide orogeny. Geology 45, 223-226.
1363 Cordell, L., Zorin, Y.A. and Keller, G.R. (1991) The decompensative gravity anomaly and deep
1364 structure of the region of the Rio Grande Rift. J. Geophys. Res. 96, 6557-6568.

1365 Craig, C.H. and McKenzie, D. (1986) The existence of a thin low-viscosity layer beneath the
1366 lithosphere. Earth Planet. Sci. Lett. 78, 420-426.
1367 DeCelles, P.G. (2004) Late Jurassic to Eocene evolution of the Cordilleran thrust belt and foreland
1368 basin system, western U.S.A. Am. J. Sci. 304, 105-168.
1369 Demouchy, S. and Bolfan-Casanova, N. (2016) Distribution and transport of hydrogen in the
1370 lithospheric mantle: a review. Lithos 240-243, 402-425.
1371 Demouchy, S. and Mackwell, S. (2006) Mechanisms of hydrogen incorporation and diffusion in
1372 iron-bearing olivine. Phys. Chem. Min. 33, 347.
1373 Demouchy, S., Shcheka, S., Denis, C.M.M. and Thoraval, C. (2017) Subsolidus hydrogen
1374 partitioning between nominally anhydrous minerals in garnet-bearing peridotite. Am.
1375 Mineral. 102, 1822-1831.
1376 Denis, C.M.M., Alard, O. and Demouchy, S. (2015) Water content and hydrogen behaviour during
1377 metasomatism in the uppermost mantle beneath Ray Pic volcano (Massif Central, France).
1378 Lithos 236-237, 256-274.
1379 Denis, C.M.M., Demouchy, S. and Alard, O. (2018) Heterogeneous hydrogen distribution in
1380 orthopyroxene from veined mantle peridotite (San Carlos, Arizona): Impact of melt-rock
1381 interactions. Lithos 302-303, 298-311.
1382 DePaolo, D.J. (1981) Trace element and isotopic effect of combined wallrock assimilation and
1383 fractional crystallization. Earth Planet. Sci. Lett. 53, 189-202.
1384 Dickinson, W.R. and Snyder, W.S. (1978) Plate tectonics of the Laramide orogeny, in: Matthews,
1385 V. (Ed.), Laramide folding associated with basement block faulting in the western United
1386 States, pp. 355-366.

1387 Dixon, J.E. and Clague, D.A. (2001) Volatiles in basaltic glasses from Loihi seamount, Hawaii:
1388 evidence for a relatively dry plume component. J. Petrol. 42, 627-634.
1389 Dixon, J.E., Clague, D.A., Wallace, P. and Poreda, R.J. (1997) Volatiles in alkalic basalts from the
1390 North Arch volcanic field, Hawaii: extensive degassing of deep submarine-erupted alkalic
1391 series lavas. J. Petrol. 38, 911-939.
1392 Dixon, J.E., Dixon, T.H., Bell, D.R. and Malservisi, R. (2004) Lateral variation in upper mantle
1393 viscosity: role of water. Earth Planet. Sci. Lett. 222, 451-467.
1394 Dixon, J.E. and Stolper, E.M. (1995) An experimental study of water and carbon dioxide
1395 solubilities in mid-ocean ridge basaltic liquids. Part II: application to degassing. J. Petrol. 36,
1396 1633-1646.
1397 Doucet, L.S., Peslier, A.H., Ionov, D.A., Brandon, A.D., Golovin, A.V., Goncharov, A.G. and
1398 Ashchepkov, I.V. (2014) High water contents in the Siberian cratonic mantle linked to
1399 metasomatism: an FTIR study of Udachnaya peridotite xenoliths. Geochim. Cosmochim. Acta
1400 137, 159-187.
1401 Downes, H. (2007) Origin and significance of spinel and garnet pyroxenites in the shallow
1402 lithospheric mantle: Ultramafic massifs in orogenic belts in Western Europe and NW Africa.
1403 Lithos 99, 1-24.
1404 Dromgoole, E.L. and Pasteris, J.D. (1987) Interpretation of the sulfide assemblages in a suite of
1405 xenoliths from Kilbourne Hole, New Mexico. Geol. Soc. Am. Spec. Paper 215, 25-46.
1406 Drury, M.R. (1991) Hydration-induced climb dissociation of dislocations in naturally deformed
1407 mantle olivine. Phys. Chem. Min. 18, 106-116.

1408 Ducea, M., Saleeby, J., Morrison, J. and Valencia, V.A. (2005) Subducted carbonates,
1409 metasomatism of mantle wedges, and possible connections to diamond formation: An
1410 example from California. Am. Mineral. 90, 864-870.
1411 Eaton, G.P. (1982) The Basin and Range Province: Origin and Tectonic Significance. Annual Review
1412 of Earth Planet. Sci. 10, 409-440.
1413 Eggins, S.M., Rudnick, R.L. and McDonough, W.F. (1998) The composition of peridotites and their
1414 minerals: a laser-ablation ICP-MS study. Earth Planet. Sci. Lett. 154, 53-71.
1415 Elkins, L.J., Gaetani, G.A. and Sims, K.W.W. (2008) Partitioning of U and Th during garnet
1416 pyroxenite partial melting: Constraints on the source of alkaline ocean island basalts. Earth
1417 Planet. Sci. Lett. 265, 270-286.
1418 English, J.M., Johnston, S.T. and Wang, K. (2003) Thermal modelling of the Laramide orogeny:
1419 testing the flat-slab subduction hypothesis. Earth Planet. Sci. Lett. 214, 619-632.
1420 Faul, U.H., Cline II, C.J., David, E.C., Berry, A.J. and Jackson, I. (2016) Titanium-hydroxyl defect-
1421 controlled rheology of the Earth's upper mantle. Earth Planet. Sci. Lett. 452, 227-237.
1422 Farver, J.R. (2010) Oxygen and hydrogen diffusion in minerals, in: Zhang, Y., Cherniak, D.J. (Eds.),
1423 Diffusion in minerals and melts. Mineralogical Society of America, Geochemical Society,
1424 Chantilly, VA, pp. 447-507.
1425 Frey, F.A. and Prinz, M. (1978) Ultramafic inclusions from San Carlos, Arizona: petrologic and
1426 geochemical data bearing on their petrogenesis. Earth Planet. Sci. Lett. 38, 129-176.
1427 Fujimaki, H., Tatsumoto, M. and Aoki, K. (1984) Partition coefficients of Hf, Zr, and ree between
1428 phenocrysts and groundmasses, Lunar Planet. Sci. Conf., J. Geophys. Res., Houston, TX, pp.
1429 B662-B672.

1430 Gaetani, G.A. and Grove, T.L. (1998) The influence of water on melting of mantle peridotite. Cont.
1431 Min. Pet. 131, 323-346.
1432 Gaetani, G.A., Kent, A.J.R., Grove, T.L., Hutcheon, I.D. and Stolper, E.M. (2003) Mineral/melt
1433 partitioning of trace elements during hydrous peridotite partial melting. Cont. Min. Pet. 145,
1434 391-405.
1435 Gao, S., Liu, X.-W., Yuan, H., Hattendorf, B., Günther, D., Chen, L. and Hu, S. (2002) Determination
1436 of Forty Two Major and Trace Elements in USGS and NIST SRM Glasses by Laser Ablation-
1437 Inductively Coupled Plasma-Mass Spectrometry. Geostand. News. 26, 181-196.
1438 Gao, W., Grand, S.P., Baldridge, W.S., Wilson, D., West, M., Ni, J.F. and Aster, R. (2004) Upper
1439 mantle convection beneath the central Rio Grande rift imaged by P and S wave tomography.
1440 J. Geophys. Res. 109.
1441 Gay, P. and LeMaître, R.W. (1961) Some observation on "iddingsite". Am. Mineral. 46, 92-111.
1442 Green, D.H. (1973) Experimental melting studies on a model upper mantle composition at high
1443 pressure under H_2O-saturated and H_2O undersaturated conditions. Earth Planet. Sci. Lett. 19,
1444 37-45.
1445 Green, T.H., Adam, J. and Siel, S.H. (1992) Trace element partitioning between silicate minerals
1446 and carbonatite at 25 kbar and application to mantle metasomatism. Mineralogy and
1447 Petrology 46, 179-184.
1448 Green, T.H., Blundy, J.D., Adams, J. and Yaxley, G.M. (2000) SIMS determination of trace element
1449 partition coefficients between garnet, clinopyroxene and hydrous basaltic liquids at 2-7.5 GPa
1450 and 1080-1200ºC. Lithos 53, 165-187.

1451 Hager, B.H. (1991) Mantle viscosity - A comparison of models from postglacial rebound and from
1452 the geoid, plate driving forces, and advected heat flux, in: Sabadini, R., Lambeck, K., Boschi,
1453 E. (Eds.), Glacial isostasy, sea level and mantle rheology. Kluwer Academic, Dordrecht,
1454 Netherlands, p. 21.
1455 Hallet, R.B. (1994) Volcanic geology, paleomagnetism, geochronology and geochemistry of the
1456 Rio Puerco Necks, west-central New Mexico. New Mexico Institute of Mining and Technology.
1457 Hallet, R.B., Kyle, P.R. and McIntosh, W.C. (1997) Paleomagnetic and 40Ar/39Ar age constraints
1458 on the chronologic evolution of the Rio Puerco volcanic necks and Mesa Prieta, west-central
1459 New Mexico: Implications for transition zone magmatism. GSA Bulletin 109, 95-106.
1460 Hao, Y., Xia, Q.-K., Li, Q., Chen, H. and Feng, M. (2014) Partial melting control of water contents
1461 in the Cenozoic lithospheric mantle of the Cathaysia block of South China. Chem. Geol. 380,
1462 7-19.
1463 Hansen, L.N. and Warren, J.M. (2015) Quantifying the effect of pyroxene on deformation of
1464 peridotite in a natural shear zone. J. Geophys. Res. 120, 2717-2738.
1465 Harvey, J., Dale, C.W., Gannoun, A. and Burton, K.W. (2011) Osmium mass balance in peridotite
1466 and the effects of mantle-derived sulphides on basalt petrogenesis. Geochim. Cosmochim.
1467 Acta 75, 5574-5596.
1468 Harvey, J., König, S. and Luguet, A. (2015) The effects of melt depletion and metasomatism on
1469 highly siderophile and strongly chalcophile elements: S–Se–Te–Re–PGE systematics of
1470 peridotite xenoliths from Kilbourne Hole, New Mexico. Geochim. Cosmochim. Acta 166, 210-
1471 233.

1472 Harvey, J., Yoshikawa, M., Hammond, S.J. and Burton, K.W. (2012) Deciphering the Trace Element
1473 Characteristics in Kilbourne Hole Peridotite Xenoliths: Melt–Rock Interaction and
1474 Metasomatism beneath the Rio Grande Rift, SW USA. J. Petrol. 53, 1709-1742.
1475 Hauri, E.H., Gaetani, G.A. and Green, T.H. (2006) Partitioning of water during melting of the
1476 Earth's upper mantle at H_2O-undersaturated conditions. Earth Planet. Sci. Lett. 248, 715-734.
1477 Hellebrand, E., Snow, J.E., Dick, H.J.B. and Hofmann, A.W. (2001) Coupled major and trace
1478 elements as indicators of the extent of melting in mid-ocean-ridge peridotites. Nature 410,
1479 677-681.
1480 Hellebrand, E., Snow, J.E., Hoppe, P. and Hofmann, A.W. (2002) Garnet-field melting and late-
1481 stage refertilization in 'residual' abyssal peridotites from the Central Indian Ridge. J. Petrol.
1482 43, 2305-2338.
1483 Herzberg, C. (2004) Geodynamic information in peridotite petrology. J. Petrol. 45, 2507-2530.
1484 Hirschmann, M.M. (2006) Water, melting, and the deep Earth H_2O cycle. Ann. Rev. Earth Planet.
1485 Sci. 34, 629-653.
1486 Hirth, G., Evans, R.L. and Chave, A.D. (2000) Comparison of continental and oceanic mantle
1487 electrical conductivity: Is the Archean lithosphere dry? Geochem. Geophys. Geosys. 1,
1488 2000GC000048.
1489 Hoffer, J.M. (1976) The Potrillo basalt field, south-central New Mexico, Cenozoic Volcanism in
1490 Southwestern New Mexico, pp. 89-92.
1491 Hofmeister, A.M. (2004) Enhancement of radiative transfer in the upper mantle by OH- in
1492 minerals. Phys. Earth Planet. Int. 146, 483-495.

1493 Humphreys, E.D. (1995) Post-Laramide removal of the Farallon slab, western United States.
1494 Geology 23, 987-990.
1495 Humphreys, E.D., Hessler, E., Dueker, K.G., Farmer, G.L., Erslev, E.A. and Atwater, T.A. (2003) How
1496 Laramide-age hydration of North American lithosphere by the Farallon slab controlled
1497 subsequent activity in the western United States. Inter. Geol. Rev. 45, 575-595.
1498 Ingrin, J. and Blanchard, M. (2006) Diffusion of hydrogen in minerals, in: Keppler, H., Smyth, J.R.
1499 (Eds.), Water in nominally anhydrous minerals. Mineralogical Society of America, Chantilly,
1500 VA, pp. 291-320.
1501 Irving, A.J. (1980) Petrology and geochemistry of composite ultramafic xenoliths in alkalic basalts
1502 and implications for magmatic processes within the mantle. Am. J. Sci. 280-A, 389-426.
1503 Johnson, D.M., Hooper, P.R. and Conrey, R.M. (1999) XRF Analysis of Rocks and Minerals for
1504 Major and Trace Elements on a Single Low
1505 Dilution Li-tetraborate Fused Bead. Adv. X-ray Anal. 41, 843-867.
1506 Johnson, K.T.M., Dick, H.J.B. and Shimizu, N. (1990) Melting in the oceanic upper mantle: an ion
1507 probe study of diopsides in abyssal peridotites. J. Geophys. Res. 95, 2661-2678.
1508 Johnston, A.D. and Schwab, B.E. (2004) Constraints on clinopyroxene/melt partitioning of REE,
1509 Rb, Sr, Ti, Cr, Zr, and Nb during mantle melting: First insights from direct peridotite melting
1510 experiments at 1.0 GPa. Geochim. Cosmochim. Acta 68, 4949-4962.
1511 Jones, A.G. (2016) Proton conduction and hydrogen diffusion in olivine: an attempt to reconcile
1512 laboratory and field observations and implications for the role of grain boundary diffusion in
1513 enhancing conductivity. Phys. Chem. Min. 43, 237-265.

1514 Karato, S. (1990) The role of hydrogen in the electrical conductivity of the upper mantle. Nature
1515 347, 272-273.
1516 Karato, S. (2006) Influence of hydrogen-related defects on the electrical conductivity and plastic
1517 deformation of mantle minerals: a critical review, in: Jacobsen, S.D., van der Lee, S. (Eds.),
1518 Earth's deep water cycle. American Geophysical Union, Washington, DC, pp. 113-130.
1519 Karato, S. and Jung, H. (1998) Water, partial melting and the origin of the seismic low velocity
1520 and high attenuation zone in the upper mantle. Earth Planet. Sci. Lett. 157, 193-207.
1521 Karlstrom, K.E., Bowring, S.A., Chamberlain, K.R., Dueker, K.G., Eshete, T., Erslev, E.A., Farmer,
1522 G.L., Heizler, M., Humphreys, E.D., Johnson, R.A., Keller, G.R., Kelley, S.A., Levander, A.,
1523 Magnani, M.B., Matzel, J.P., McCoy, A.M., Miller, K.C., Morozova, E.A., Pazzaglia, F.J., Prodehl,
1524 C., Rumpel, H.M., Shaw, C.A., Sheehan, A.F., Shoshitaishvili, E., Smithson, S.B., Snelson, C.M.,
1525 Stevens, L.M., Tyson, A.R. and Williams, M.L. (2002) Structure and evolution of the
1526 lithosphere beneath the Rocky Mountains; initial results from the CD-ROM experiment. GSA
1527 Today 12, 4-10.
1528 Karlstrom, K.E., Whitmeyer, S.J., Dueker, K., Williams, M.L., Bowring, S.A., Levander, A.R.,
1529 Humphreys, E.D., Keller, G.R. and Group, C.R.W. (2005) Synthesis of Results from the Cd-Rom
1530 Experiment: 4-D Image of the Lithosphere Beneath the Rocky Mountains and Implications for
1531 Understanding the Evolution of Continental Lithosphere, The Rocky Mountain Region: An
1532 Evolving Lithosphere.
1533 Kaufmann, G. and Amelung, F. (2000) Reservoir-induced deformation and continental rheology
1534 in vicinity of Lake Mead, Nevada. J. Geophys. Res. 105, 16341-16358.

1535 Kelemen, P.B., Shimizu, N. and Salters, V.J.M. (1995) Extraction of mid-ocean-ridge basalt from
1536 the upwelling mantle by focused flow of melt in dunite channels. Nature 375, 747-753.
1537 Kempenaers, L., Janssens, K., Jochum, K.P., Vincze, L., Vekemans, B., Somogyi, A., Drakopoulos,
1538 M. and Adams, F. (2003) Micro-heterogeneity study of trace elements in USGS, MPI-DING and
1539 NIST glass reference materials by means of synchrotron micro-XRF. J. Anal. At. Spectrom. 18,
1540 350-357.
1541 Kessel, R., Schmidt, M.W., Ulmer, P. and Pettke, T. (2005) Trace element signature of subduction-
1542 zone fluids, melts and supercritical liquids at 120-180 km depth. Nature 437, 724-727.
1543 Kil, Y. and Wendlandt, R.F. (2004) Pressure and temperature evolution of upper mantle under
1544 the Rio Grande Rift. Cont. Min. Pet. 148, 265-280.
1545 Klein, E.M. (2003) Geochemistry of the Igneous Oceanic Crust in: Holland, H.D., Turekian, K.K.
1546 (Eds.), Treatise on Geochemistry. Pergamon, Oxford, pp. 433-463.
1547 Klemme, S., van der Laan, S.R., FOley, S.F. and Gunther, D. (1995) Experimentally determined
1548 trace and minor element partitioning between clinopyroxene and carbonatite melt under
1549 upper mantle conditions. Earth Planet. Sci. Lett. 133, 439-448.
1550 Langmuir, C.H., Klein, E.M. and Plank, T. (1993) Petrological systematics of mid-ocean ridge
1551 basalts: Constraints on melt generation beneath ocean ridges. Mantle flow and melt
1552 generation at mid-ocean ridges, 183-280.
1553 Larsen, C.F., Motyka, R.J., Freymueller, J.T., Echelmeyer, K.A. and Ivins, E.R. (2005) Rapid
1554 viscoelastic uplift in southeast Alaska caused by post-Little Ice Age glacial retreat. Earth
1555 Planet. Sci. Lett. 237, 548-560.

1556 Li, Z.-X.A., Lee, C.-T., Peslier, A.H., Lenardic, A. and Mackwell, S.J. (2008) Water contents in mantle
1557 xenoliths from the Colorado Plateau and vicinity: implications for the mantle rheology and
1558 hydration-induced thinning of continental lithosphere. J. Geophys. Res. 113, 1-22.
1559 Libowitzky, E. and Beran, A. (2006) The structure of hydrous species in nominally anhydrous
1560 minerals: Information from polarized IR spectroscopy, in: Keppler, H., Smyth, J.R. (Eds.),
1561 Water in nominally anhydrous minerals. Mineralogical Society of America, Chantilly, VA, pp.
1562 29-52.
1563 Lorenz, V. (1975) Formation of phreatomagmatic maar-diatreme volcanoes and its relevance to
1564 kimberlite diatremes. Phys. Chem. Earth 9, 17-29.
1565 Lorenz, V. (2003) Maar-diatreme volcanoes, their formation, and their setting in hard-rock or
1566 soft-rock environments. GeoLines 15, 72-83.
1567 Mackwell, S.J., Kohlstedt, D.L. and Paterson, M.S. (1985) The role of water in the deformation of
1568 olivine single crystals. J. Geophys. Res. 90, 11319-11333.
1569 Magnani, M.B., Levander, A., Miller, K.C., Eshete, T. and Karlstrom, K.E. (2005) Seismic
1570 Investigation of the Yavapai-Mazatzal Transition Zone and the Jemez Lineament in
1571 Northeastern New Mexico, The Rocky Mountain Region: An Evolving Lithosphere. American
1572 Geophysical Union, pp. 227-238.
1573 Magnani, M.B., Miller, K.C., Levander, A. and Karlstrom, K.E. (2004) The Yavapai-Mazatzal
1574 boundary: A long-lived tectonic element in the lithosphere of southwestern North America.
1575 GSA Bulletin 116, 1137-1142.

1576 Masuti, S., Barbot, S.D., Karato, S.-I., Feng, L. and Banerjee, P. (2016) Upper-mantle water
1577 stratification inferred from observations of the 2012 Indian Ocean earthquake. Nature 538,
1578 373-377.
1579 McDonough, W.F. and Sun, S.-S. (1995) The composition of the Earth. Chem. Geol. 120, 223-253.
1580 McKenzie, D. and O'Nions, R.K. (1991) Partial melt distributions from inversion of rare Earth
1581 element concentrations. J. Petrol. 32, 1021-1091.
1582 Mei, S. and Kohlstedt, D.L. (2000a) Influence of water on plastic deformation of olivine aggregates
1583 1. Diffusion creep regime. J. Geophys. Res. 105, 21457-21469.
1584 Mei, S. and Kohlstedt, D.L. (2000b) Influence of water on plastic deformation of olivine aggregates
1585 2. Dislocation creep regime. J. Geophys. Res. 105, 21471-21481.
1586 Menzies, M. (1983) Mantle Ultramafic Xenoliths in Alkaline Magmas: Evidence for Mantle
1587 Heterogeneity Modified by Magmatic Activity, in: Hawkesworth, C.J., Norry, M.J. (Eds.),
1588 Continental Basalts and Mantle Xenoliths. Shiva Publishing Limited, Cambridge, p. 272.
1589 Mercier, J.-C. and Nicolas, A. (1975) Textures and fabrics of upper-mantle peridotites as
1590 illustrated by xenoliths from basalts. J. Petrol. 16, 454-487.
1591 Michael, P.J. (1988) The concentration, behavior and storage of H_2O in the suboceanic upper
1592 mantle: Implications for mantle metasomatism. Geochim. Cosmochim. Acta 52, 555-566.
1593 Nielsen, R.L., Gallahan, W.E. and Newberger, F. (1992) Experimentally determined mineral-melt
1594 partition coefficients for Sc, Y and REE for olivine, orthopyroxene, pigeonite, magnetite and
1595 ilmenite. Cont. Min. Pet. 110, 488-499.

1596 Norman, M.D. (1998) Melting and metasomatism in the continental lithosphere: laser ablation
1597 ICPMS analysis of minerals in spinel lherzolites from eastern Australia. Cont. Min. Pet. 130,
1598 240-255.
1599 Norman, M.D., Griffin, W.L., Pearson, N.J., Garcia, M.O. and O'reilly, S.Y. (1998) Quantitative
1600 analysis of trace element abundances in glasses and minerals: a comparison of laser ablation
1601 inductively coupled plasma mass spectrometry, solution inductively coupled plasma mass
1602 spectrometry, proton microprobe and electron microprobe data. J. Anal. At. Spectrom. 13,
1603 477-482.
1604 O'Leary, J.A., Gaetani, G.A. and Hauri, E.H. (2010) The effect of tetrahedral Al^{3+} on the partitioning
1605 of water between clinopyroxene and silicate melt. Earth Planet. Sci. Lett. 297, 111-120.
1606 Palme, H. and O'Neill, H.S.C. (2003) Cosmochemical estimates of mantle composition, in: Carlson,
1607 R.W. (Ed.), Treatise on geochemistry. Elsevier, pp. 1-38.
1608 Peacock, S.M. (1990) Fluid processes in subduction zones. Science 248, 329-337.
1609 Pearson, D.G., Canil, D. and Shirey, S. (2003) Mantle samples included in volcanic rocks: xenoliths
1610 and diamonds, in: Holland, H.D., Turekian, K.K. (Eds.), Treatise of Geochemistry. Elsevier,
1611 Oxford, pp. 171-275.
1612 Padrón-Navarta, J.A. and Hermann, J. (2017) A subsolidus olivine water solubility equation for
1613 the Earth's upper mantle. J. Geophys. Res. 122, 9862-9880.
1614 Perkins, D. and Anthony, E.Y. (2011) The evolution of spinel lherzolite xenoliths and the nature of
1615 the mantle at Kilbourne Hole, New Mexico. Cont. Min. Pet. 162, 1139-1157.

1616 Perkins, G.B., Sharp, Z.D. and Selverstone, J. (2006) Oxygen isotope evidence for subduction and
1617 rift-related mantle metasomatism beneath the Colorado Plateau–Rio Grande rift transition.
1618 Cont. Min. Pet. 151, 633.
1619 Perry, F.V., Baldridge, W.S. and DePaolo, D.J. (1988) Chemical and isotopic evidence for
1620 lithospheric thinning beneath the Rio Grande Rift. Nature 332, 432-434.
1621 Peslier, A.H. (2010) A review of water contents of nominally anhydrous natural minerals in the
1622 mantles of Earth, Mars and the Moon. J. Volc. Geotherm. Res. 197, 239-258.
1623 Peslier, A.H. and Bizimis, M. (2015) Water in Hawaiian peridotite minerals: A case for a dry
1624 metasomatized oceanic mantle lithosphere. Geochem. Geophys. Geosys. 16, 1-22.
1625 Peslier, A.H., Bizimis, M. and Matney, M. (2015) Water disequilibrium in olivines from Hawaiian
1626 peridotites: recent metasomatism, H diffusion and magma ascent rates. Geochim.
1627 Cosmochim. Acta 154, 98-117.
1628 Peslier, A.H. and Luhr, J.F. (2006) Hydrogen loss from olivines in mantle xenoliths from Simcoe
1629 (USA) and Mexico: Mafic alkalic magma ascent rates and water budget of the sub-continental
1630 lithosphere. Earth Planet. Sci. Lett. 242, 302-319.
1631 Peslier, A.H., Luhr, J.F. and Post, J. (2002) Low water contents in pyroxenes from spinel-
1632 peridotites of the oxidized, sub-arc mantle wedge. Earth Planet. Sci. Lett. 201, 69-86.
1633 Peslier, A.H., Schönbächler, M. and Busemann, H. (2017) Water in the Earth's interior:
1634 Distribution and origin. Space Sci. Rev. 212, 743-811.
1635 Peslier, A.H., Woodland, A.B., Bell, D.R. and Lazarov, M. (2010) Olivine water contents in the
1636 continental lithosphere and the longevity of cratons. Nature 467, 78-81.

1637 Peslier, A.H., Woodland, A.B., Bell, D.R., Lazarov, M. and Lapen, T.J. (2012) Metasomatic control
1638 of water contents in the Kaapvaal cratonic mantle. Geochim. Cosmochim. Acta 97, 213-246.
1639 Peslier, A.H., Woodland, A.B. and Wolff, J.A. (2008) Fast kimberlite ascent rates estimated from
1640 hydrogen diffusion profiles in xenolithic olivines from Southern Africa. Geochim. Cosmochim.
1641 Acta 72, 2711-2722.
1642 Plank, T. (2005) Constraints from thorium/lanthanum on sediment recycling at subduction zones
1643 and the evolution of the continents. J. Petrol. 46, 921-944.
1644 Plank, T., Kelley, K.A., Zimmer, M.M., Hauri, E.H. and Wallace, P.J. (2013) Why do mafic magmas
1645 contain ~4 wt% water on average? Earth Planet. Sci. Lett. 364, 168-179.
1646 Pollitz, F.F., Bürgmann, R. and Romanowicz, B. (1998) Viscosity of oceanic asthenosphere inferred
1647 from remote triggering of earthquakes. Science 280, 1245-1249.
1648 Porreca, C., Selverstone, J. and Samuels, K. (2006) Pyroxenite xenoliths from the Rio Puerco
1649 volcanic field, New Mexico: Melt metasomatism at the margin of the Rio Grande rift.
1650 Geosphere 2, 333-351.
1651 Rapp, R.P., Shimizu, N., Norman, M.D. and Applegate, G.S. (1999) Reaction between slab-derived
1652 melts and peridotite in the mantle wedge: experimental constraints at 3.8 GPa. Chem. Geol.
1653 160, 335-356.
1654 Reeves, G.C. and DeHon, R.A. (1965) Geology of Potrillo maar, New Mexico and northern
1655 Chihuahua, Mexico. Am. J. Sci. 263, 401-409.
1656 Roden, M.F., Irving, A.J. and Murthy, V.R. (1988) Isotopic and trace element composition of the
1657 upper mantle beneath a young continental rift: results from Kilbourne Hole, New Mexico.
1658 Geochim. Cosmochim. Acta 52, 461-473.

1659 Rowe, M.C., Lassiter, J.C. and Goff, K. (2015) Basalt volatile fluctuations during continental rifting:
1660 An example from the Rio Grande Rift, USA. Geochem. Geophys. Geosys. 16, 1254-1273.
1661 Saleeby, J. (2003) Segmentation of the Laramide Slab—evidence from the southern Sierra Nevada
1662 region. GSA Bulletin 115, 655-668.
1663 Salters, V., Longhi, J.E. and Bizimis, M. (2002) Near mantle solidus trace element partitioning at
1664 pressures up to 3.4 GPa. Geochem. Geophys. Geosys. 3, 1-23.
1665 Salters, V.J.M. and Longhi, J. (1999) Trace element partitioning during the initial stages of melting
1666 beneath mid-ocean ridges. Earth Planet. Sci. Lett. 166, 15-30.
1667 Sarafian, E., Evans, R.L., Collins, J.A., Elsenbeck, J., Gaetani, G.A., Gaherty, J.B., Hirth, G. and
1668 Lizarralde, D. (2015) The electrical structure of the central Pacific upper mantle constrained
1669 by the NoMelt experiment. Geochem. Geophys. Geosys. 16, 1115-1132.
1670 Schmidt, M.W. and Poli, S. (1998) Experimentally based water budgets for dehydrating slabs and
1671 consequences for arc magma generation. Earth Planet. Sci. Lett. 163, 361-379.
1672 Seyler, M., Lorand, J.P., Toplis, M.J. and Godard, G. (2004) Asthenospheric metasomatism
1673 beneath the mid-ocean ridge: evidence from depleted abyssal peridotites. Geology 32, 301-
1674 304.
1675 Shaw, D.M. (2005) Trace elements in magmas: a theoretical treatment. Cambridge University
1676 Press.
1677 Skogby, H. (2006) Water in natural mantle minerals I: pyroxenes, in: Keppler, H., Smyth, J.R. (Eds.),
1678 Water in nominally anhydrous minerals. Mineralogical Society of America, Chantilly, VA, pp.
1679 155-167.

1680 Skogby, H., Bell, D.R. and Rossman, G.R. (1990) Hydroxide in pyroxene: variations in the natural
1681 environment. Am. Mineral. 75, 764-774.
1682 Smith, D. (2000) Insights into the evolution of the uppermost continental mantle from xenolith
1683 localities on and near the Colorado Plateau and regional comparisons. J. Geophys. Res. 2000,
1684 16769-16781.
1685 Sosa, A., Thompson, L., Velasco, A.A., Romero, R. and Herrmann, R.B. (2014) 3-D structure of the
1686 Rio Grande Rift from 1-D constrained joint inversion of receiver functions and surface wave
1687 dispersion. Earth Planet. Sci. Lett. 402, 127-137.
1688 Stinnett, J.W. and Stueber, A.M. (1976) A strontium isotopic and geochemical study of volcanic
1689 rocks from the Datil-Mogollon field, southwestern New Mexico, Geological Society of
1690 America Abstracts Program, pp. 636-637.
1691 Sun, C. and Liang, Y. (2014) An assessment of subsolidus re-equilibration on REE distribution
1692 among mantle minerals olivine, orthopyroxene, clinopyroxene, and garnet in peridotites.
1693 Chem. Geol. 372, 80-91.
1694 Sundvall, R. and Stalder, R. (2011) Water in upper mantle pyroxene megacrysts and xenocrysts:
1695 a survey study. Am. Mineral. 96, 1215-1227.
1696 Sweeney, R.J., Prozesky, V. and Przybylowicz, W. (1995) Selected trace and minor element
1697 partitioning between peridotite minerals and carbonatite melts at 18–46 kb pressure.
1698 Geochim. Cosmochim. Acta 59, 3671-3683.
1699 Tarantola, A. and Valette, B. (1982) Generalized nonlinear inverse problems solved using the least
1700 squares criterion. Rev. Geophys. 20, 219-232.

1701 Tenner, T.J., Hirschmann, M.M., Withers, A.C. and Hervig, R.L. (2009) Hydrogen partitioning
1702 between nominally anhydrous upper mantle minerals and melt between 3 and 5 GPa and
1703 applications to hydrous peridotite partial melting. Chem. Geol. 262, 42-56.
1704 Thompson, R.N., Ottley, C.J., Smith, P.M., Pearson, D.G., Dickin, A.P., Morrison, M.A., Leat, P.T.
1705 and Gibson, S.A. (2005) Source of the Quaternary Alkalic Basalts, Picrites and Basanites of the
1706 Potrillo Volcanic Field, New Mexico, USA: Lithosphere or Convecting Mantle? J. Petrol. 46,
1707 1603-1643.
1708 Thoraval, C. and Demouchy, S. (2014) Numerical models of ionic diffusion in one and three
1709 dimensions: application to dehydration of mantle olivine. Phys. Chem. Min. 41, 709-723.
1710 Tian, Z.Z., Liu, J., Xia, Q.-K., Ingrin, J., Hao, Y.T. and Christophe, D. (2017) Water concentration
1711 profiles in natural mantle orthopyroxenes: A geochronometer for long annealing of xenoliths
1712 within magma. Geology 45, 87-90.
1713 van der Lee, S., Regenauer-Lieb, K. and Yuen, D.A. (2008) The role of water in connecting past
1714 and future episodes of subduction. Earth Planet. Sci. Lett. 273, 15-27.
1715 van Wijk, J., van Hunen, J. and Goes, S. (2008) Small-scale convection during continental rifting:
1716 Evidence from the Rio Grande rift. Geology 36, 575-578.
1717 Walter, M.J., Bulanova, G.P., Armstrong, L.S., Keshav, S., Blundy, J.D., Gudfinnsson, G., Lord, O.T.,
1718 Lennie, A.R., Clark, S.M., Smith, C.B. and Gobbo, L. (2008) Primary carbonatite melt from
1719 deeply subducted oceanic crust. Nature 454, 622-625.
1720 Walter, M.J., Sisson, T.W. and Presnall, D.C. (1995) A mass proportion method for calculating
1721 melting reactions and application to melting of model upper mantle lherzolite. Earth Planet.
1722 Sci. Lett. 135, 77-90.

Wang, D., Li, H., Yi, L. and Shi, B. (2008) The electrical conductivity of upper-mantle rocks: water content in the upper mantle. Phys. Chem. Min. 35, 157-162.

Warren, J.M. and Hauri, E.H. (2014) Pyroxenes as tracers of mantle water variations. J. Geophys. Res. 119, 1851-1881.

Warren, J.M. (2016) Global variations in abyssal peridotite compositions. Lithos 248-251, 193-219.

West, M., Ni, J., Baldridge, W.S., Wilson, D., Aster, R., Gao, W. and Grand, S. (2004) Crust and upper mantle shear wave structure of the southwest United States: implications for rifting and support for high elevation. J. Geophys. Res. 109, doi:10.1029/2003JB002575.

Whitmeyer, S.J. and Karlstrom, K.E. (2007) Tectonic model for the Proterozoic growth of North America. Geosphere 3, 220-259.

Workman, R.K. and Hart, S.H. (2005) Major and trace element composition of the depleted MORB mantle (DMM). Earth Planet. Sci. Lett. 231, 53-72.

Yu, Y., Xu, X.-S., Griffin, W.L., O'Reilly, S.Y. and Xia, Q.-K. (2011) H_2O contents and their modification in the cenozoic subcontinental lithospheric mantle beneath the Cathaysia block, SE China. Lithos 126, 182-197.

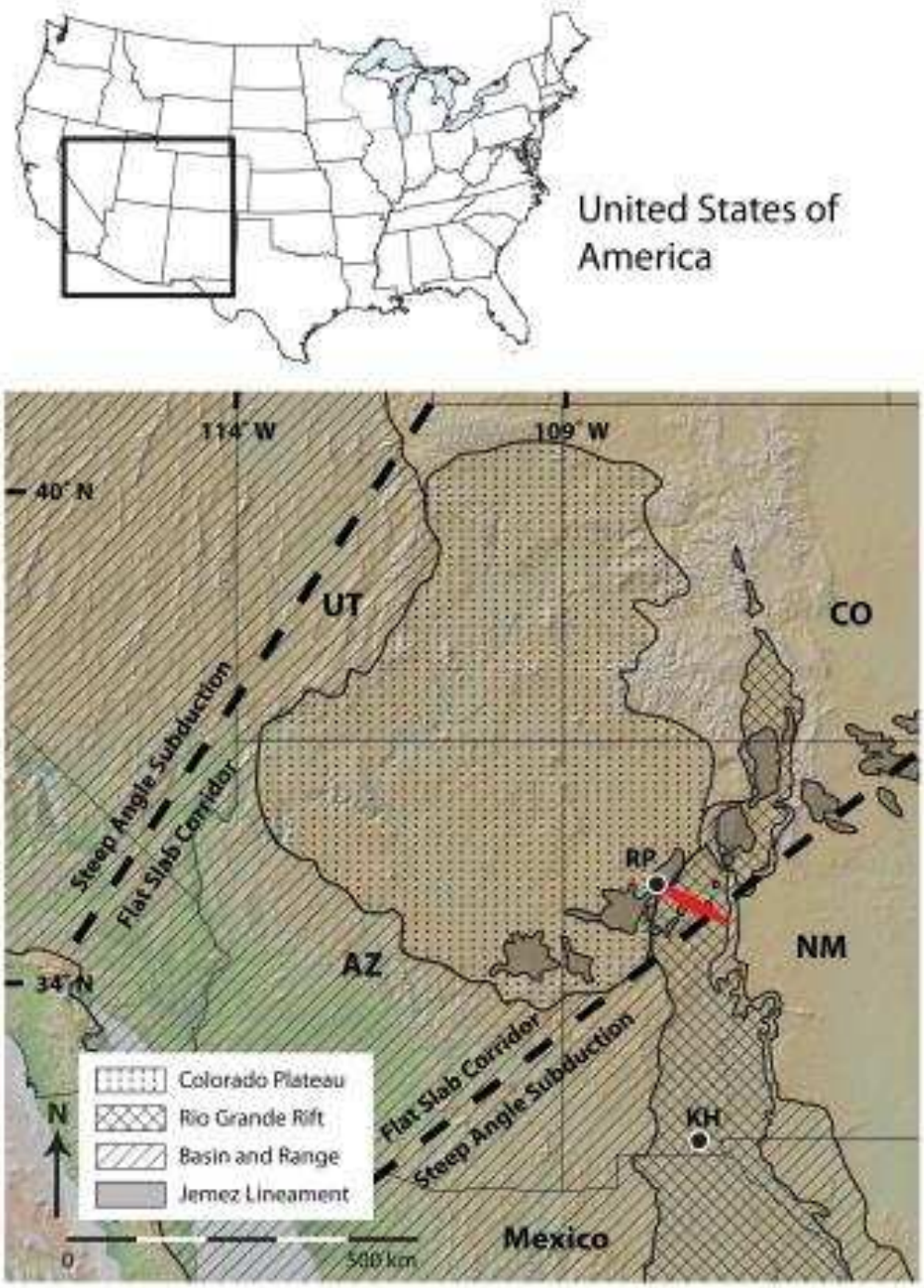

Figure 1.

1744

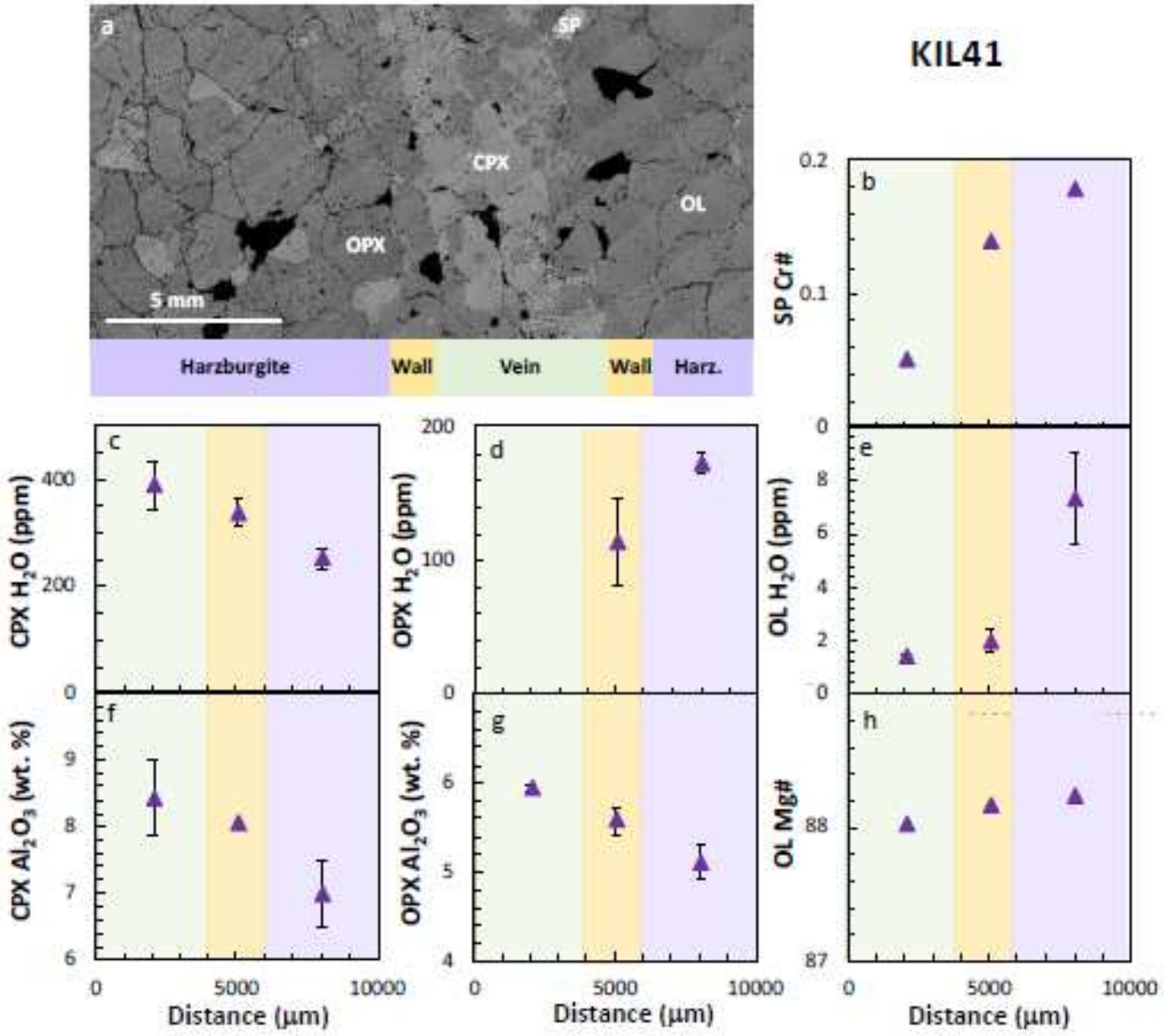
KIL41
a
SP
CPX
OL
OPX
5 mm
Harzburgite
Wall
Vein
Wall
Harz.
b
SP Cr#
c
CPX H2O (ppm)
d
OPX H2O (ppm)
e
OL H2O (ppm)
f
CPX Al2O3 (wt. %)
g
OPX Al2O3 (wt. %)
h
OL Mg#
Distance (µm)
Distance (µm)
Distance (µm)

Figure 2.

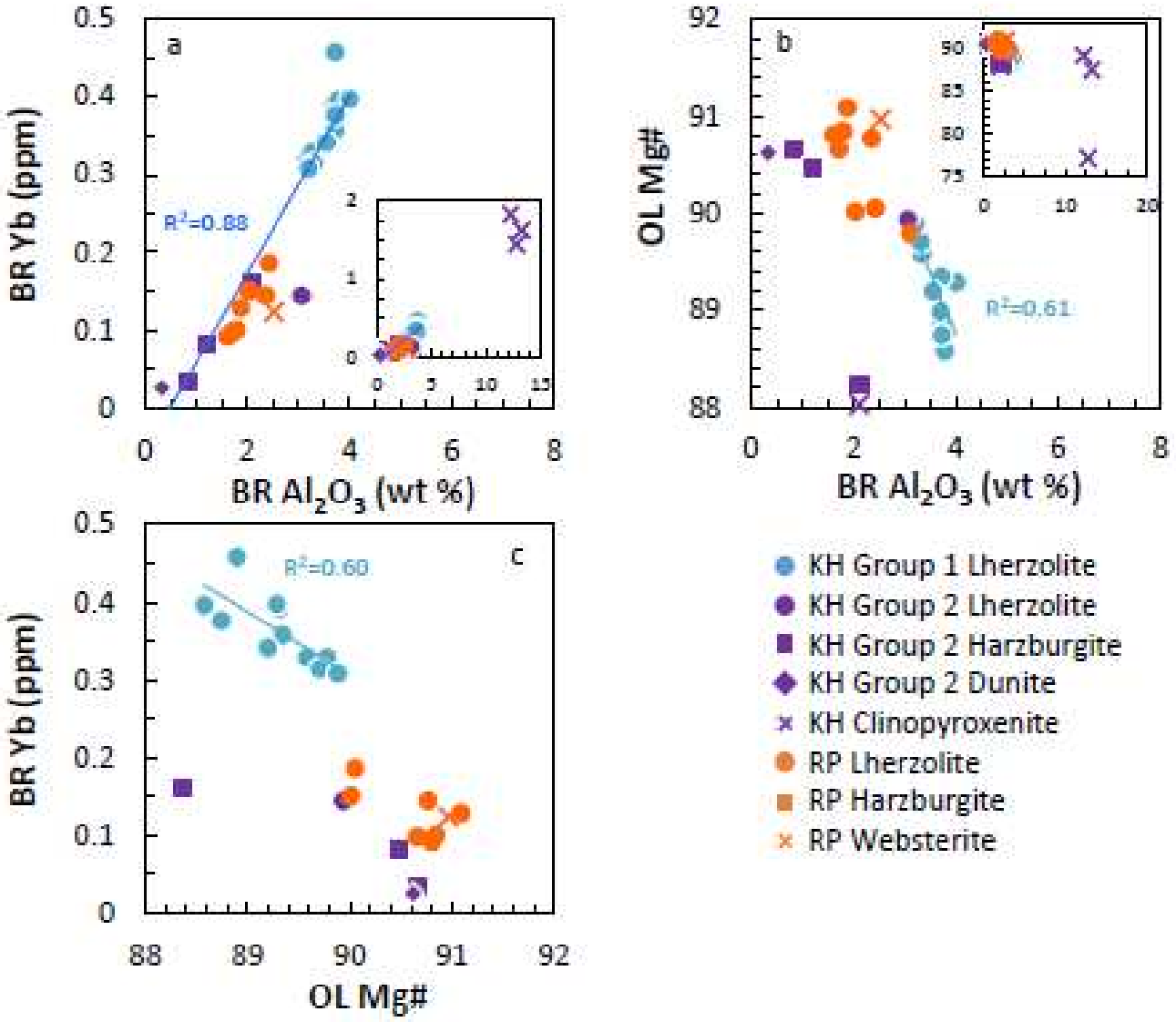

Figure 3.

1749

1750

1751

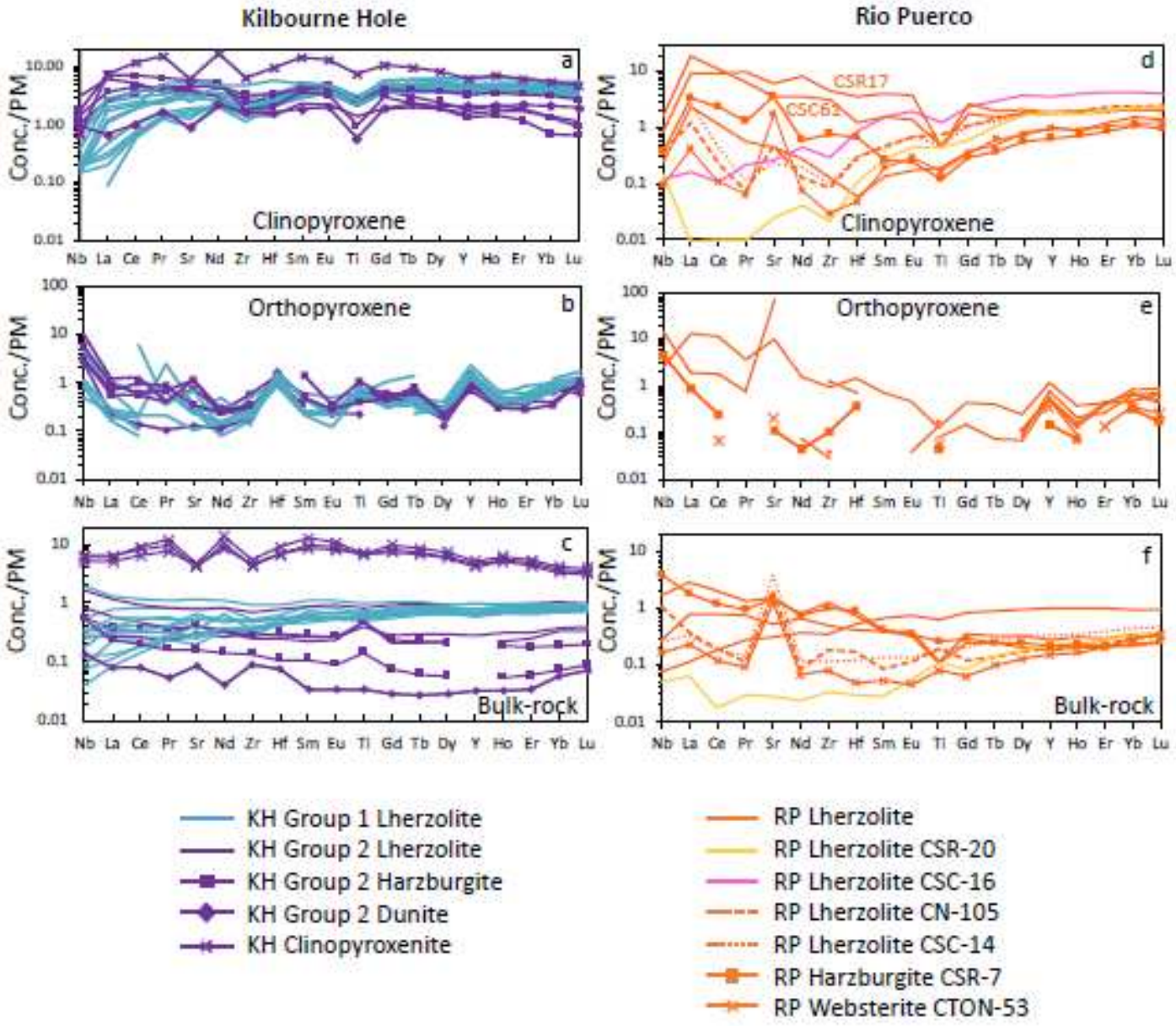
Kilbourne Hole
Rio Puerco
a
b
c
d
e
f
Clinopyroxene
Orthopyroxene
Bulk-rock
CSR17
CSC62
Conc./PM
Nb La Ce Pr Sr Nd Zr Hf Sm Eu Ti Gd Tb Dy Y Ho Er Yb Lu
KH Group 1 Lherzolite
KH Group 2 Lherzolite
KH Group 2 Harzburgite
KH Group 2 Dunite
KH Clinopyroxenite
RP Lherzolite
RP Lherzolite CSR-20
RP Lherzolite CSC-16
RP Lherzolite CN-105
RP Lherzolite CSC-14
RP Harzburgite CSR-7
RP Websterite CTON-53

Figure 4.

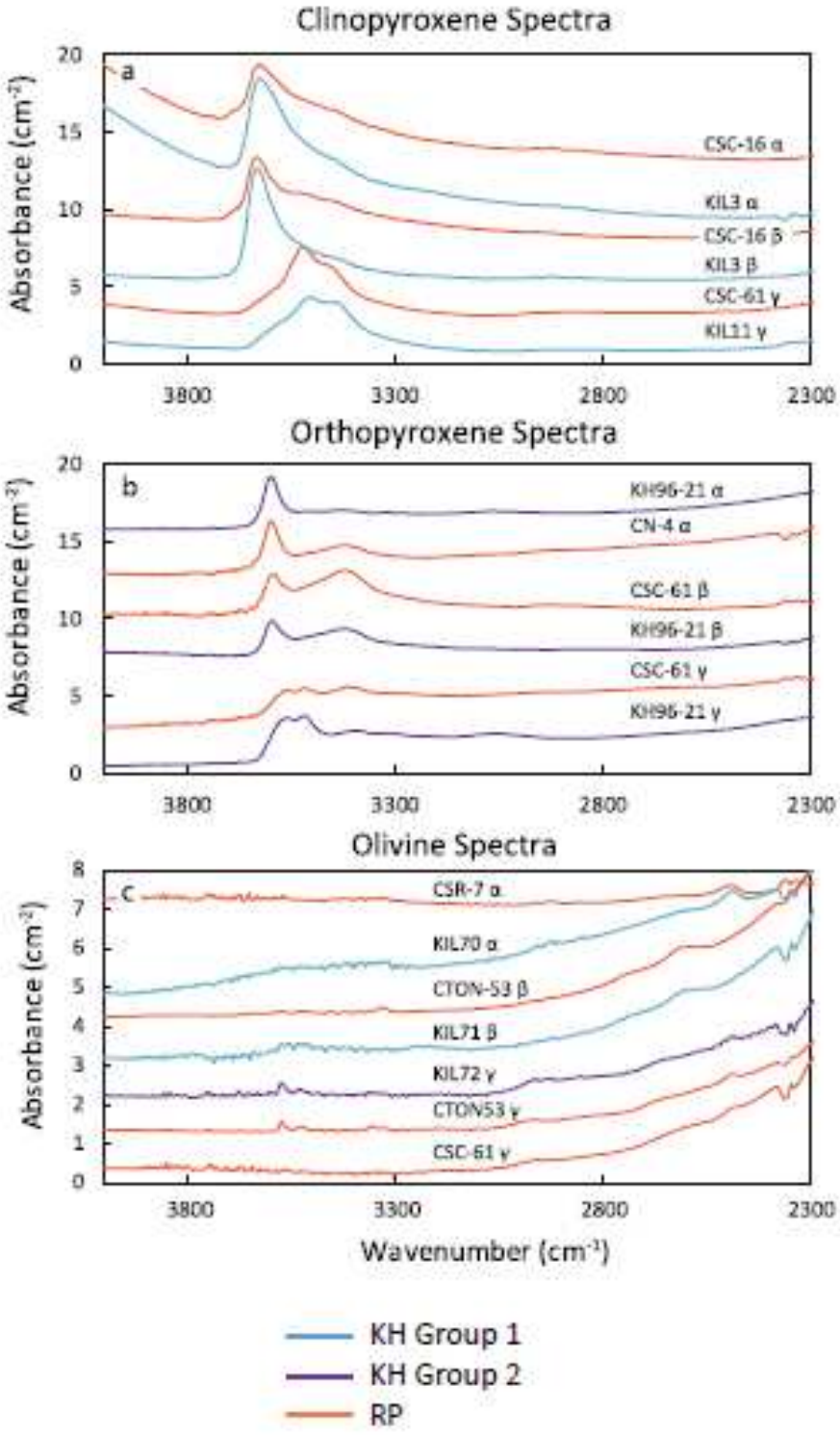

Figure 5.

1756

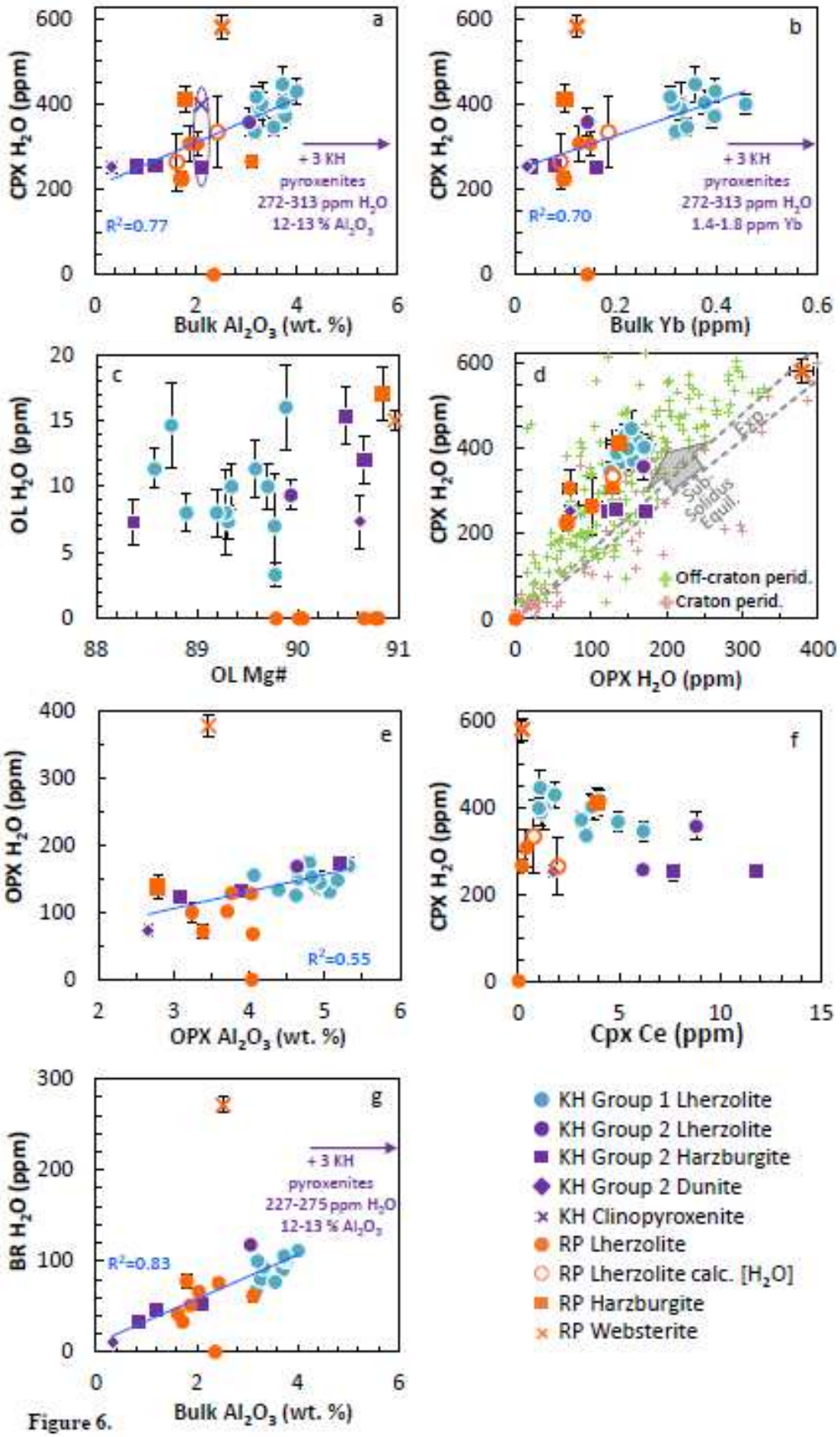

Figure 6.

1757

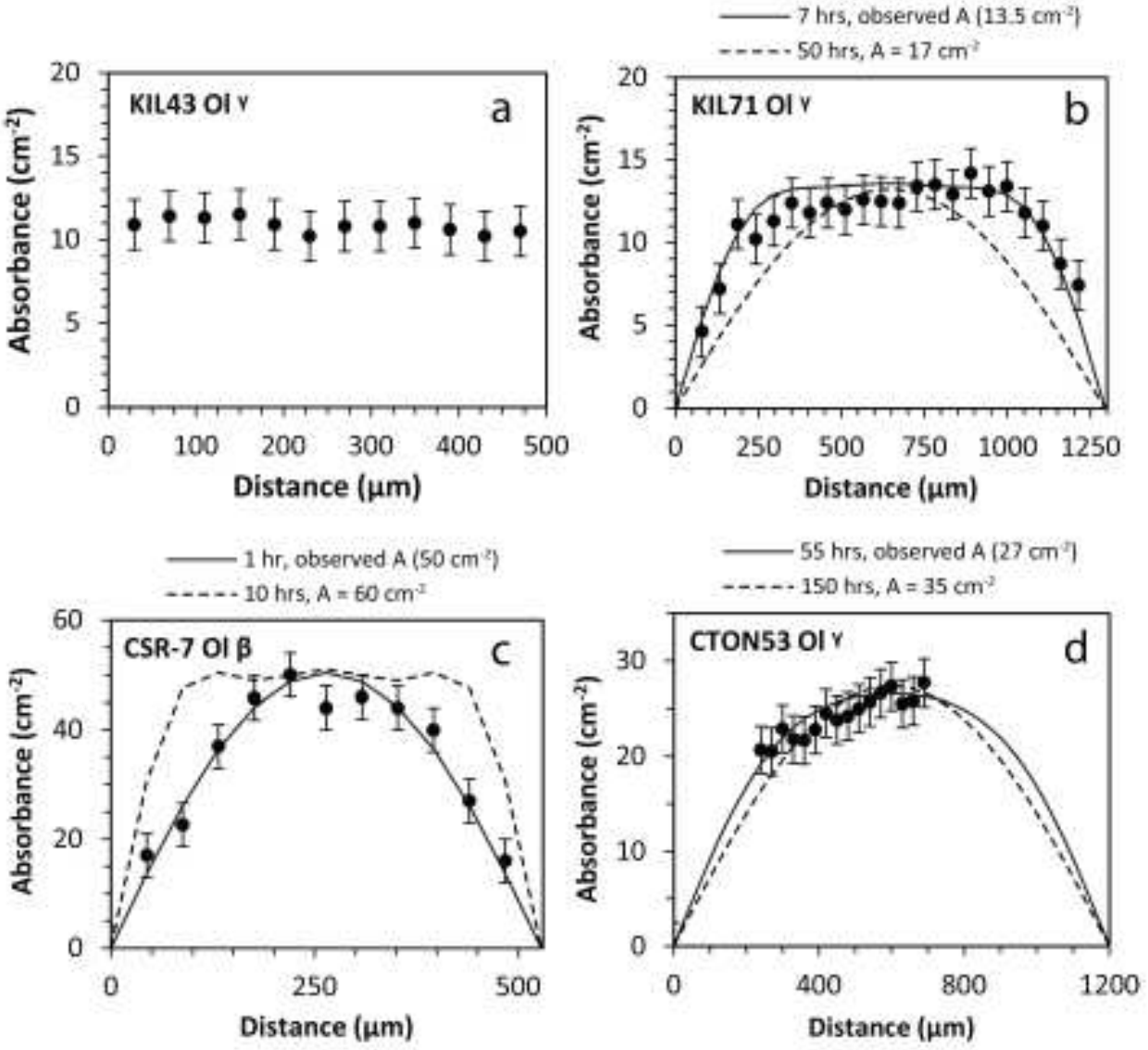

Figure 7.

1758

1759

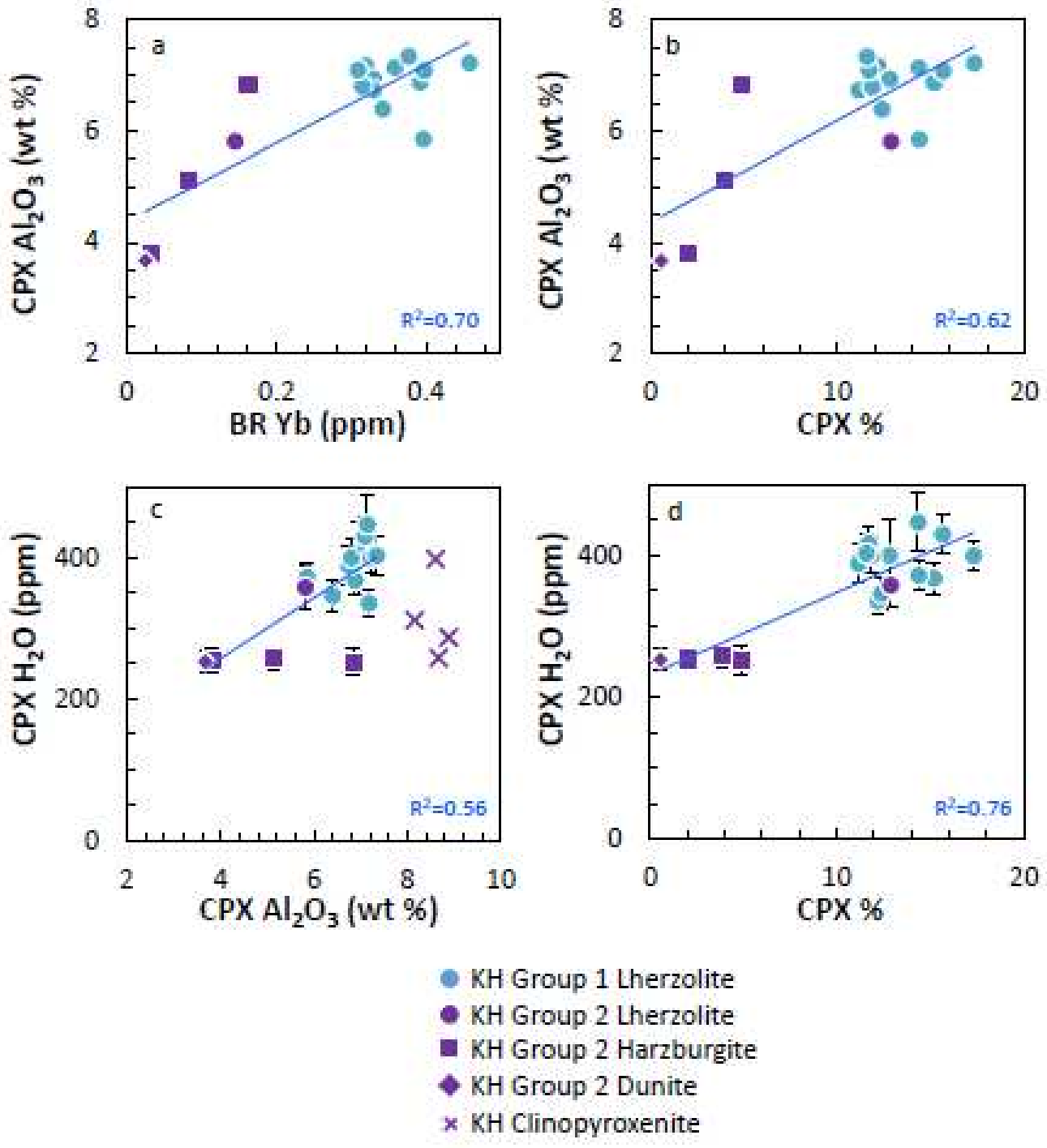

Figure 8.

1760

1761

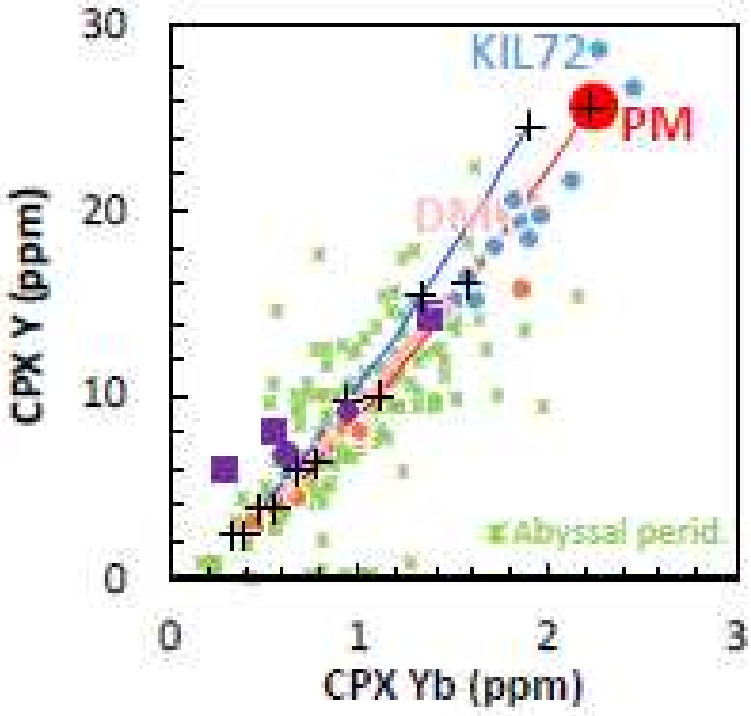

Figure 9.

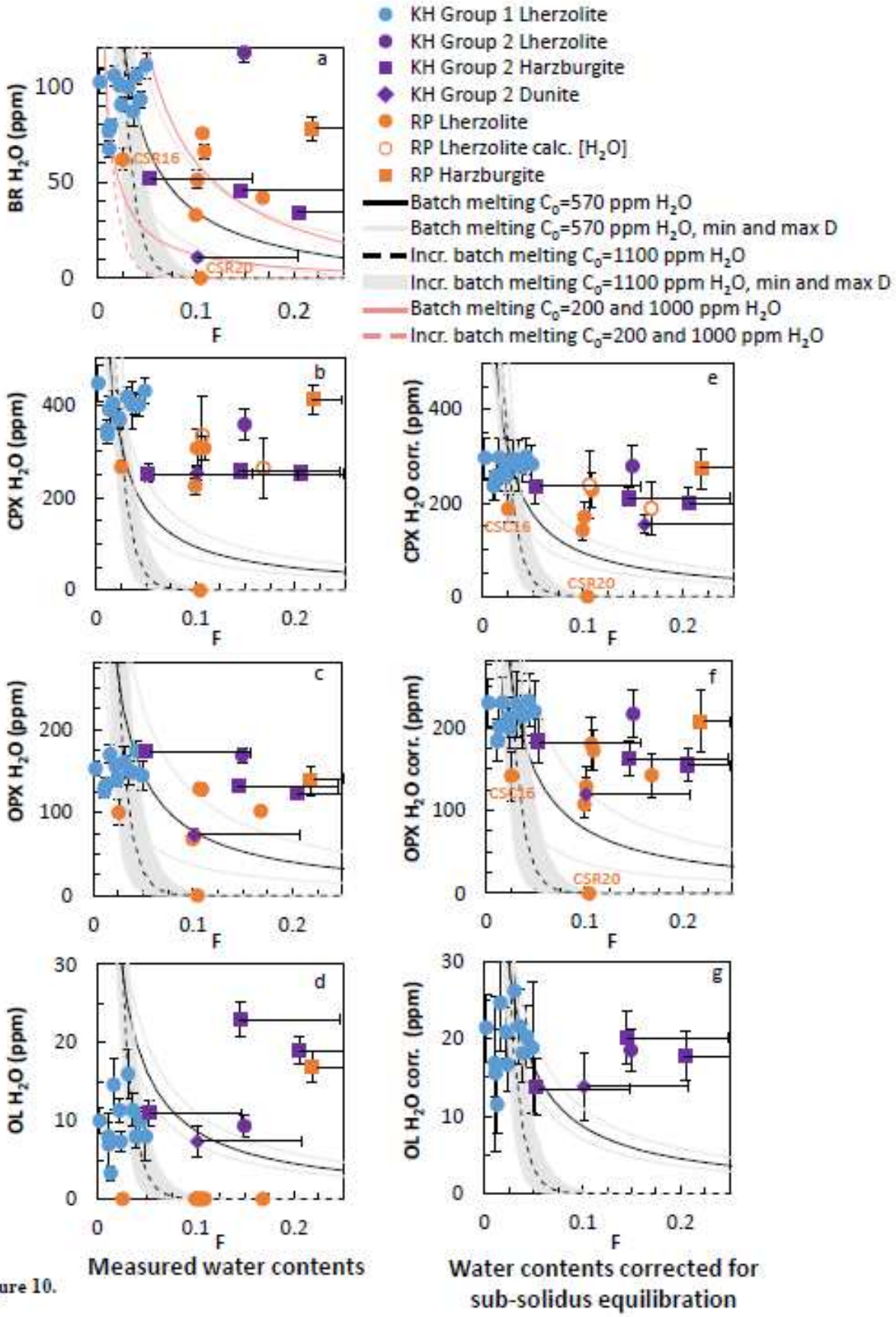

Figure 10.

1770

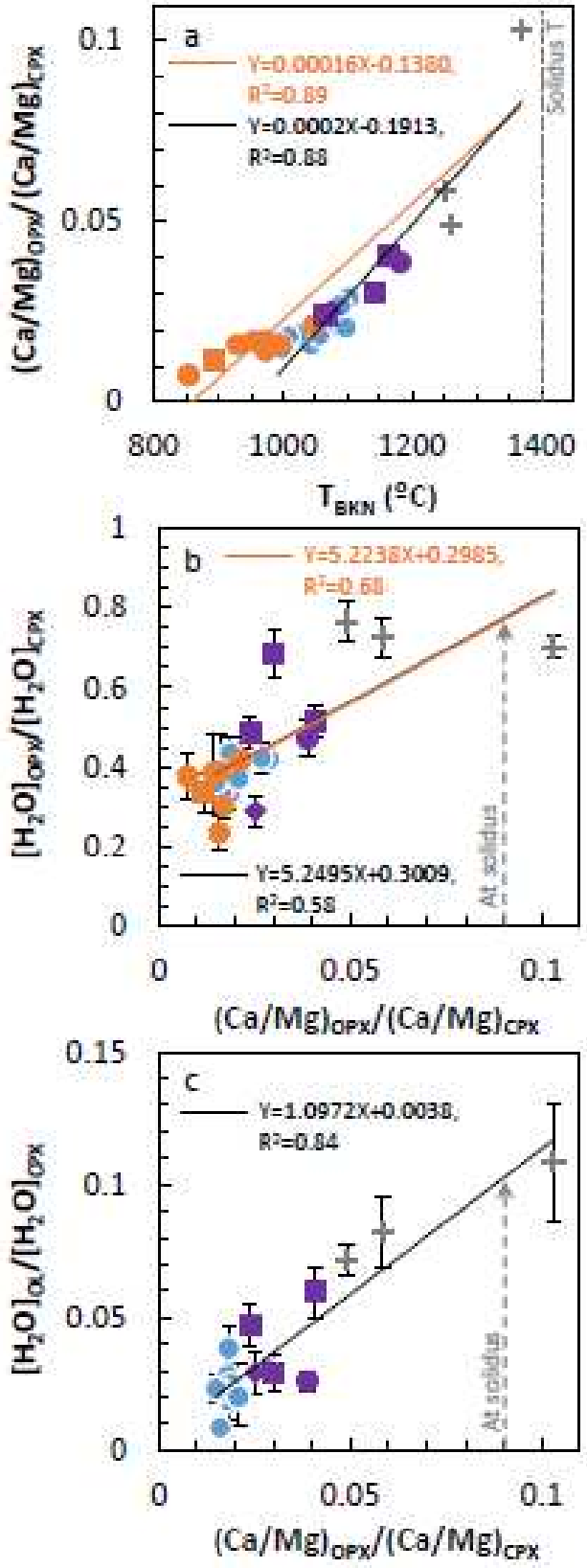

Figure 11.

1771

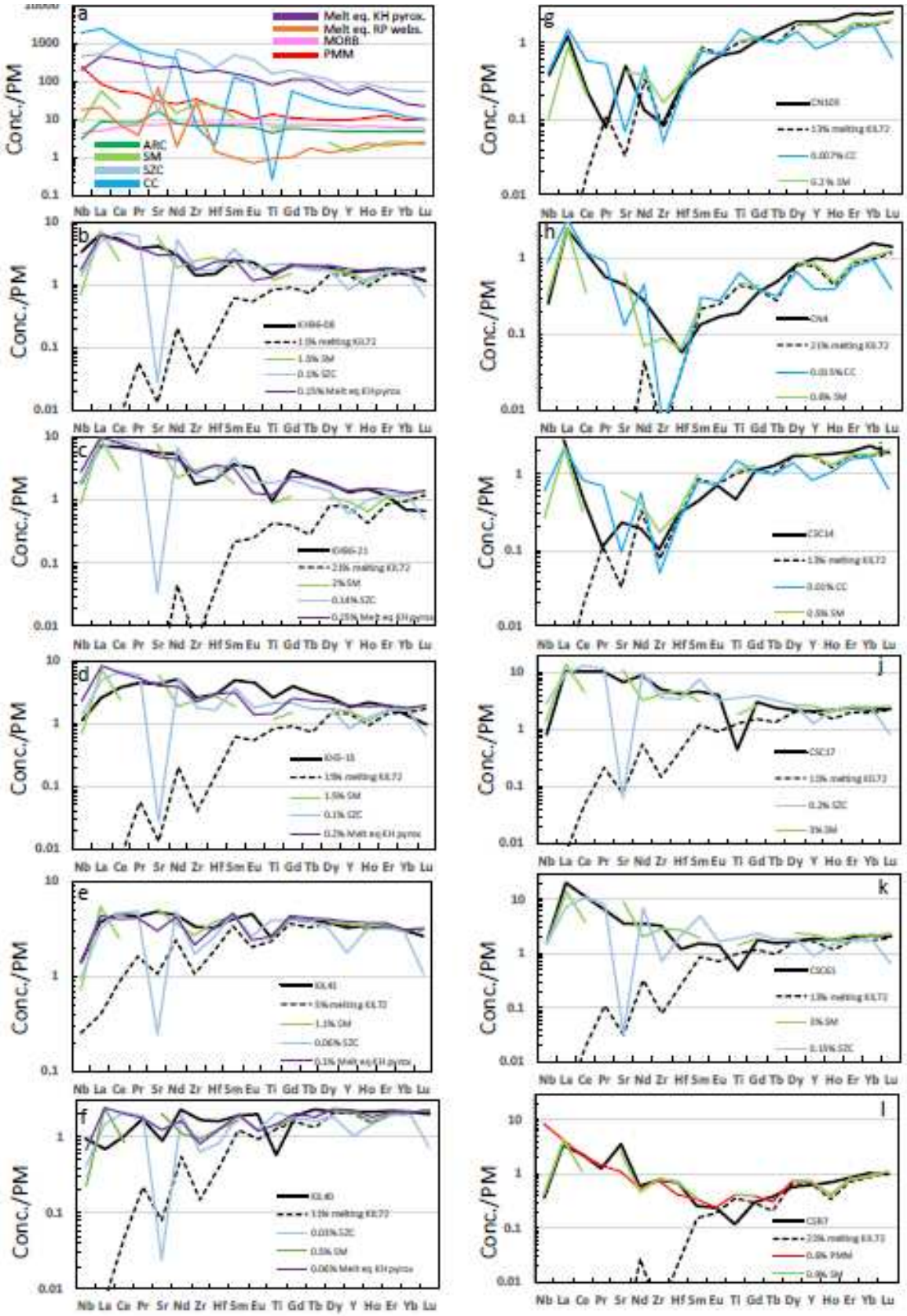
a
Melt eq. KH pyrox.
Melt eq. RP webs.
MORB
PMM
ARC
SM
SZC
CC
Conc./PM
Nb La Ce Pr Sr Nd Zr Hf Sm Eu Ti Gd Tb Dy Y Ho Er Yb Lu
b
c
d
e
f
g
h
i
j
k
l

Figure 12.

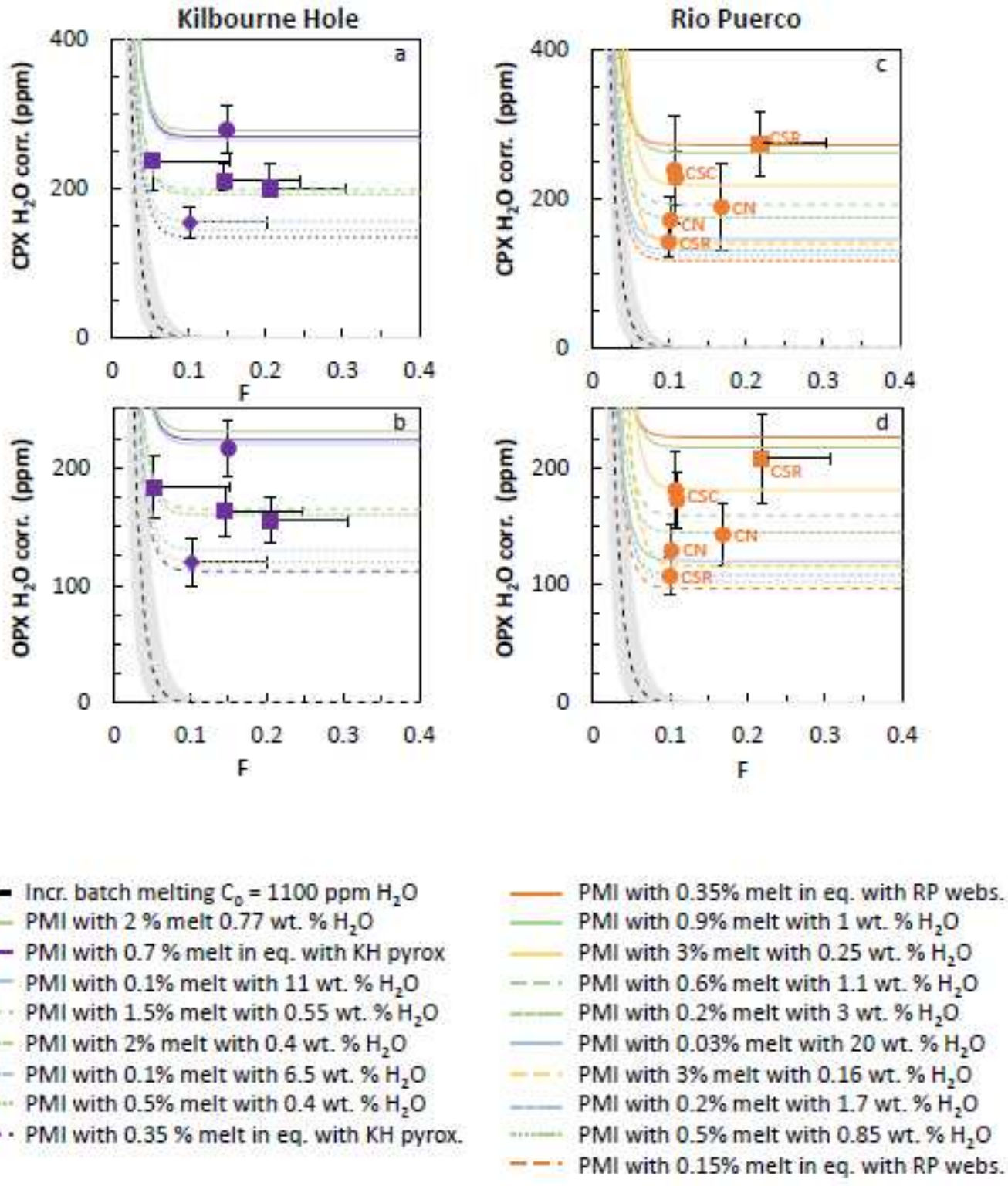

Figure 13.

1773

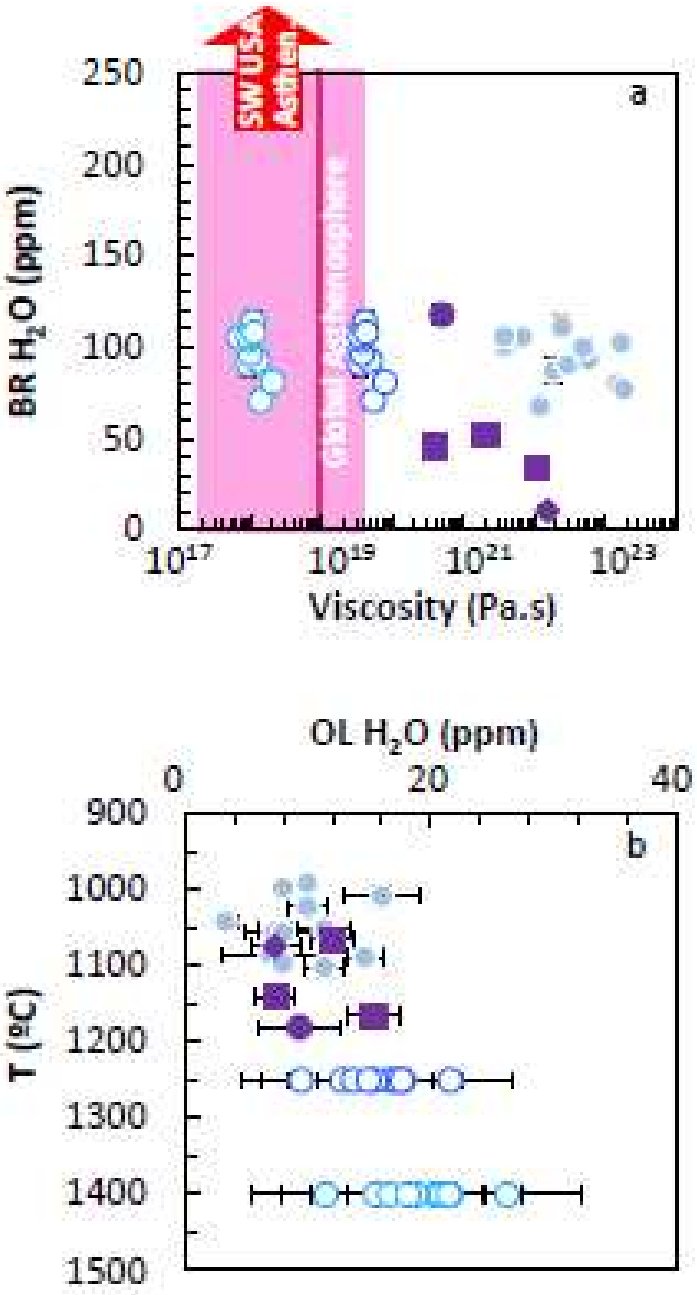

Figure 14.

1774

Supplementary information for Schaffer et al (2018), Evaluating the effects of subduction and rifting on the water contents of the Rio Grande Rift mantle

1- List of supplementary information tables

Table SI1: Bulk rock major element concentrations from XRF analysis (wt.%)

Table SI2: Mineral major element concentrations from EMP analysis (wt. %)

Table SI3: Bulk rock trace element concentrations from ICP-MS (ppm)

Table SI4: Clinopyroxene trace element concentrations from *in situ* LA-ICP-MS (ppm)

Table SI5: Orthopyroxene trace element concentrations from *in situ* LA-ICP-MS (ppm)

Table SI6: FTIR data; O-H integrated absorbances and water content calculations

Table SI7: Results of the degree of melting and of the peridotite-melt calculations

Table SI8: Phase proportions and partition coefficients from the literature used in trace element melting and mixing models

Table SI9: Mantle and melt trace element compositions from the literature

Table SI10: Experimental data from the literature used to calculate water partition coefficients and sub-solidus corrections

2- Description of FTIR spectra

In both KH and RP clinopyroxene, OH infrared absorption bands are observed between 3765 – 3000 cm^{-1} (Figure 5a). Spectra measured along the α and β indicatrix axes in KH and RP clinopyroxene (henceforth //α and //β) contain a main band dominating each spectrum centered at 3630 – 3640 cm^{-1} with a smaller band centered at 3450 cm^{-1}. The spectra //γ sometimes contain a small broad band centered at 3635 cm^{-1} followed by two main bands centered at 3525 and 3460 cm^{-1}. No OH bands were observed in clinopyroxene from CSR-20 and that peridotite also has the most depleted LREE signature out of all RP xenoliths (Figure 4). Clinopyroxene in CTON-53, CSR-7, CSC-17, and CSC-61 from RP also sometimes contain a band centered at 3525 cm^{-1} //α and //βon. This band at 3525 cm^{-1} ranges in size from grain to grain; it is non-existent in some grains and equal height with the band at 3450 cm^{-1} in other grains. The clinopyroxene spectra of websterite CTON-53 are not distinct from those of RP peridotite clinopyroxenes. There is also no distinction between KH Group 1 and 2 spectra.

Orthopyroxene OH infrared absorption bands in KH and RP spectra are located between 3729 – 2800 cm^{-1} (Figure 5b). When //α, KH and RP spectra contain a large band centered at 3600 cm^{-1} with a smaller band centered at 3420 cm^{-1}; a small broad band is sometimes observed centered at 3070 cm^{-1}. In websterite CTON-53 from Rio Puerco an additional small broad band is observed at 3305 cm^{-1} as well as an additional small narrow band at 3520 cm^{-1}. The KH and RP spectra //β are characterized by a large band centered at 3600 cm^{-1} and a smaller band centered at 3420 cm^{-1}. In KH and RP orthopyroxene, two bands with the largest height //γ are centered at 3565 cm^{-1} and 3520 cm^{-1}, followed in size by two smaller bands centered at 3400 cm^{-1} and 3320 cm^{-1}; a small broad band is sometimes observed at 3060 cm^{-1}. In all RP xenoliths except for CTON-53 and CSR-20, bands centered at 3565 cm^{-1}, 3520 cm^{-1}, and 3400 cm^{-1} are roughly equal in size, and the band

centered at 3320 cm^{-1} is not observed. No OH bands are detected in CSR-20 orthopyroxene. There is no obvious difference between KH Group 1 and Group 2 orthopyroxene spectra. Relative area beneath the OH absorption bands are consistently $\gamma > \alpha \geq \beta$.

All Kilbourne Hole olivine grains measured contained detectable water contents. Rio Puerco olivine grains have no detectable water with the exception of olivine in harzburgite CSR-7 and websterite CTON-53 (Figure 5c). In hydrated olivines from KH and RP, OH infrared absorption bands are observed between 3600 – 3000 cm^{-1}. When //α, the most prominent bands within a spectrum are centered at 3570 cm^{-1} and 3525 cm^{-1} with smaller additional bands sometimes observed centered at 3445, 3415, 3380, 3355, and 3330 cm^{-1}. Spectra //β sometimes contain bands centered at 3570 cm^{-1} and 3525 cm^{-1} and usually contain a prominent band centered at 3225 cm^{-1}. Spectra //γ contain two prominent bands centered at 3570 cm^{-1} and 3525 cm^{-1} with additional bands sometimes present centered at 3355 cm^{-1} and 3330 cm^{-1}. There is no difference between KH Group 1 and Group 2 olivine spectra. Websterite CTON-53 olivine spectra are not distinct from KH peridotite or CSR-7 olivine spectra. Seven out of 15 KH xenoliths have homogeneous integrated OH absorbances throughout their olivines, while other olivines from KH and in those from RP, OH integrated absorbances are lower at the edge of olivine grains compared to their core (Fig. 6, Table SI6).

3- Degree of melting

3-1 -Degree of melting from major element modelling of Herzberg (2004):

The major element compositions of KH and RP peridotites are compared to those of the partial melting models of Herzberg (2004) who used a fertile spinel lherzolite resembling primitive mantle (PM; McDonough and Sun, 1995) as the initial composition. That composition is more

1847 fertile (higher Al_2O_3 and lower MgO contents) than our most fertile KH or RP peridotites (Fig.
1848 SI3 a and b) and, therefore, the degrees of melting obtained by that method are maximum values.
1849 The results for isobaric batch melting at 1 and 2 GPa, and decompression fractional melting starting
1850 at 2 and 3 GPa are shown in Fig. SI3 a and b. Initial pressures of 3 GPa are considerably higher
1851 than the estimated equilibrium pressures for KH and RP xenoliths (1-1.8 GPa; Perkins and
1852 Anthony, 2011; Porreca et al., 2006), however, 2 and 3 GPa are the lowest pressure at which
1853 fractional melting models were run (Herzberg, 2004). The major element concentrations of all KH
1854 xenoliths plot near or along the melting trends of (Herzberg, 2004). The exception is the lherzolite
1855 KH96-08, which has bulk-rock MgO and Al_2O_3 concentrations that are slightly too low compared
1856 to the models. However, KH96-08 is considered to be anomalous because it has an unusually high
1857 modal abundance of low-Ca pyroxene (45% orthopyroxene, 44% olivine), which is interpreted as
1858 evidence of modal metasomatism resulting from a peridotite-melt reaction in a supra-subduction
1859 zone environment that re-equilibrated texturally (Harvey et al., 2012). The KH xenoliths plot
1860 equally close to batch and fractional major element melting trends with the most depleted KH
1861 peridotite, the dunite, recording slightly lower melting degrees with batch melting (31%) compared
1862 to fractional melting (33%).

1863 Overall, the major element compositions of RP peridotites do not fall on Herzberg's
1864 melting trends for either batch or fractional melting but parallel to them (Fig. SI3 a and b), being
1865 generally displaced to lower MgO and Al_2O_3 abundances (Herzberg, 2004). This could mean that
1866 the RP protolith had a different composition prior to melting with lower abundances of Fe, Al, Ca
1867 and Na compared to the composition used in the (Herzberg, 2004) models or that of KH.
1868 Alternatively, as noted in the previous section, their major element compositions may have instead
1869 been affected by modal metasomatism. Even CN-4 and CSR-17, the most major element-depleted

peridotites, have elevated LREE relative to HREE (Fig. 4), indicating cryptic metasomatism. Therefore, it appears that the major element geochemistry of KH peridotites is controlled by partial melting, while RP major element geochemistry reflects a more complicated history that likely includes multiple events of melting, metasomatism and possibly an unusual protolith composition.

3-2 -Degree of melting estimated from the spinel Cr#

Based on abyssal peridotite data, it has been proposed that the Cr# of spinel can be used to calculate the degree of melting of spinel peridotites (Hellebrand et al., 2001). Using that method, degrees of melting of 0 to 16 % for KH and 1 to 14% for RP are calculated. These are lower than those obtained with the decompression (2-0 GPa) melting model of Herzberg (2-26 % for KH and 7-17% for RP) and those obtained with the Y and Yb contents of clinopyroxene (up to 1-20 and 2-22 %). Peridotites from KH Group 1 have higher HREE contents than most abyssal peridotites which are thought to have resulted from melting of the DM, as opposed to PM (Fig. 9). The lower degree of melting obtained using the spinel Cr# method based on abyssal peridotite data is expected given the more fertile initial compositions used with the other two methods and illustrate that using this model to peridotites other than strongly depleted abyssal peridotites should be done with caution.

4- Viscosity calculations

The viscosity of the KH peridotites is calculated using their olivine water contents and a flow law for olivine aggregates at equilibration temperatures (Li et al., 2008). Li et al 2008 derived

their equation from that of Mei and Kohlsted 2000 established from experiments in dislocation creep regime.

Effective viscosity:

$$\eta_{eff} = \tau / \dot{\varepsilon} \quad \text{(eq. SI1)}$$

η_{eff} = effective viscosity (Pa·s)

τ = shear stress (0.3 MPa (Li et al., 2008) or 0.6 MPa ())

$\dot{\varepsilon}$ = strain rate (s^{-1})

Strain rate:

$$\dot{\varepsilon} = A_{cre}{}^{n1}(\exp(c_0 + c_1 \ln C_{OH} + c_2 \ln^2 C_{OH} + c_3 \ln^3 C_{OH}))^r \exp(\frac{Q + PV_{cre}}{RT}) \quad \text{(eq. SI2)}$$

A_{cre} = experimentally determined constant 90 $MPa^{-(n1+r)}s^{-1}$ with stress exponent n1 = 3.5 and the water fugacity exponent r = 1.2 (Hirth and Kohlstedt, 2004)

c = parameters for water fugacity in the environment {Mei, 2000 #1750; Li et al., 2008): c_0 = -7.9859, c_1 = 4.3559, c_2 = -0.5742. c_3 = 0.0337

C_{OH} = water content of olivine ($H/10^6Si$, converted from ppm H_2O with a SiO_2 content in olivine of 40.60 wt %)

Q = activation energy for dislocation creep of olivine (480 kJ/mol; Hirth and Kohlstedt, 2004)

V_{cre} = activation volume for dislocation creep of olivine (10.6 x 10^{-6} m^3/mol; Li et al., 2008)

P = pressure (Pa)

T = temperature (^oK)

R = gas constant (8.314 J $mol^{-1}K^{-1}$)

5- Supplementary figures

Figure SI1. Examples of textures found in KH and RP peridotites. Sample KIL8 in a is shown in cross-polarized light. This is the only KH sample which exhibits an equigranular texture. A protogranular texture is observed in all other KH samples, as seen for KIL3 in plane polarized light in b. This sample contains small glass veins, also present in samples KIL1, KIL2, and KIL41. In c, xenolith CN-4 from RP shows exsolution lamellae within the large orthopyroxene grain (opx) as well as inclusion-rich clinopyroxenes. Samples from RP are highly fractured, as shown in the photograph of CN-105 in d.

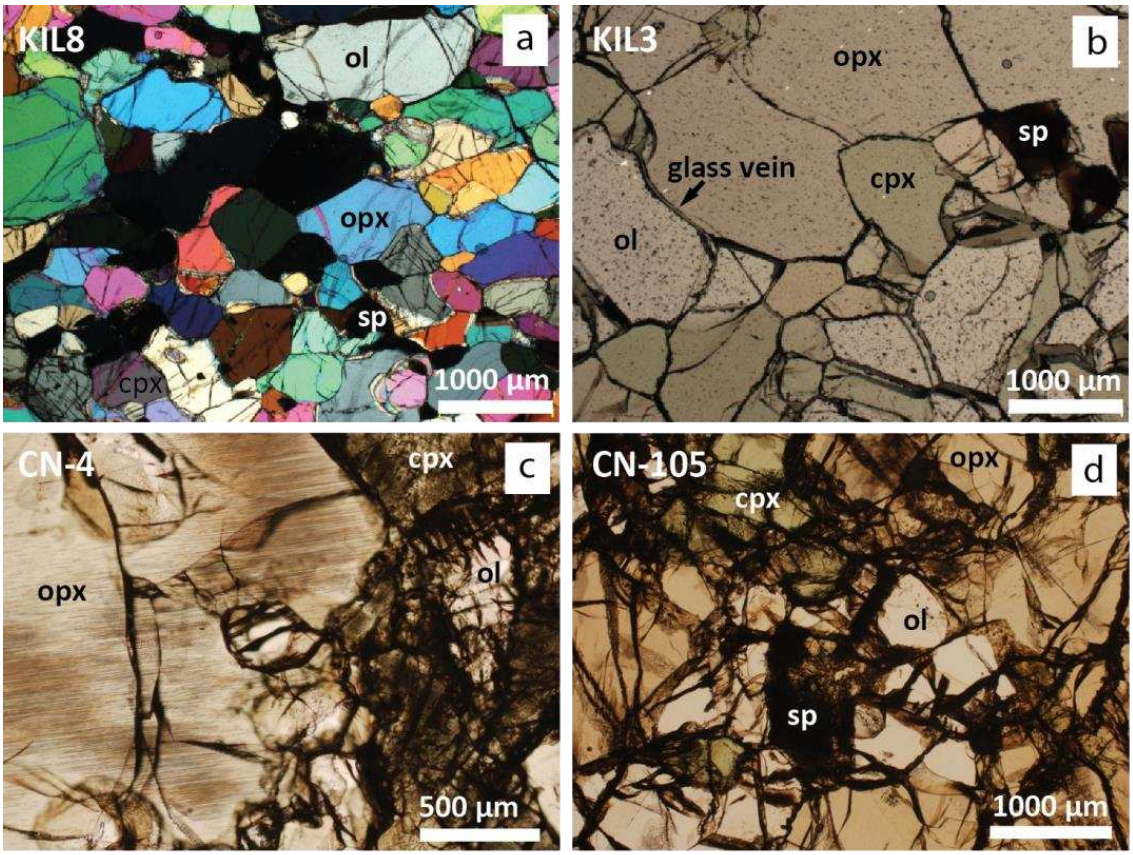

Figure SI2. Major element transects across a clinopyroxene with a spongy rim in peridotite xenolith CSC-61 from Rio Puerco. The spongy rim has a different major element composition compared to the homogeneous clinopyroxene, a feature found in all RP peridotites.

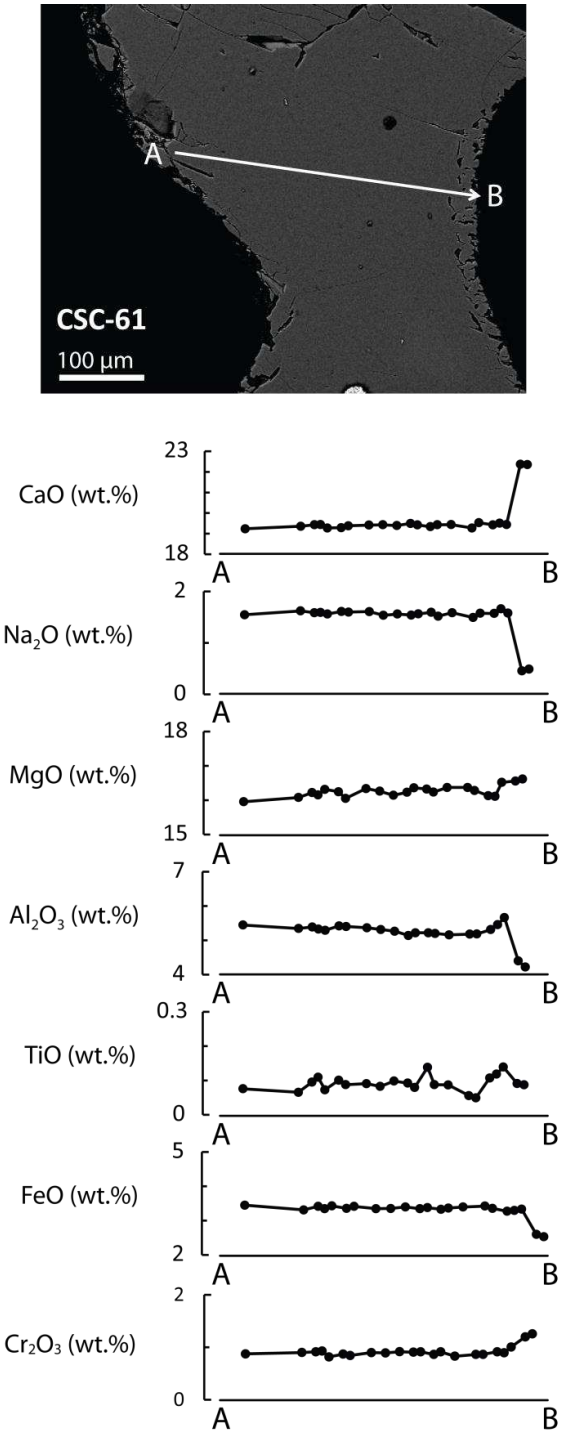

Figure SI3: Determination of the degree of melting using Herzberg's (2004) modelling of bulk-rock (BR) MgO and Al_2O_3 contents during melting of a fertile spinel peridotite compared to those of KH and RP peridotites (symbols as in Fig. 6).

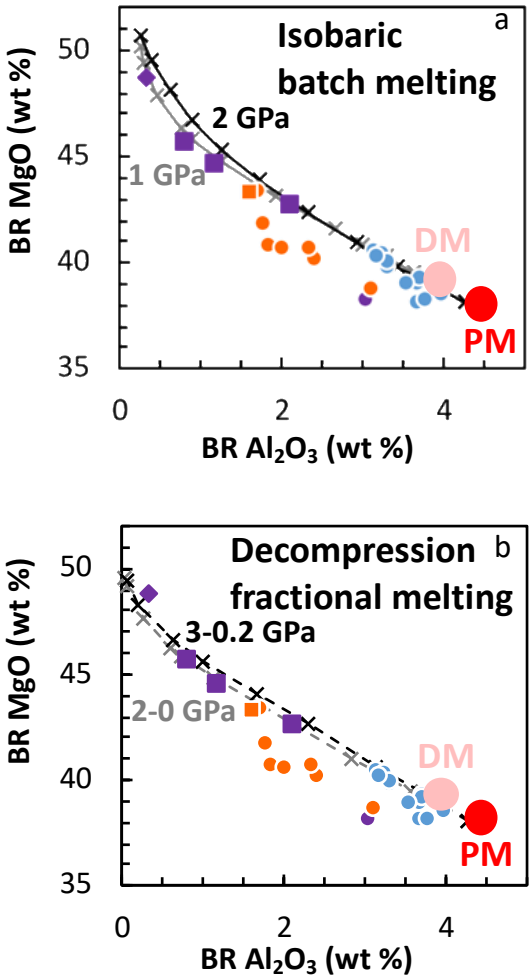

Figure SI4: Clinopyroxene (CPX) trace element concentrations normalized to primitive mantle (PM) composition (McDonough and Sun, 1995) in Kilbourne Hole (KH, a-b) and Rio Puerco (RP, c-d) peridotites compared to incremental batch melting models of PM-like lherzolite KIL72 from 1 to 20%.

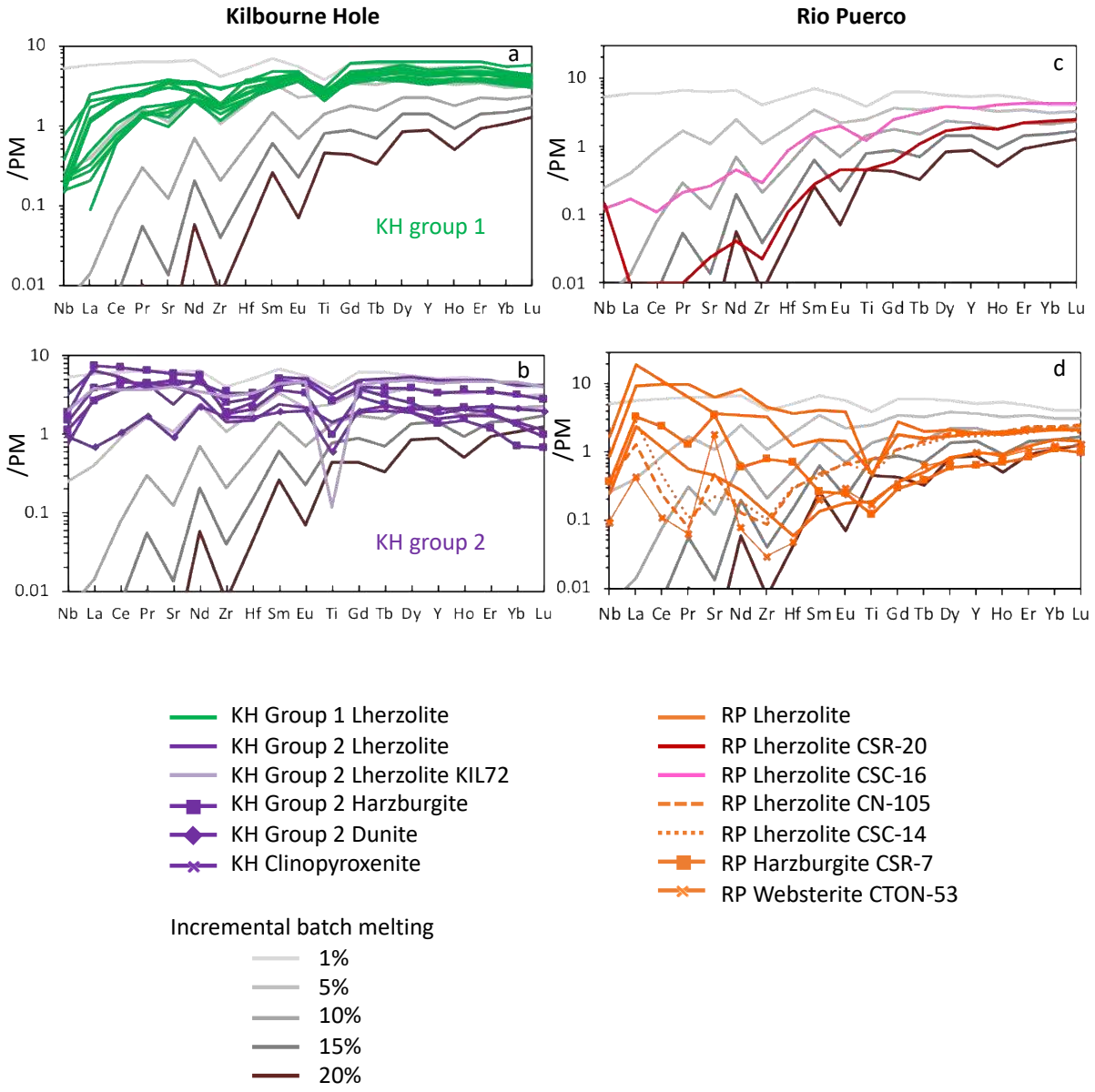

Figure SI5: Clinopyroxene composition normalized to primitive mantle (PM) from peridotite-melt interaction models compared to RP websterite CTON53 (thick black line). First, the starting composition of the peridotite is calculated by incremental batch melting models (dashed black line) from the composition of KIL72 to match CTON53 MREE-HREE. Then that residue composition is mixed with various melts (Figure 11a) which composition results from assimilation and crystallization modelling (AFC) until the profile matches that of CTON53. For clarity, only the best matches between models and data are shown. Melt in equilibrium with primitive mantle (PMM), slab silicate melt (SM), and subduction zone carbonatite (SZC).

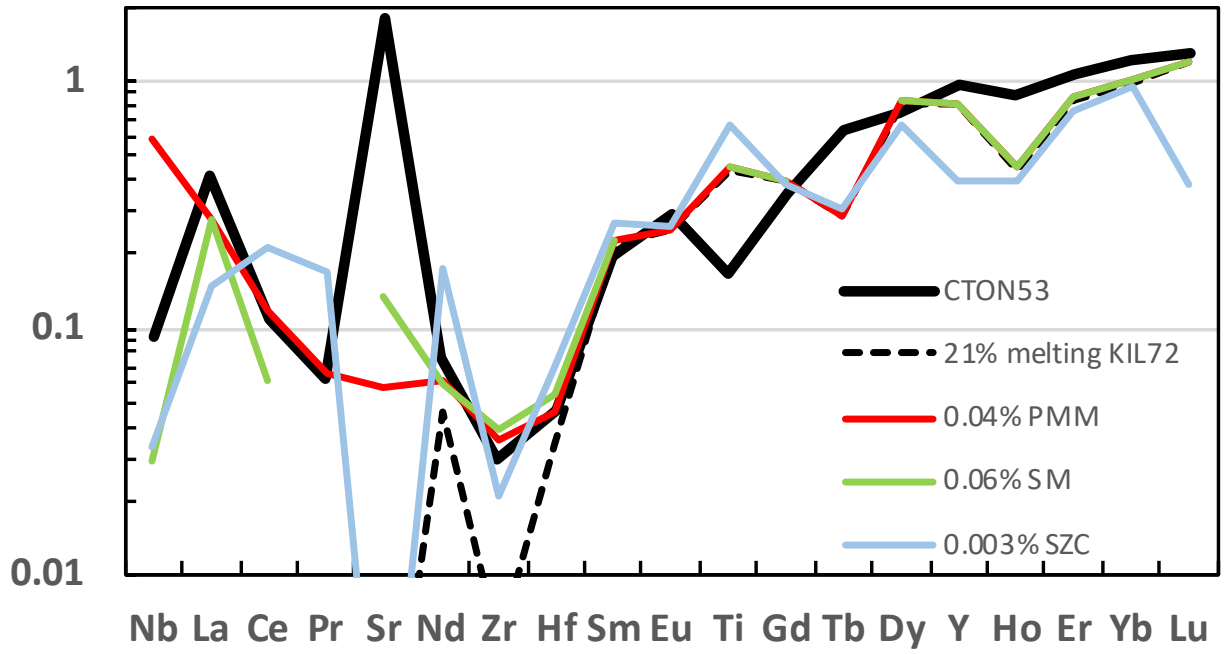

Figure SI6: Comparison of viscositie calculated with a) a stress of 0.3 MPa (Li et al., 2008) and b) with a stress of 0.6 MPa (Hansen and Warren 2015), and c) dependance of calculated viscosities to temperature. Empty blue circles are for viscosities with olivine water contents of KH Group 1 calculated at possible lithosphere-asthenospheric boundary depths beneath KH (bright blue for 62 km and 1250°C and light blue for 70 km and 1400°C, i.e. near solidus conditions).

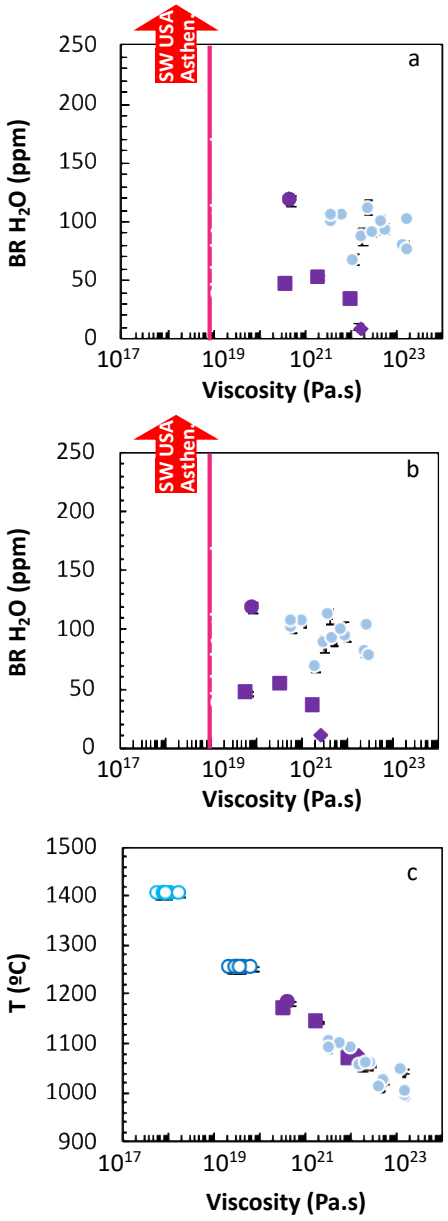

1962

1963